November 18, 2020

Electron Ion Collider
Conceptual Design Report
Experimental Equipment

Contributors:
W. Akers[2], E-C. Aschenauer[1], F. Barbosa[2], A. Bressan[3], C.M. Camacho[4], K. Chen[1], S. Dalla Torre[3] L. Elouadhriri[2], R. Ent[2], O. Evdokimov[5], Y. Furletova[2], D. Gaskell[2], T. Horn[6], J. Huang[1], A. Jentsch[1], A. Kiselev[1], W. Schmidke[1], R. Seidl[7], T. Ullrich[1],

[1]Brookhaven National Laboratory, USA
[2]Thomas Jefferson National Accelerator Facility, USA
[3]University of Trieste and INFN at Trieste, Italy
[4]Institut de Physique Nucléaire at Orsay, France
[5]University of Illinois at Chicago, USA
[6]Catholic University of America, Washington DC, USA
[7]RIKEN Nishina Center for Accelerator-Based Science, Japan

Contents

Chapter 2

The Science of EIC

2.1 Introduction

The science mission of the Electron-Ion Collider is to provide us with an understanding of the internal structure of the proton and more complex atomic nuclei that is comparable to our knowledge of the electronic structure of atoms. Unlike the more familiar molecular and atomic structure, the interactions and structures are not well separated in protons and other forms of nuclear matter, but are inextricably mixed up, and the observed properties of nucleons and nuclei, such as mass and spin, emerge out of this complex system.

2.1.1 EIC Physics and Accelerator Requirements

A consensus study report of the National Academies of Sciences, published in 2018, on an **Assessment of U.S.-based Electron-Ion Collider Science** [1], recognized this and concluded "EIC science is compelling, timely and fundamental". The NAS study further found that "An EIC can uniquely address three profound questions about nucleons — neutrons and protons — and how they are assembled to form the nuclei of atoms:

- How does the mass of the nucleon arise?
- How does the spin of the nucleon arise?
- What are the emergent properties of dense systems of gluons?"

They also concluded that "These three high-priority science questions can be answered by an EIC with highly polarized beams of electrons and ions, with sufficiently high luminosity and sufficient, and variable, center-of-mass energy."

This reinforces the unique accelerator requirements of the Electron-Ion Collider, requiring a large luminosity, 10^{33-34} over a large and variable range of center-of-mass energies, between 20 and 140 GeV, high electron and (light) ion beam polarizations of above 70%,

and a large range of accessible ion beams, from deuterium to the heaviest nuclei (uranium or lead). It should be understood that the required electron polarization is longitudinal, whereas the polarization requirement for protons and light ions is for both longitudinal and transverse. Due to the broad science program foreseen at the Electron-Ion Collider, the possibility to have a second interaction region and associated detector was emphasized in the report.

As stated in the National Academy of Sciences Committee recommendations, "a central goal of modern nuclear physics is to understand the structure of the proton and neutron directly from the dynamics of their quarks and gluons, governed by the theory of their interactions, quantum chromodynamics (QCD), and how nuclear interactions between protons and neutrons emerge from these dynamics." The scientific program of the Electron-Ion Collider (EIC) is designed to make unprecedented progress towards this goal.

The EIC can be seen as a microscope to image the 3D QCD structure of protons, neutrons and other hadrons - composite systems of quarks and gluons, and their intrinsic dynamics and correlations that lead to mass, spin, and other emergent properties. The EIC would explore the QCD landscape over a large range of resolution (Q^2) and quark/gluon density ($1/x$), from the region where visible matter is (mostly) quark systems built from up, down and strange quarks to a gluon-dominated region. Heavy nuclei are critical to explore the high-density gluon matter.

2.1.2 Interaction Region and Detector Requirements

Beyond the unique accelerator requirements, EIC science also leads to a unique set of detector requirements, and a novel **fully** integrated detector and interaction region scheme. **All** final state particles carry information about the 3D QCD structure of nuclear matter and the emergent phenomena. Therefore, it is essential that the interaction region and the detector at the EIC are designed so all particles are identified and measured at as close to 100% acceptance as possible and with the necessary resolutions.

The basic physics process at the EIC is Deep Inelastic Scattering (DIS), which is represented in Fig. 2.1. An ion, composed of nucleons, which are in turn composed of partons (quarks and gluons), moves in one direction and collides with an electron moving in the other direction. The electron collides with a parton within the ion in a hard collision.

We qualitatively define three classes of particles in the final state:

- The scattered electron,
- Particles associated with the initial state ion, and
- Particles associated with the struck parton.

The difficulty in achieving good acceptance in the forward regions at a collider has to do with the accelerator elements needed to deliver the colliding beams. To first order, the luminosity at the interaction point is inversely proportional to the distance between the

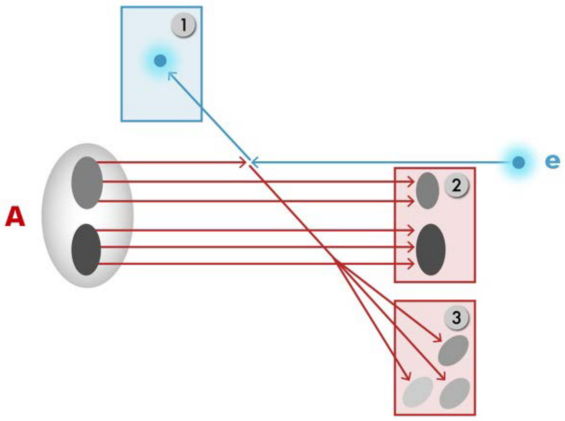

Figure 2.1: Classification of the final-state particles of a DIS process at the EIC: scattered electron (1), the particles associated with the initial state ion (2), and the struck parton (3).

nearest quadrupole magnets. On the other hand, the closer the beam elements are to the interaction point, the more they obstruct the acceptance at shallow angles with respect to the beam axis, and restrict the acceptance for forward particles. This complicates achieving close to 100% acceptance for all three types of particles, but especially the particles associated with the initial state ion.

This leads to a unique and novel integration of the detector in the interaction region, extending over a large region ($\pm$ 40 m) beyond the main detector. It also should be pointed out that any change has impact on a wide variety of systems, from beam dynamics to accelerator performance to magnet engineering requirements to detection capability – the latter in terms of (gaps in) acceptance, particle identification and resolutions.

Further integration is required for ancillary measurements to deliver on the EIC science program, such as those to absolutely determine the longitudinal electron and longitudinal and/or transverse proton/light-ion polarizations with beam polarimeters, with good systematic (order 1%) understanding. For the electrons a transverse polarization measurement is not a requirement but often useful to underpin the systematic understanding of the spin direction. Further, the exact frequency of electron-ion collisions per second must be experimentally determined with luminosity monitors with again a goal of better than 1% understanding. Both of these goals are non-trivial, with beam dynamics potentially impacting long-time averaging methods.

The central detector region of the EIC is designed to measure those final state particles from the hard collision between the electron and the parton in the ion (particles of types 1 and 3 in Fig. 2.1) and is very much like the traditional collider detectors. The EIC central detector needs to provide the measurements to determine Q^2 and x variables of the electron scattering kinematics (or, the resolution Q^2 and quark/gluon density $1/x$ of the QCD landscape). The central detector is divided into three sections, the Electron-endcap, the Hadron-endcap and the Barrel. The three different central detector sections correspond to different x and Q^2 regions for the scattered electron.

Beyond determination of x and Q^2, measurement of two transverse kinematics degrees of freedom (transverse momentum and impact parameter), as well as flavor identification of the partonic collision is central to the 3D QCD nucleon and nuclear structure program planned for the EIC. The energy scale of the transverse kinematics is $\sim$200 MeV/c. This means that identification and precise measurements of single hadrons among the particles associated with the scattered partons (Particles of type 3 in Fig. 2.1) are also needed in the central detector.

Crucial information on hadron structure is carried by particles that do not emerge from the beam envelope within the coverage of the central detector. Broadly speaking, there are two types of forward final state particles that need to be reconstructed. The first type of forward particles comes from interactions in which the beam particle receives a large transverse momentum kick and fragments into many parts. These particles typically retain a velocity similar in magnitude, but with significantly different kinematics, from that of the incident beam particle and may have very different charge-to-mass ratios. Such particles will separate relatively rapidly from the beam. An example of such a particle is a forward proton from a deuteron-electron DIS, a process that can give information on QCD neutron structure (inside a deuteron) comparable to QCD proton structure. Another example are forward neutrons.

The second type is a (hadron) beam particle that stays intact during the collision, only loses a small fraction of its longitudinal momentum, and acquires a small transverse momentum. These particles are for example protons or ions in non-dissociative diffractive interactions and will have a trajectory that is close to the proton (ion) beam. To map these types of forward final state particles, a highly-integrated extended ("far-forward") detector region is defined downstream of the ion beam, and after the beam final-focusing elements, covering about 30 m. The far-forward detector region together with the central detector provides essential near-complete coverage for final state particles associated with the incident ion beam particle.

Similarly, the "far-backward" detector region is highly integrated to capture a third type of measurements, those close to the beam line in the electron-beam direction. This allows to monitor the luminosity as well as to significantly increase the low-Q^2 coverage of the detector. Electron-ion collisions where the electron is scattered through a very shallow angle corresponds to the case where the exchanged photon is almost real. Such photoproduction processes are of interest in their own right but also can allow a program of spectroscopy.

The science program at the electron-ion collider (EIC) has the potential to revolutionize our understanding of 3D QCD nuclear and nucleon structure. It will also explore new states of QCD. In order to maximize the potential of an EIC, it is important to have a large (near-100%) acceptance not only in the central region, but also in the region that is close to both the ion-beam and electron-beam direction — i.e. a total acceptance detector is needed. There has never been a collider detector that has both the central and forward (or backward) acceptances maximized in tandem, and this design is uniquely suited to the EIC physics program.

2.2 EIC Context and History

Half a century of investigations have revealed that the neutrons and protons (nucleons) that make up the atomic nucleus are composed of more basic constituents, the quarks and gluons, with their interactions mediated by the exchange of gluons. Their discovery has led to the development of the fundamental theory of strong interactions, quantum chromodynamics (QCD). QCD attributes the forces among quarks and gluons (collectively called partons) to their color charge. In contrast to quantum electrodynamics, where the force carriers (photons) are electrically neutral, gluons carry color charge and therefore do self-interact.

As a consequence of QCD, the internal structure of nucleons consists of a complex dynamical system of valence quarks immersed in a quantum sea of virtual quarks, antiquarks, and gluons, a system unlike any other heretofore observed in nature. The spin of the nucleon is not a simple sum of the spins of the valence quarks, but also includes significant contributions from this quantum sea. The mass of the nucleon is not the sum of its constituent partons (which is near zero), but emerges from interactions among the valence quarks, antiquarks, and gluons.

Understanding the structure of nucleons and nuclei, as well as their properties such as spin, mass, and nucleon-nucleon interactions from the properties and dynamics of quarks and gluons is a central goal of nuclear science. Decades of work in high energy physics and nuclear physics to probe the nature of matter at the QCD level has revealed a rich tapestry with many detailed answers, but the most fundamental questions remain unsolved, entailing many opportunities for new discoveries. The Electron Ion Collider (EIC) is conceived with unique capabilities to explore this new realm of discovery for understanding the fundamental role of QCD in the observed structure of matter.

The dynamical interactions between quarks and gluons have profound consequences, such as the generation of the nucleon mass. They also result in a little explored domain of matter where gluons dominate the nuclear wavefunction. Hints of this domain have been seen in nuclear collisions at RHIC and the LHC where the nuclei collide at nearly the speed of light. Similar hints have been obtained from prior electron-proton scattering at HERA. The corresponding strong color fields are at the heart of many poorly understood emergent phenomena in QCD, such as confinement, properties of the quark gluon plasma, and the origin of nucleon spin. A quantitative study of matter in this domain of gluon dominance is a central goal of the EIC.

In the last two decades, nuclear physicists have developed new phenomenological tools that show promise of realizing tomographic images of the quarks and gluons inside polarized and unpolarized protons and neutrons. These tools are being utilized now and will be further refined in the next few years to study the valence quark and the start of the sea-quark region in the nucleon using the 12 GeV CEBAF at TJNAF and the COMPASS experiment at CERN, respectively. However, our knowledge of the nucleon will be far from complete without the investigation of the gluon dominated region within it. While high-energy polarized and unpolarized hadron-hadron collisions at RHIC and the LHC have

initiated the exploration of this gluon-dominated regime, the EIC will complement these studies by simultaneously bringing the precision of the well-understood electromagnetic probe, polarized beams, and high energies to the study of the gluon dominated region. As one increases the energy of the electron-nucleon collision, the deep inelastic scattering process probes regions of progressively higher gluon densities. However, the density of gluons inside a nucleon must eventually saturate to avoid an indefinite rise in the strength of the nucleon-nucleon interaction. How this exactly happens in QCD is unknown. Unambiguous evidence of this saturated gluon density has so far eluded us, although tantalizing hints at RHIC and the LHC have been observed. Experimental design limitations of the past are being specifically addressed in the design of the EIC in order to study this remarkable form of matter; this will be facilitated by electron collisions with heavy nuclei, where coherent contributions from many nucleons effectively amplify the probed gluon density.

The scientific goals and the machine parameters of the EIC were first agreed upon in deliberations at a community-driven program held at the Institute for Nuclear Theory (INT) [2]. They were further refined and summarized in the EIC White Paper [3]. The EIC science goals were set by identifying critical questions in QCD that remain unanswered despite the significant experimental and theoretical progress made over the past decades, and would remain unanswered unless the EIC is realized. Those science goals and the consequent machine parameters for the EIC were supported in the 2015 NSAC Long Range Plan (LRP) [4] leading to the recommendation for the EIC as the "highest priority new facility" to be constructed in the US by DOE's Office of Nuclear Physics.

The EIC machine design presented in this document addresses all the scientific goals that were identified by the broader community [2–5] as the most compelling questions in QCD that the future Electron Ion Collider must address. During 2017 an independent assessment of the science of EIC was conducted by a panel convened by the National Academies of Sciences, Engineering, and Medicine [1]. The report strongly endorses this program, noting that it addresses profound scientific questions central to nuclear physics research while also advancing U.S. leadership in accelerator science and technology.

In parallel to growing the science case addressed by the EIC, there has been a vibrant R&D program [6] developing the detector technologies needed for a state-of-the-art compact collider detector. Over the years several consortia have been established to address the challenges in tracking, calorimetry and particle identification detectors both at mid-, backward and forward rapidities. Following the trends from the Large-Hadron Collider (LHC) in data acquisition (DAQ) also at EIC one is investigating a free streaming DAQ, thus eliminating any trigger and providing a large potential for not yet anticipated physics ideas. In addition emphasis was given to integrate all the ancillary detectors along the lepton and hadron beamlines into the wider interaction region.

2.3 The Science Goals of the EIC and the Machine Parameters

In this section, we present a few selected topics among the set of compelling questions in QCD that led to the recommendation for construction of an EIC in the NSAC process, and

summarize the machine parameters that are needed to address them.

The key scientific questions that the EIC could address are:

1. How are the sea quarks and gluons, and their spins, distributed in space and momentum inside the nucleon? How do nucleon properties emerge from them and their interactions?

2. How do color-charged quarks and gluons, and jets, interact with a nuclear medium? How do the confined hadronic states emerge from these quarks and gluons? How do the quark-gluon interactions create nuclear binding?

3. How does a dense nuclear environment affect the quarks and gluons, their correlations and their interactions? What happens to the gluon density in nuclei? Does it saturate at high energy, giving rise to a gluonic matter with universal properties in all nuclei and even nucleons?

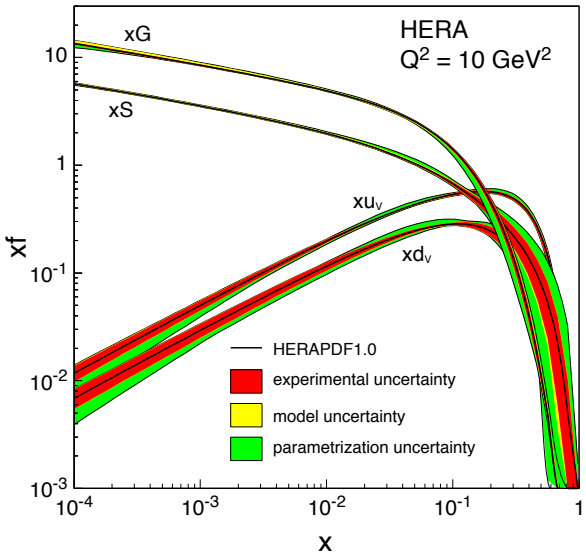

Figure 2.2: The gluon (xG), sea (xS) and valence quarks (x u_v and x d_v) distributions as extracted from the data collected at HERA along with their uncertainties. Domination of gluons at $x \leq 0.1$ is evident.

Figure 2.2 depicts the parton distribution functions extracted from *e+p* scattering data from the HERA collider at DESY. To leading order, these functions represent the probability density for finding a particle with a certain longitudinal momentum fraction x at resolution scale Q^2. The plots show the valence quark, sea quark, and gluon distributions extracted from the data. The most surprising feature of this result was the rapid rise of the gluon distribution with decreasing x, indicating that gluons dominate the proton's wavefunction at high energies.

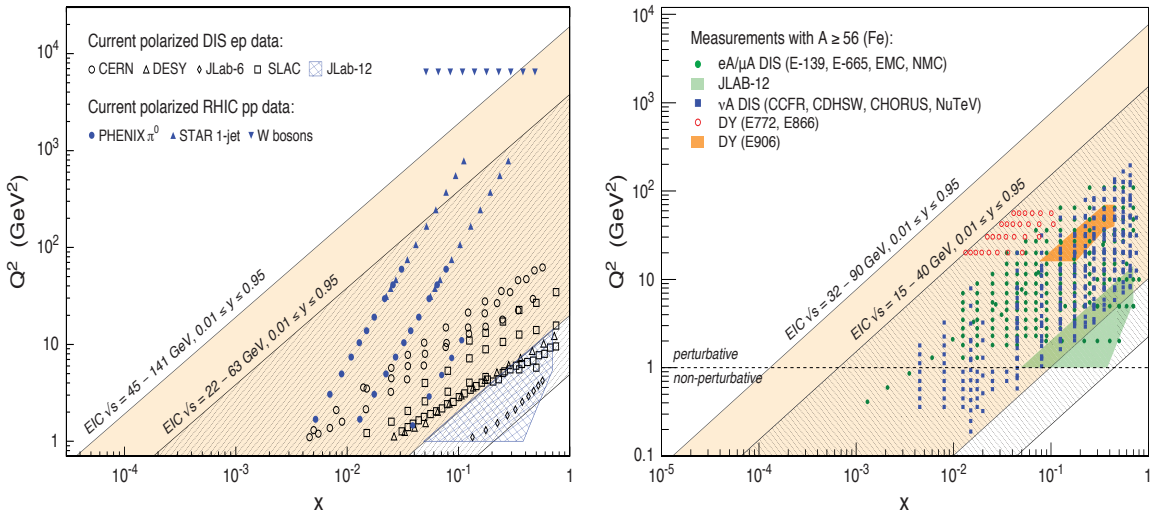

Figure 2.3: Left: The x-Q^2 range covered by the EIC with two different center-of-mass energy ranges in comparison with past and existing polarized e+p at CERN, DESY and SLAC and p+p experiments at RHIC. Right: the kinematic range in x-Q^2 for lepton-nucleus deep inelastic scattering and Drell-Yan (DY) experiments and future CEBAF 12 GeV experiments in comparison with the EIC.

The EIC design described in this document covers a center-of-mass energy range for the e+p collisions of $\sqrt{s}$ of 29 to 140 GeV. The kinematic reach in x and Q^2, the momentum transferred by the electron to the proton, is shown in Figure 2.3. The diagonal lines in each plot represent lines of constant *inelasticity*, y, which represents the ratio of the virtual photon's energy to the incoming electron's, in the target rest frame. The variables x, Q^2, y and s are related to each other by a simple equation $Q^2 = sxy$. Since the EIC is being designed to study the domain of gluon dominance in the proton, it has to have a substantial energy reach to access the low-x region ($x \propto 1/s$). The left figure shows the kinematic acceptance for polarized and unpolarized e+p collisions, and the right figure shows the acceptance for e+A collisions. Also shown for comparison is the reach of past and current fixed target facilities that acquire comparable data sets, and in case of the left plot, polarized p+p collisions from RHIC. Note that there are no data from past or current experiments in the region of $x < 5 \times 10^{-3}$. The two figures establish that the EIC would, for the first time, allow us to explore significantly lower values of x where the role of gluon degrees of freedom is enhanced.

The details of the science case for the EIC have been presented in the EIC White Paper [3]. In what follows, we describe, in greater detail, the compelling scientific questions outlined above, and motivate the requirements for the machine parameters that would help us address these questions.

2.3.1 Nucleon Spin and Imaging

Nucleon Spin

Understanding the nucleon spin in terms of its components, quarks, anti-quarks, gluons, and the dynamics resulting from color interactions, has been an important goal for nuclear scientists over the past five decades. The nucleon spin can be split into its components [7]:

$$\frac{1}{2} = \frac{1}{2}\Delta\Sigma(Q_f^2) + \Delta G(Q_f) + L_{Q+G}(Q_f) \tag{2.1}$$

where $\Delta\Sigma$, ΔG, and L are the contributions from quarks and anti-quarks, gluons, and their angular momentum to the nucleon spin. They are evaluated at a fixed scale Q_f and summed over the whole x range from 0 to 1. The discovery by the EMC experiment at CERN in the 1980s, that the quark and anti-quark spin alignment ($\Delta\Sigma$ in the equation above) could not explain the nucleon's spin, brought this fundamental issue into the limelight. Since then, numerous fixed target polarized electron/muon scattering experiments and polarized proton collisions at RHIC [8] have confirmed that the spin alignment of quarks+antiquarks, and gluons, in the covered kinematic region ($0.001 \leq x \leq 0.6$) does not explain the nucleon's spin, thus providing indirect evidence for a potential contribution from parton orbital angular momenta, L_{Q+G}. The largest uncertainties in $\Delta\Sigma$ and ΔG come from the unmeasured regions of $x < 5 \times 10^{-3}$, where no data exist. With measurements in this region, the EIC will provide precise measurements of $\Delta\Sigma$ and ΔG that will resolve the spin components of the proton [3, 5, 9].

Figure 2.4 illustrates the potential impact of the EIC on reducing the uncertainty in knowledge of the unmeasured region assuming the $\sqrt{s}$ range indicated in the figure. The EIC will significantly reduce the uncertainty in the knowledge of $\Delta\Sigma + \Delta G$ for $10^{-6} < x < 10^{-3}$ (y-axis), as well as in the contribution from orbital angular momentum in the range $10^{-3} < x < 1$ (x-axis). It is evident from this plot that the higher center-of-mass energy is required to make measurements for which the errors are much smaller than the individual contributions. For the EIC measurements of $\Delta\Sigma$ and ΔG inclusive DIS longitudinally polarized double spin asymmetries are necessary where the scale dependence of asymmetries measured at the same x but different Q^2 provides information to the gluon spin contribution.

In addition, the role of sea quark helicities and their contribution to the total spin has been only slightly addressed at moderate to high momentum fractions so far. In particular the role of strange quarks, an entire sea object, is still very unclear and has so far mostly been obtained via hyperon decay constants and the assumption of SU(3) flavor symmetry. Using those assumptions, a substantial negative contribution is found in global fits (reducing the contribution of $\Delta\Sigma$ to the proton spin) while no direct indication of such a behavior was seen in semi-inclusive DIS measurements so far. DIS measurements in which final-state hadrons are measured (in addition to the scattered electron), are commonly referred to as "Semi-Inclusive DIS" (SIDIS) measurements. Using SIDIS measurements at the EIC will enable the direct determination of the strange and other sea quark helicities with the help of fragmentation functions. Especially the fragmentation of partons into kaons, which

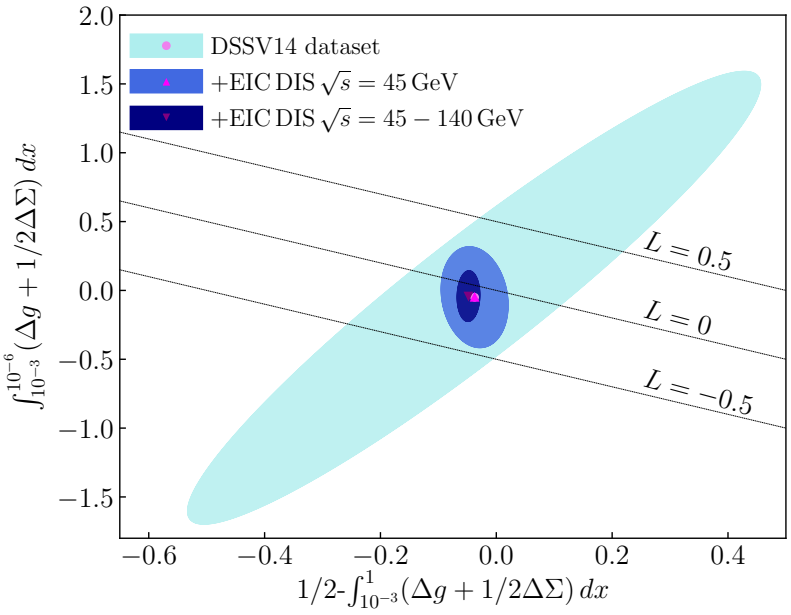

Figure 2.4: The impact of different center-of-mass energies on our knowledge of the sum of quark and gluons' helicity contributions in the range $10^{-6} < x < 10^{-3}$ (vertical axis) versus the contribution from the orbital angular motion in the range $10^{-3} < x < 1$ (horizontal axis). The calculations are shown at a fixed scale of $Q_f^2 = 10\,\text{GeV}^2$ [5].

contain a strange quark as valence flavor, enhances the sensitivity to the strange helicities. Figure 2.5 displays the expected uncertainties of various sea quark helicities as a function of x when not only including EIC DIS but also semi-inclusive DIS data. One can clearly see that the impact on the sea quark helicities greatly improves under the inclusion of SIDIS EIC data.

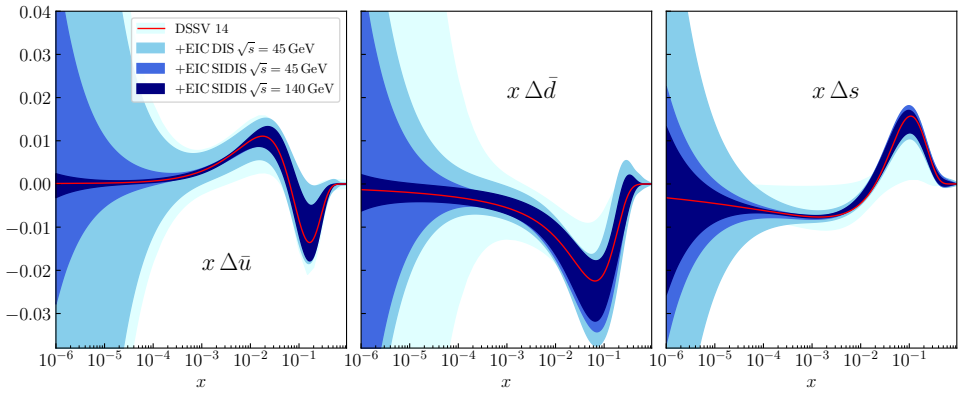

Figure 2.5: The impact of the EIC measurements on the sea quark helicity distributions as a function of x. From left to right, the anti u-quark, anti d-quark and strange quark helicities are displayed including their expected uncertainties. [10].

Machine and Detector Requirements For Polarized Inclusive and Semi-inclusive Deep Inelastic Scattering

Obtaining double longitudinal spin asymmetries require measuring inclusive deep inelastic scattering (DIS) with longitudinally polarized electrons off longitudinally polarized protons. Typically, 70% beam polarization was assumed in the conducted simulations. Most studies were performed assuming a data set with integrated luminosity $L = 10$ fb^{-1}, and it was shown in [5, 9] and references therein that the statistical uncertainties at this luminosity are considerably smaller than the current theoretical uncertainties. Experimental systematic uncertainties, coming from polarization measurements and other (time dependent, detector related) false asymmetries in measurements would then have to be constrained to a few percent [11]. Similar measurements using polarized ^{3}He or deuteron are needed to obtain full flavor separation of the spin structure. The machine requirements are similar to the ones discussed for the proton except for the need of neutron rich polarized nuclear beams. In addition, this science program will need high center-of-mass energies and an integrated luminosity of at least 10 fb^{-1}.

As will be discussed in more detail later, the scattered DIS leptons can be predominantly found in the backward endcap region, the central detector region and, at high x and Q^2, also the forward region. In the latter case using the total hadronic final state or combined methods are often required to determine the DIS kinematics well enough. Final state hadrons needed for the semi-inclusive measurements range from the forward regions with high momenta of up to 70 GeV at the higher collision energies to the backward endcap region and generally smaller momenta. For the flavor sensitivity to the sea quark helicities, pions and kaons need to be cleanly identified in the detector.

Imaging The Confined Motion Of Quarks

Experiments with collisions of electrons on transversely polarized protons, deuterons (D), or helium (^{3}He) targets, have measured single spin azimuthal asymmetries for various identified hadrons over a broad range of kinematics. Similar effects have been observed and studied in singly polarized p+p collisions. The commonly accepted origin of these asymmetries are the correlations between the transverse momentum of quarks and their spin, as well as the spin of the parent nucleons. Therefore a full picture of the nucleon has to include the transverse spin and momentum distribution of partons in addition to their longitudinal one.

SIDIS and polarized p+p measurements over the past decade, have allowed scientists to formulate a framework in which the measurements of single spin azimuthal asymmetries for different identified hadrons are connected to the transverse momentum distribution (TMD) of partons, *i.e.*, their confined motion inside the nucleon and to its transverse spin contribution. These TMDs incorporate the correlations between the motion of partons, their spin, and the spin of the parent nucleon. These correlations arise from spin-orbit coupling among the partons about which very little is known to-date. One can define eight types of TMDs [12] based on the different combinations of quark and nucleon spin

orientations, and a similar set of eight TMDs for gluons—all of which need to be mapped out if one is to gain full knowledge of the 3D momentum and spin structure of the nucleon. As these measurements mostly require hadrons in the final state, also similar sets of TMD fragmentation functions are involved in order to access these distributions.

The data sets used to constrain TMDs are currently more limited in x and Q^2 than the measurements shown in Figure 2.3 (left) used to constrain the helicity PDFs. With its polarized beams and high energy, the EIC will dramatically advance our knowledge of TMDs. One will be able to map out the 2+1 dimensional momentum structure of the different quark flavors and gluons inside nucleons over a wide region in x and Q^2 [3, 13].

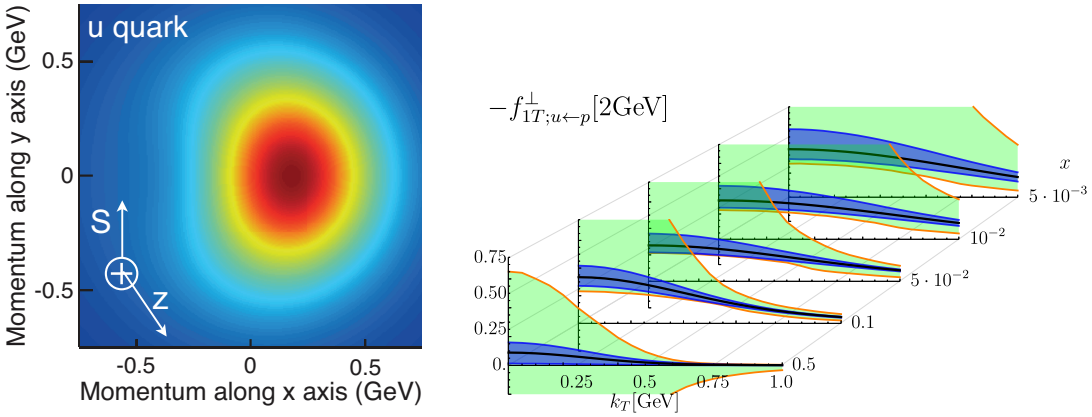

Figure 2.6: Left: The transverse momentum distribution of an up quark with longitudinal momentum fraction $x = 0.1$ in a transversely polarized proton moving in the z-direction, while polarized in the y-direction. The color code indicates the probability of finding the up quarks. Right: The transverse-momentum profile of the up quark Sivers function at five x values accessible to the EIC, and corresponding statistical uncertainties.

Figure 2.6 (left) depicts the transverse-momentum distribution of up quarks inside a proton moving in the z-direction (pointing out of the page) with its spin polarized in the positive y-direction. The colors represent the probability of finding the *up* quarks for the given momenta. The anisotropy in transverse momentum is described by the Sivers distribution function [3, 14, 15], which describes the correlation between the proton's spin direction and the motion of its quarks and gluons. While the figure is based on a preliminary extraction of this distribution from current, limited, experimental data and the expected precision at an EIC, nothing is known about the spin and momentum correlations of the gluons and sea quarks. The achievable statistical precision of the quark Sivers function from EIC kinematics assuming an integrated luminosity of 10 fb^{-1} is shown in Figure 2.6 (right). Currently no data exist for extracting such a picture in the gluon-dominated region in the proton or in light nuclei. For (sea)quark related Sivers function measurements semi-inclusive single spin asymmetries for certain azimuthal correlations of hadrons and nucleon spins around the virtual photon direction are required. To single out gluon processes to access the gluon Sivers function, nearly back-to-back pairs of jets or heavy flavor hadrons are required where the transverse spin dependent transverse momentum imbal-

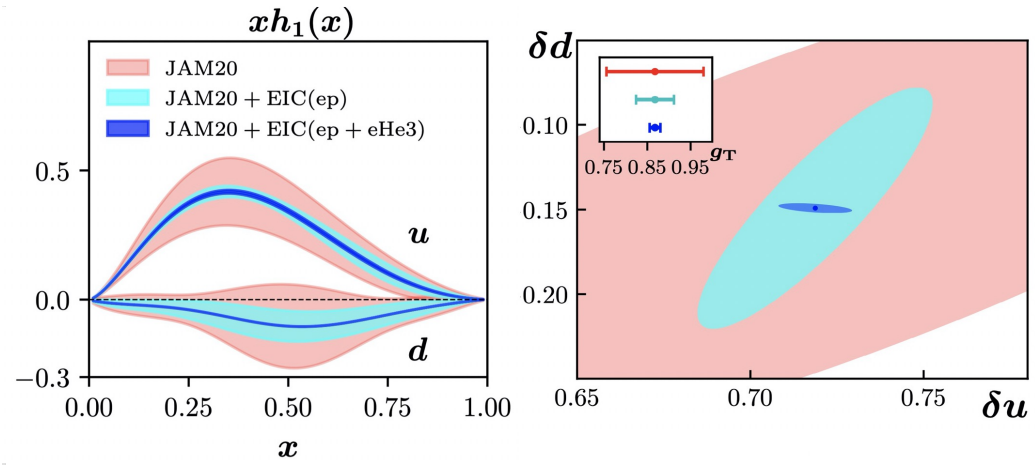

Figure 2.7: Expected up and down quark transversity distributions (left) and tensor charges (right) at an EIC in comparison to current extractions [16].

ance relates to the gluon Sivers function. The EIC will be crucial to realize such a program. Similarly important is the transverse spin distribution of quarks inside a transversely polarized nucleon which also requires the use of TMD or di-hadron fragmentation functions despite not being an explicitly transverse momentum dependent object itself. The integral over x is also called the tensor charge of the nucleon which may be connected to physics beyond the standard model. The current experimental precision is very limited and still requires various phenomenological assumptions, but the comparison of the tensor charges extracted from the EIC and from lattice QCD simulations may be sensitive to such physics. While the tensor charges are expected to be valence dominated, only the full integrals over a large range in x will remove the extrapolation uncertainties that current and future fixed-target measurements have and complement them. The expected precision on the transversity distributions and tensor charges for up and down quarks is shown in Figure. 2.7 in comparison to current extractions [16] with a precision that would exceed lattice calculations.

In addition to extracting the transverse spin and momentum picture of the nucleon, substantial theoretical interest lies in understanding the scale dependence of explicitly transverse momentum dependent functions. Unlike the collinear case that is well understood, there are plenty of open questions that can only be answered by a machine such as the EIC that has a large range of scales while covering transverse momenta from low, non-perturbative, to high, perturbative, regions.

Machine Requirements For TMD Measurements

Measurements of transverse momentum dependent distribution and fragmentation functions require longitudinally and transversely polarized hadron beams colliding with (un)polarized electrons. Simulations to investigate the degree to which the EIC can constrain the Sivers and other TMD functions assumed 70% transverse polarization of the

proton beam [3]. As mentioned earlier, semi-inclusive DIS implies the identification of final state hadrons in coincidence with the scattered electrons. There is already experimental evidence for flavor dependence, namely, a dependence on the type of quark involved in the collision, of the different TMDs. These measurements require that the hadron type in the final state be identified, in order to tag the flavor of the parton as up quarks are more likely to fragment into positive pions, down quarks into a negative pion and strange quarks into kaons. To obtain a detailed understanding of the eight different quark and gluon TMDs, one needs to bin the experimental observables in multiple variables, such as x, Q^2, y, p_T, z and $\phi_{S,h}$ simultaneously, where p_T is the hadron transverse momentum and z is the momentum fraction of the final state hadron, both with respect to the virtual photon. $\phi_{S,h}$ are the azimuthal angles of the incoming nucleon spin and the outgoing hadron around the virtual photon direction evaluated relative to the lepton scattering plane. The smooth coverage of all azimuthal angles for the given other kinematic variables requires a homogeneous detector with as little gaps as possible. Mapping the TMDs in multiple dimensions will require larger statistics than for inclusive measurements. To fully disentangle the flavor dependence of the various TMDs, it is important to collect data with neutron rich transversely polarized beams, such as ^{3}He or D with equivalent experimental conditions. Each of these collider operating modes will need an integrated luminosity (or significant fraction) of 10 fb^{-1}. There is an obvious redundancy in the data sets. For example, unpolarized target conditions could be achieved by combining oppositely polarized longitudinal or transverse data sets, thus running the collider effectively for two physics programs simultaneously. However, despite such opportune simultaneity in data taking, it is anticipated that the systematic program of measurements essential for the complete mapping of TMDs will require large collective integrated luminosities (a couple of 10 fb^{-1}) at various collisions energies for different hadron beams and their spin orientation [3]. The wide range in $x - Q^2$ provided by the EIC is essential for mapping the TMDs. To explore gluon TMDs, access to the gluon dominated low-x region is critical and requires both high energy ($\sqrt{s} \geq 100\,\text{GeV}$) and a large luminosity [13, 17].

Imaging the Transverse Spatial Distribution of Partons

As in the case of the transverse momentum distribution of partons inside a hadron, we know little about what a hadron looks like in transverse spatial dimensions. Many of our expectations are solely based on models. In some cases, it is expected that at large-x, the quantum numbers of the hadrons come from the struck partons in the DIS measurement. As one goes to low-x, and gluon distribution begins to saturate, its an interesting question of how gluons and sea quarks clump together in the hadron. At some yet unknown low-x a very high density gluon saturated region is reached [3, 5].

It is now possible to measure the transverse spatial distributions experimentally. The study of the spatial distribution of quarks and gluons requires a special category of measurements, that of exclusive reactions. Examples are deeply virtual Compton scattering (DVCS) and deeply virtual vector meson (DVVM) production. In these, the proton remains intact after the electron has scattered off, and a photon or a vector meson is produced. Exclusivity demands that all final state products are detected. This includes the scattered

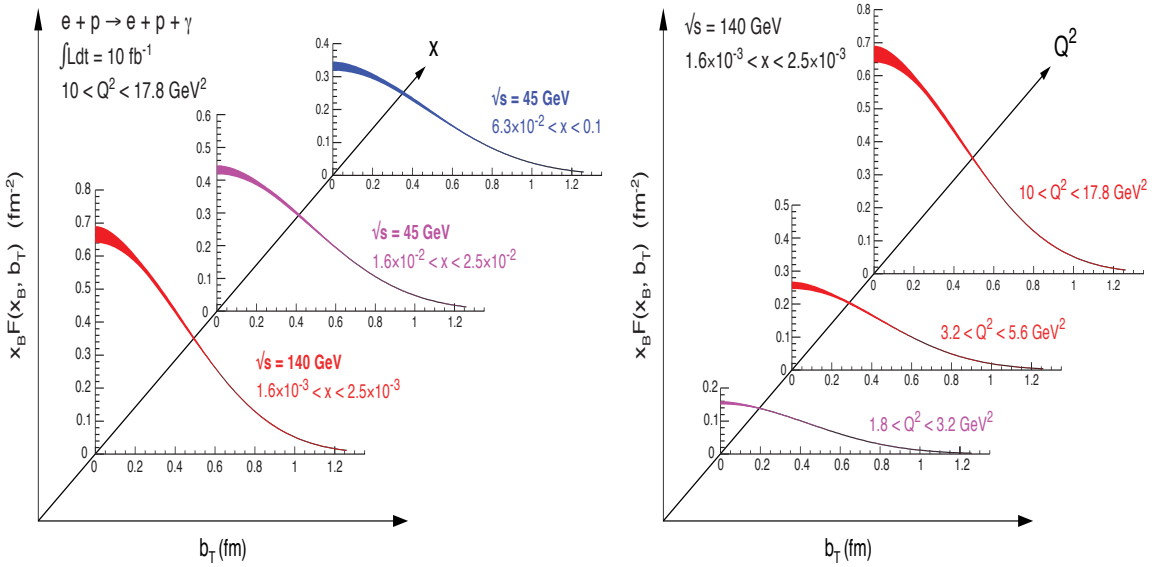

Figure 2.8: The projected precision of the transverse spatial distribution of partons obtained from the Fourier transform of the measurement of unpolarized DVCS cross section as a function of $|t|$ at the EIC for a targeted luminosity of $10\,\mathrm{fb}^{-1}$ at each center-of-mass energy. Impact parameter, b_T, is the distance from the center of the proton. Left: the evolution in x at a fixed Q^2 ($10 < Q^2 < 17.8\ \mathrm{GeV}^2$). Right: the evolution in Q^2 at a fixed x ($1.6 \times 10^{-3} < x < 2.5 \times 10^3$). The red and blue bands indicate extraction of spatial distribution only with high and low center-of-mass energies, respectively, while the purple band is accessible at both.

electron, the produced photon or vector meson, and the scattered proton. The spatial distribution of quarks and gluons in these experiments is extracted from the Fourier transform of the differential cross section with respect to the momentum transfer, t, between the incoming and the scattered proton. The non-perturbative quantities that encode the spatial distributions are called Generalized Parton Distributions (GPDs) [18–20]. They are interesting to nuclear scientists not only because of their fundamental importance in non-perturbative QCD, but also because the second moment of particular sets of quark and gluon GPDs will give us information about total quark and total angular momentum of quarks and gluons in the proton [21]. This spatial distribution yields a picture of the proton that is complementary to the one obtained from the transverse-momentum distribution of quarks and gluons.

Currently, our knowledge of GPDs from DVCS is limited and is based on fixed target experiments at intermediate to high-x or at low-x from the HERA collider measurements. The high-energy, high-luminosity EIC will make a very significant impact on these measurements. It is anticipated that measurements made for protons in the range $0.04 \lesssim t < 1.5\,\mathrm{GeV}^2$ will enable maps of parton distributions all the way down to 0.1 fm [5, 22]. Such exclusive measurements performed on nuclei will enable us to gain a deeper understanding of the transverse quark and gluon distributions within.

Figure 2.8 shows the precision with which an EIC will provide transverse spatial distribu-

tion for quarks [5]. The red and blue bands are reachable only with high or low energy collider operations, respectively, while the purple band is reachable by both. To reach low-x and high-Q^2 the EIC needs to have the higher center-of-mass energy. The measurements were simulated using an integrated sample of 10 fb^{-1}. The uncertainties shown in this plot only account for statistics and experimental systematics, not for the systematic uncertainties associated with the extraction of these quantities from data. For more about the extraction of proton size, we refer to [3, 5, 22].

Machine Requirements for GPD Physics

GPD physics is one of the most demanding in terms of luminosity as it requires multi-dimensional binning of very low cross-section processes. While it has been shown that an integrated luminosity of 10 fb^{-1} is sufficient to get to precise unpolarized spatial distribution functions, transverse spin asymmetry measurements that are sensitive to GPD E require 100 fb^{-1}. This amount of integrated luminosity will be necessary at several center-of-mass energies in order to cover the physics program outlined in the EIC White Paper [3] and high Q^2 and high x measurements will need the highest luminosity possible in to achieve a statistical precision comparable to the systematics uncertainties of the measurements.

The continuous measurement of t from $\sim$ 0.02 to about 1.5 GeV^2 demands a careful design of the interaction region to detect the forward going protons scattered under small angles combined with a careful choice of the hadron beam parameters, *i.e.*, angular divergence and large acceptance magnets. A complete map of the spatial distributions of quarks and gluons including polarization effects, requires high polarization of hadron and lepton beams [3, 22].

Pion and Kaon Form factors and structure functions

A recent addition to the physics program at the EIC originating from a series of workshops taking place since 2017 aims to study not only the sub-structure of the nucleon and nuclei, but extend it to the lightest bound states of the strong interaction, pions and kaons. As pions and kaons are unstable, their substructure could not be directly accessed via DIS and most of its limited information originates from secondary pion/kaon beam Drell-Yan measurements [23]. There is, however an opportunity to study their substructure using the Sullivan process [24, 25] where the lepton scatters not on the nucleon but on a virtual meson emitted from the initial nucleon and the remaining baryon is detected at very forward angles. The corresponding diagrams are displayed in Fig. 2.9 for elastic and deeply inelastic scattering on the meson.

The EIC allows to explore pion and kaon structure functions over a large QCD landscape in x and Q^2 to map the quark and gluon distributions in pions and kaons at a roughly similar level as for the proton when using only the HERA data. This would allow to give crucial insights to the understanding of mass. The vast majority of the proton mass is

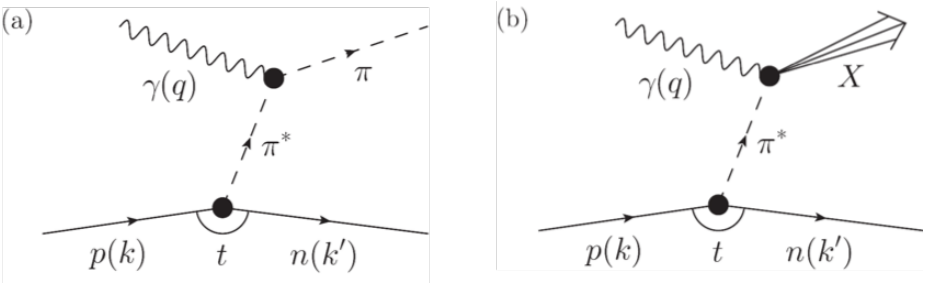

Figure 2.9: Diagrams depicting the scattering of the virtual photon on a virtual pion emitted from the nucleon a), elastically or b) deeply in-elastically.

emergent and due to quark-gluon interactions, and similar emergent-mass mechanisms must play a role in the pion and kaon. Yet the mass of the pion is only 140 MeV. This has led to speculation if the pion as viewed at high energies is full or empty of gluons. The EIC data will give unique insight in the emergent-mass mechanism and why the pion mass is so light. The kaon mass is ∼490 MeV and is at the boundary of the emergent- and Higgs-mass mechanisms, the latter responsible for the larger strange quark mass. Whether kaons viewed at high energies have less or more gluons in them than pions is unclear. The EIC will similarly allow access to the pion form factor to large values of Q^2 ∼35 GeV^2.

Machine requirements for pion/kaon substructure measurements

The debris of the meson and the scattered lepton can be detected by the central detectors. In the case of the virtual meson of the Sullivan process being a π^+, the resulting baryon is a neutron that can be detected by zero-degree calorimeters. When studying the kaon structure via this process, the forward-going baryon becomes a Λ and decays either into a π^--proton pair or a π^0-neutron pair. Detecting the charged particles is quite challenging but the neutral particles can be detected by a finely segmented zero-degree calorimeter. Due to the long life-time of the Λ, the lower collision energies are slightly favored in ensuring the decay before the ZDC. However, the larger angular spread of the forward-going baryons at lower energies would require a larger ZDC which could possibly interfere with accelerator elements.

Since only a small fraction of the nucleons emit a virtual meson and only small momentum transfers from the nucleon to the resulting baryon allow the interpretation in terms of a real pion, the highest luminosities are necessary.

2.3.2 Physics with High-Energy Nuclear Beams at the EIC

The nucleus is a QCD molecule, with a complex structure corresponding to bound states of nucleons. Understanding the formation of nuclei in QCD is an ultimate long-term goal of nuclear physics. With its wide kinematic reach, as shown in Fig. 2.10, the capability

to probe a variety of nuclei in both inclusive and semi-inclusive DIS measurements, the EIC will be the first experimental facility capable of exploring the internal 3-dimensional sea quark and gluon structure of a fast-moving nucleus. Furthermore, the nucleus itself is a unique QCD laboratory for discovering the collective behavior of gluonic matter at an unprecedented occupation number of gluons, for studying the propagation of fast-moving color charges in a nuclear medium to shed light on the mystery of the hadronization process, and to study of the quark-gluon origin of short range nucleon-nucleon forces in the nuclei.

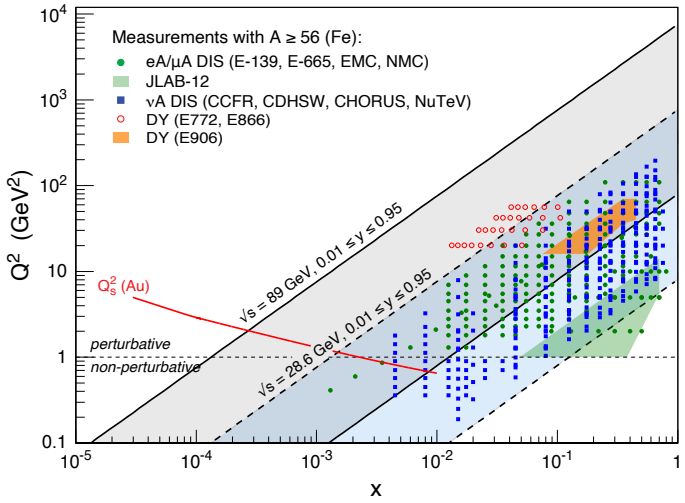

Figure 2.10: The range in the square of the transferred momentum by the electron to the nucleus, Q^2, versus the parton momentum fraction x accessible to the EIC in e+Au collisions is depicted for the highest and lowest center-of-mass energies available at an EIC. The data points reflect existing e+A data. The red curve illustrates the expected saturation scale $Q_s^2(x)$ for Au.

Study of High Gluon Density Matter

A key feature of gluon saturation is the emergence of a momentum scale Q_S, known as the saturation scale. If this scale is significantly larger than the QCD confinement scale Λ_{QCD}, the dynamics of strongly correlated gluons can be described using weak coupling many-body methods. The framework that enables such computations is called the Color Glass Condensate (CGC) [26]. The CGC predicts that $Q_S^2 \propto A^{1/3}$; thus, the novel domain of saturated gluon matter may be accessed sooner at a given energy in large nuclei (see Fig. 2.10). This regime of QCD is assumed to exist in all hadrons and nuclei when viewed at high energies where one is able to probe the low-x regime in full detail. Unambiguous establishment of this novel domain, and its detailed study, is one of the most important goals of the EIC.

QCD predicts that the saturation of gluons is achieved precociously in large nuclei, *i.e.*, at larger values of x than in the proton since the saturation scale Q_S^2 is enhanced by approxi-

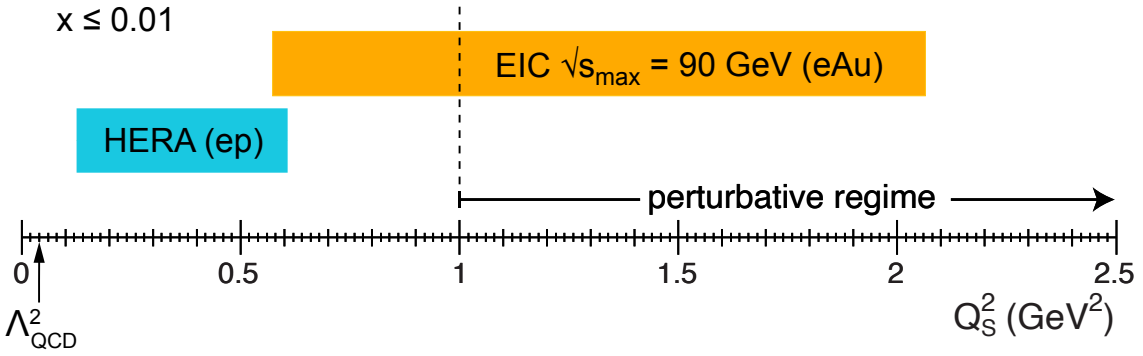

Figure 2.11: The accessible values of the saturation scale Q_S^2 at an EIC in e+A collisions compared to e+p collisions at HERA. In both cases maximum center-of-mass energies is assumed.

mately $A^{1/3}$. Figure 2.11 shows calculations for the saturation scales for the e+A collisions at maximum center-of-mass energies and for e+p collisions at HERA. Perturbative calculations can be performed reliably in the higher Q^2 region to the right of the dashed vertical line. It is in this region where $Q^2 > Q_S^2$ that DGLAP evolution can be reliably compared with the saturation calculations. Clearly, the saturation scales achievable at the EIC are significantly larger than those in e+p although the $\sqrt{s}$ energy for HERA was substantially larger. This enhancement of Q_s^2 in nuclei is a consequence of the high energy probe coupling coherently to all the partons along its path length in the nucleus. This figure makes the case that, to explore saturation phenomena reliably, one needs to have the largest nuclei at the highest possible center-of-mass energy.

While there are multiple experimental signatures of saturation discussed in the literature [3], we only use two in this section to motivate the requirement for the energy of the collider; these are dihadron suppression and diffraction in e+A collisions.

The dihadron correlation in the process $e + \mathrm{A} \rightarrow e' + h_1 + h_2 + X$ refers to the angular correlations between two hadrons h_1 and h_2. The angle between the two hadrons in the azimuthal plane is sensitive to the transverse momentum dependence of gluons as the parton shower develops, and to their interactions among themselves—the mechanism that leads to saturation. The experimental signature of saturation is a progressive suppression of the away-side ($\Delta\Phi = \pi$) correlations of hadrons with increasing atomic number A at a fixed value of x. A systematic comparison of the magnitudes and widths in the dihadron azimuthal distribution in e+p and e+A collisions at various energies should lead us to the appropriate conclusion about the existence of saturation [5, 27]. In the left plot in Fig. 2.12 (for details see [5, 27]), we plot the ratio of the correlations functions in e+Au to those in e+p for three energies. The suppression increases with increasing center-of-mass energy of 90 GeV. Since the typical uncertainties in saturation models are approximately equal to what would be a suppression of 20%, a significantly larger suppression ratio would be highly desirable, suggesting the highest possible center-of-mass energy is essential for establishing saturation unambiguously. The right plot in Fig. 2.12 depicts the corresponding

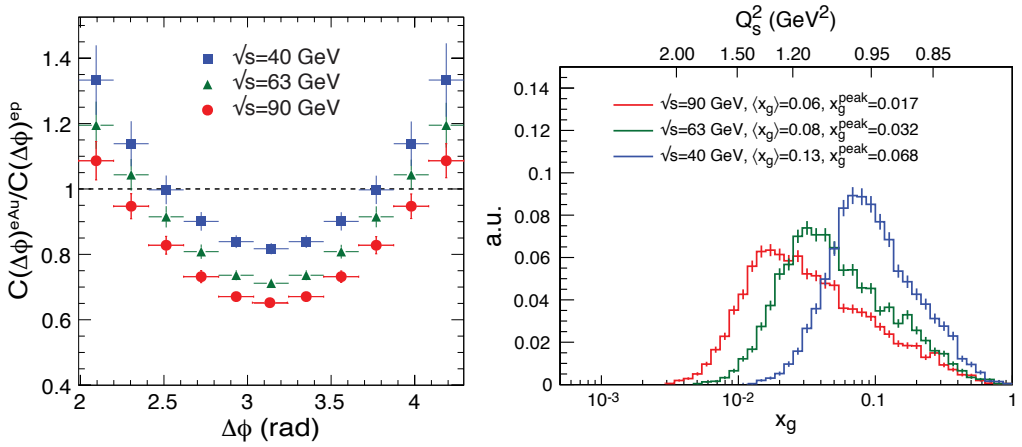

Figure 2.12: **Left:** Ratio of dihadron correlation functions in e+Au collisions to those in$e$+p collisions in a simulation study at three different center-of-mass energies. Ratio below 1 implies a suppression or disappearance of hadrons, which is statistically significant (and maximal) at $\Delta\phi = \pi$ radians. **Right:** x_g distributions probed by the correlated hadron pairs for the different center-of-mass energies in e+Au collisions. The average and peak values for the distributions are shown. The gluon saturation scales Q_s^2 corresponding to x_g values are displayed on top of the plot.

x_g distributions for dihadrons produced at the three different center-of-mass energies discussed. The larger the energy, the smaller the x_g values one can access, and the further we reach into the saturation regime. Since the saturation scale is a function of x_g alone, we also show the reference Q_s^2 values on the top of the plot.

Diffraction in e+A scattering is another promising avenue to establish the existence of saturation and study the underlying dynamics. Diffraction entails the exchange of a color neutral object between the virtual photon and the target. A consequence of this is a rapidity gap between the target remnant and the diffractively produced system. Conversely, if the exchanged particle is not color neutral, then in the detector one would observe a broad spray of final state hadrons filling up the rapidity gap. At HERA, these types of diffractive events made up a surprisingly large fraction of the total e+p cross section (10–15%). There are two explanations of such large diffraction cross-sections. One is the physics of saturation. The other is due to nonperturbatively shadowed diffractive structure functions that satisfy leading twist evolution equations. At EIC, the diffractive DIS off nuclei, saturation models predict that over 20% of the cross-section will be diffractive. In contrast, the perturbative QCD based leading twist shadowing (LTS) models do not predict any such enhancement. Since diffractive cross sections are proportional to the square of the nuclear gluon distribution, $\sigma \propto g(x, Q^2)^2$, they are very sensitive to the onset of gluon saturation, and are important for the study the gluon saturation.

Figure 2.13 illustrates this dramatic effects of gluon density saturation in e+A versus e+p collisions at an EIC. The plot considers coherent diffractive processes, defined to include all events in which the beam nucleus remains intact and feature a rapidity gap contain-

ing no produced particles. As shown in the figure, the fraction of such diffractive events are greatly enhanced by gluon saturation (the red points) in comparison with the predictions of shadowing model (the blue points). In all gluon saturation models, the coherent destructive multiple interaction among colored gluons suppresses both the coherent diffractive and total DIS cross-sections on nuclei compared to those on the proton, but, the suppression on the coherent diffractive events with the nucleus remained intact is much weaker than that of the total cross section leading to a dramatic enhancement in the double ratio as shown in Fig. 2.13. An early measurement of coherent diffraction in e+A collisions at the EIC would provide the first unambiguous evidence for gluon saturation.

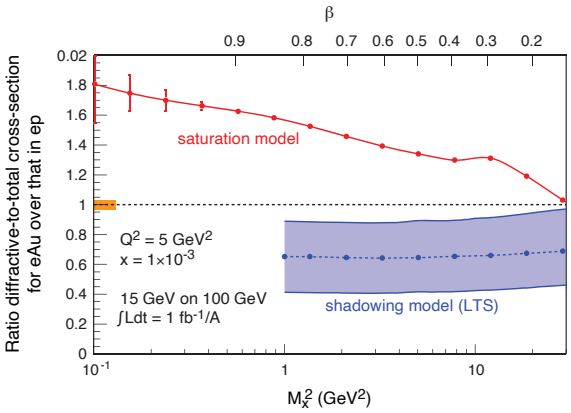

Figure 2.13: The ratio of diffractive over total cross-section for DIS on gold normalized to DIS on proton plotted for different values of M_X^2, the mass squared of hadrons produced in the collisions for models assuming saturation and non-saturation [3]. The statistical error bars are too small to depict and the projected systematic uncertainty for the measurements is shown by the orange bar. The theoretical uncertainty for the predictions of the LTS model is shown by the grey-blue band.

Machine Parameters For Studies of Gluon Saturation

Highest energy operation of the EIC with the heaviest nuclei will be an essential requirement for discovery of the gluon saturation. A detailed study of saturation beyond its discovery would require a systematic variation of the nuclear size and of $\sqrt{s}$ to see where the saturation sets in. Di-hadron correlation studies performed with an 10 fb^{-1}/A integrated luminosity are sufficient to get a clean signature. Such integrated data sets are also sufficient for many diffractive studies, and many of these measurements could be performed simultaneously for a particular nucleus. Some diffracting studies, like exclusive vector meson production will be more luminosity hungry since the require the measurement of multi-differential quantities. Running at the maximum energy is the most crucial requirement for this key EIC physics.

Nuclear Modifications of Parton Distribution Functions

When compared to our knowledge of parton distribution functions in the proton, our knowledge of nuclear PDFs (nPDF) is significantly more limited. Most of it comes from fixed target experiments in a region of intermediate to high-x as shown in Figure 2.10. Recently available data from the LHC have been included in nPDF extractions but have had limited impact on extracting nuclear PDFs [28]. High energy electron-nucleus collisions at the EIC will enable measurements of nuclear PDFs over a broad and continuous range in Q^2 all the way from photo-production ($Q^2 \sim 0$) to large Q^2 in the perturbative region. This will enable scientists to study the nPDFs with unprecedented precision. Precise knowledge of nPDFs will be crucial when searching for the transition between linear and non-linear evolution of the parton densities with change of the resolution scale of the probe. The latter saturation regime occurs at low-x and low interaction scale Q^2 where the gluon densities are highest and the recombination of low-x gluons becomes increasingly important. In e+A scattering such non-linearities are predicted to be more pronounced than in e+p interactions [29] due to an enhanced saturation scale Q_S^2.

Precision Measurements of Nuclear PDFs

Nuclear PDFs are dominantly determined through global fits to existing inclusive DIS data off nuclei using reduced cross-sections. The reduced cross section, σ_r, can be expressed in terms of the structure function F_2 and the longitudinal structure function F_L as:

$$\sigma_r = F_2(x, Q^2) - \frac{y^2}{1 + (1 - y)^2} \cdot F_L(x, Q^2) \tag{2.2}$$

While F_2 is sensitive to the momentum distributions of (anti)quarks and to gluons mainly through scaling violations, F_L has a larger direct contribution from gluons. An additional constraint on the gluon distribution at moderate to high-x comes from charm production driven by photon-gluon fusion. The fraction of charm production grows with the energy, reaching about $\sim$15% of the total cross section at the highest $\sqrt{s}$, thus permitting one to set a robust and independent constraint on the gluon distribution in nuclei at high-x [3,5].

Figure 2.14 shows the reduced cross section for inclusive and charm production in e+A scattering. The data were simulated using three different center-of-mass energies, 31.6, 44.7, and 89.4 GeV. The blue shaded region indicates the existing data, and grey bands indicate the uncertainty in the EPPS16 parameterization [28], the most up-to-date nPDF. Note that the estimated experimental uncertainties on the data are very small compared to theory uncertainties, and the higher center-of-mass energy enables a broader range in (x, Q^2), particularly in the low-x region where gluons dominate. Higher energies are clearly advantageous, and 10 fb^{-1}/A combined for the data at all center-of-mass energies will be sufficient to make significant impact on our knowledge of nuclear PDFs.

Figure 2.15 shows F_L for inclusive (left) and for charm (right) calculations based on EPPS16 along with the uncertainties estimated at each energy. Note that the measurement of F_L

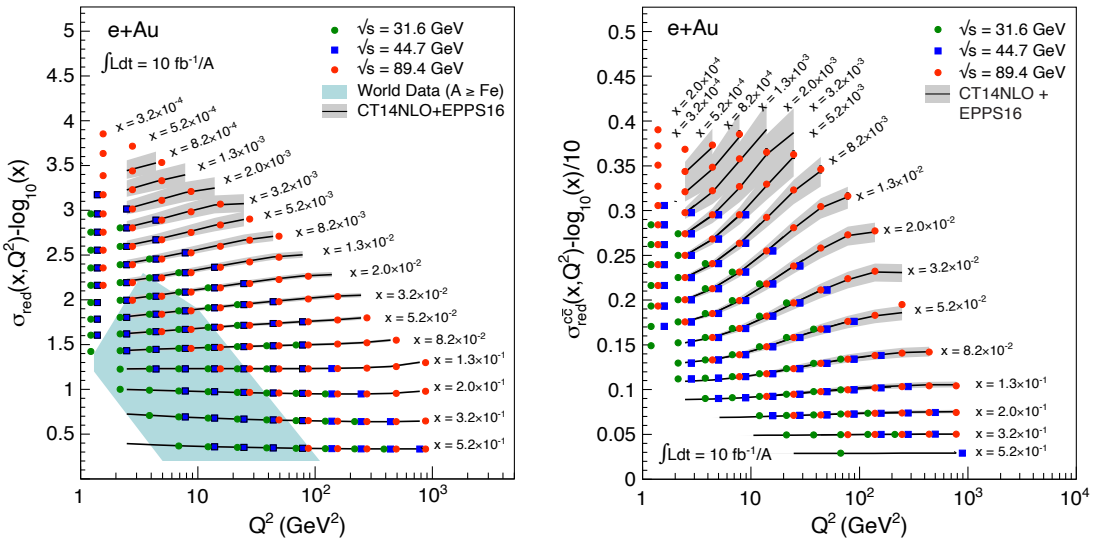

Figure 2.14: Reduced cross section for inclusive (left plot) and charm (right plot) plotted for x and Q^2 along with their uncertainties (shown in grey bands) from EPPS16 model. EIC simulated data [30] are shown for different center-of-mass energy combinations. The blue band in the left plot shows the currently available data.

requires one to operate the collider at several different center-of-mass energies. This simulation was performed with total of 10 fb^{-1} data over the combination of three center-of-mass energies [30]. The width of the gray bands reflects the current theoretical uncertainty in both cases and is wider than the statistical uncertainties from the simulations indicating that these uncertainty bands would be reduced significantly using future EIC data.

How parton distributions in nuclei are modified relative to those in the proton can be quantified by plotting their ratio normalized by the atomic number of the nucleus. The deviation of this ratio from unity is a clear demonstration that the nuclear parton distributions are not a simple convolutions of those in the proton. A depletion of this ratio is often called shadowing, while an enhancement is dubbed anti-shadowing. The reduced cross-sections of simulated EIC data was used together with existing world-data in a global fit to evaluate the level of improvements of gluon PDFs the EIC will provide [30]. The study allowed for additional flexibility in the fit function (EPPS16*) used to derive the gluon PDF in the nuclei in order to better evaluate the EICs impact. Figure 2.16 shows the ratio of gluon distribution in Pb to that in proton plotted at two different values of Q^2. The grey bands indicate the current uncertainties in the nuclear PDFs, orange bands indicate the improvement we could expect from the inclusive data sets, and the hatched band indicates the further improvement one expects from the inclusion of charm quark production in this analysis. Including charm quarks in the analysis helps significantly in the large-x region, where they are produced abundantly through the photon-gluon fusion process [5, 30].

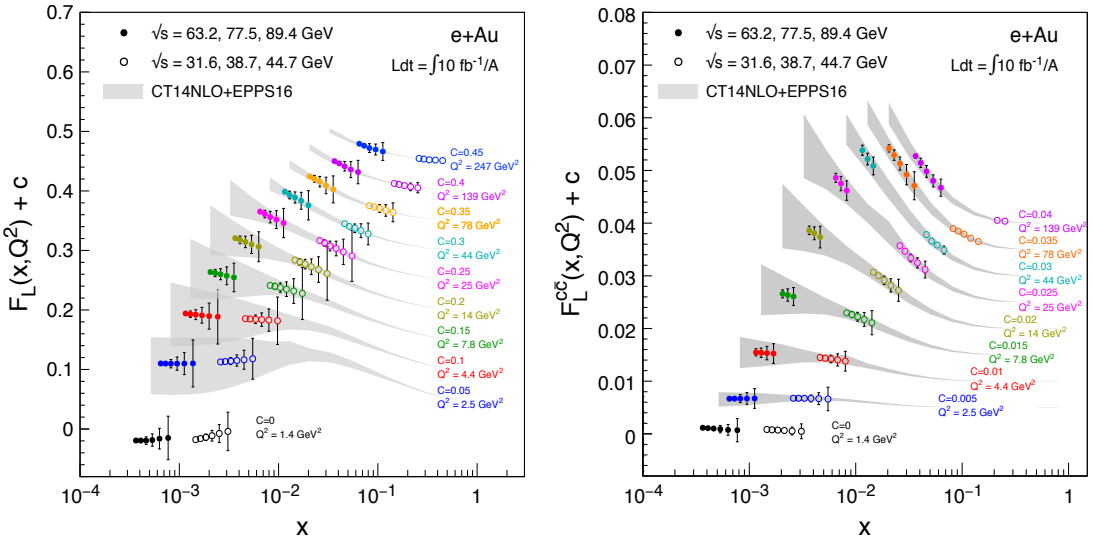

Figure 2.15: Inclusive F_L (left plot) and charm (right plot) $F_L^{c\bar{c}}$ simulated data [30] shown with the EPPS16 nuclear PDFs. Grey bands are uncertainties in the model, and the EIC data simulated with $10\,\mathrm{fb}^{-1}/\mathrm{A}$ are shown for three center-of-mass energies.

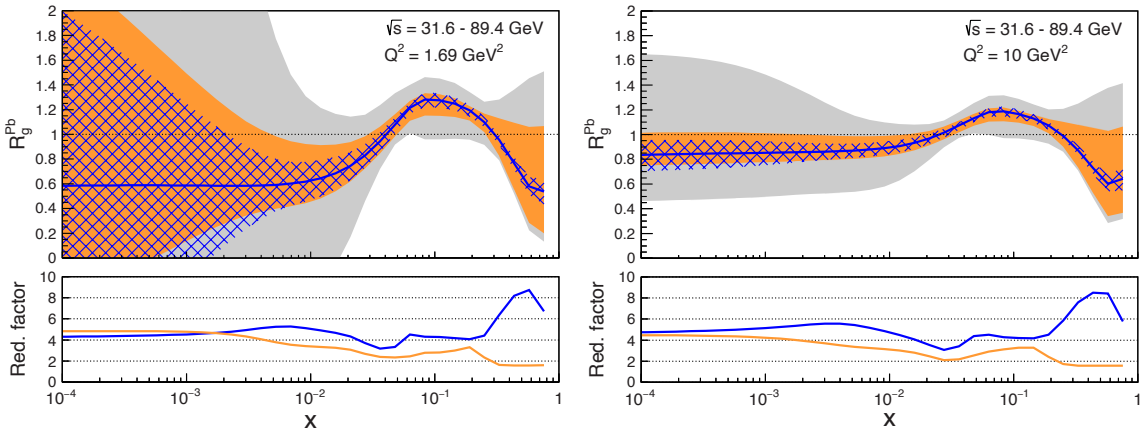

Figure 2.16: Nuclear PDFs improvements with the EIC. The ratio R_g^{Pb}, from EPPS16*, of gluon distributions in a lead nucleus relative to the proton at $Q^2 = 1.69\ \mathrm{GeV}^2$ (left) and $Q^2 = 10\ \mathrm{GeV}^2$ (right). The grey band represents the EPPS16* theoretical uncertainty. The orange (blue hatched) band includes the EIC simulated inclusive (charm quark) reduced cross-section data. The lower panel in each plot shows the reduction factor in the uncertainty with respect to the baseline fit.

Machine Parameters For Precision Nuclear PDF Measurements

Based on recent studies for inclusive DIS and charm cross section measurements [30], large $\sqrt{s}$ presents a significant advantage, as a wider x-Q^2 coverage can be explored and one reaches further in the region of gluon dominance. For precise high impact measurements an integrated luminosity of 10 fb^{-1}/A is sufficient. In fact, beyond a few fb^{-1}, these measurements become systematics dominated and more statistics will not affect the overall uncertainties.

2.3.3 Passage of Color Charge Through Cold QCD Matter

Figure 2.17 shows a schematic of an e+A scattering event. The virtual photon transmits the energy from the electron and interacts with a quark inside a nucleon in the nucleus. The struck quark will subsequently traverse the nucleus, interacting with the color charges inside the nucleus and continually lose energy. At some point, this quark will hadronize and form a color neutral hadron. Whether the hadronization process happens inside or outside the nucleus depends on the interplay between the energy of the quark and the atomic number of the nucleus.

If the virtual photon energy (in the nuclear rest frame) is large, the quark that is kicked will have a large energy and produces a jet. Measuring the jets experimentally gives several advantages in comparison to leading hadron studies. Reconstructed from multiple (ideally all) final state particles produced by hadronization of the scattered parton, jets are much closer proxies for the parton kinematics than any single particle observable. Using jets in many cases removes (or minimizes) hadronization uncertainties. On the other hand, jets are composite objects with rich internal substructure encoding shower evolution and hadronization details.

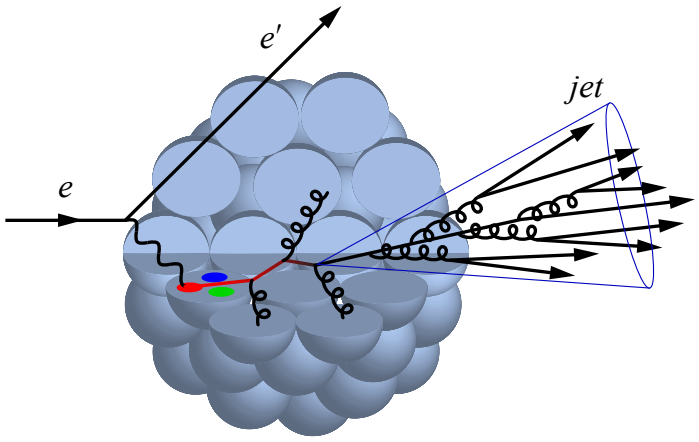

Figure 2.17: Schematic depiction of a struck parton propagating through cold nuclear matter resulting in the formation of a single jet.

Jets are versatile tools for experimental studies at hadron-hadron and lepton-hadron colliders, addressing variety of physics topics from precision measurement of the Standard Model processes to searches beyond Standard Model and transport properties of quark gluon plasma. The methodology of jet reconstruction and underlying background handling is rapidly developing at the modern collider facilities, on par with the progress in theoretical understanding of emerging jet data at the next-to-next-to-leading order for many channels. The experience thereby gathered can be gainfully applied to physics at the EIC, and without a doubt jets will be indispensable in the next chapter of collider experiments to be written there. At the EIC the jet will be an effective tool to be employed to measure and study the hadronic component in high energy photon structure [31] and gluons' helicity in polarized protons [5]. Jet measurements will also contribute to constraining polarized and unpolarized parton distribution functions, probing gluon transverse momentum dependent distributions, and most relevant for this section, to studies of QCD hadronization, shower evolution, and cold nuclear matter effects.

Several recent works [32,33] detail the feasibility and applications of jet studies at the EIC. The jet kinematic distributions, including inclusive jet transverse momentum and pseudorapidity spectra, and dijet mass and pseudorapidity distributions, were quantified for a range of Q^2 values, processes, and beam energies. The energy contribution from underlying event activity was also studied as a function of jet energy [32], and while for energetic jets, the underlying event contributions are found small, at lower jet energies, these contributions are found to have a fractionally significant effect. Some of these studies are also incorporating expected detector performance. They show that the best jet reconstruction performance can only be achieved at sufficiently high energies, and thus high center-of-mass energy collisions are vital for jet studies.

Energetic jet born by scattered parton encodes the history of multiple interactions with the target nucleus, which generate p_T-broadening. Thus, a comparison of the cross-section in e+p and e+A collisions is expected to be sensitive to in-medium broadening effects. Several key measurements relying on jets were identified for their sensitivity to parton energy loss in the nucleus [33], together with developments of new tools for controlling hadronization effects. Among such measurements are several variables assessed via lepton-jet correlations, including the ratio of the electron to jet transverse momenta, and a relative azimuthal angle between the measured jet and electron. These measurements will allow constraining parton transport coefficient in the nuclei [34]. The lepton-jet correlations are measured in the lab-frame and could be compared directly to the similar measurements at RHIC and LHC elucidating the hot and cold nuclear matter effects on propagating parton.

It is expected that the variability of energy of the collider and the "dialing" of the nuclear size, both of which are possible with the EIC, will allow us to study the emergence of jets as a function of energy, and to study the internal spatial structure of jets systematically as an additional topic of high interest. Studying how jet substructure is modified between e+A and e+p collisions could provide additional information about details of how partons lose energy in the cold nuclear medium. A comparison of jet properties in e+A versus e+p collisions is thus a promising avenue to study a broad set of QCD phenomena related to the passage of color through cold QCD matter and the hadronization/fragmentation

processes.

In addition to jet studies, identified hadron measurements will provide additional experimental avenue for detailed understanding of cold-QCD effects of color-charge. Parton propagation through cold nuclear matter and its' effects on hadronization have been previously studied by the HERMES collaboration in semi-inclusive deep-inelastic scattering on nuclei via relative hadron production cross-sections for various light-flavor particle species. These most precise measurements to date left room for different modeling of hadronization dynamics and in-medium attenuation. EIC experiments will be able to extend these light-flavor cross-section measurements into new kinematic domains and augment these studies with heavy flavor mesons. Recent theoretical works [35] highlighted the sensitivity of D- and B-meson production to the transport properties of cold nuclear medium. Studies of the medium-induced suppression patterns of heavy hadrons are shown to have high discriminating power for theoretical models of energy loss and hadronization in nuclear matter. In addition to inclusive hadron and jet production measurements, mapping the modification of heavy flavor production in reactions with nuclei of different sizes will provide an experimental handle for understanding transport properties of nuclear matter.

Machine Design Parameters For Jets Studies

Jets can only be produced and identified cleanly at high enough collider energies. High momentum jets feature higher hadron multiplicity and a more complex internal structure. As such, high center-of-mass energy is vital for jet studies. Nuclear size is an essential control variable in these experiments and a broad range from light to heavy nuclei would be desired for systematic studies of energy loss in a nuclear medium. It is imperative to have matching beam energies for e+p and e+A collisions to avoid extrapolation related uncertainties and deliver most precise measurements of nuclear effects.

2.4 Summary of Machine Design Parameters for the EIC Physics

Here we summarize the machine requirements that were motivated in the previous section through a set of key measurements that reflect the highlights of the EIC science program. The important machine design parameters were originally discussed in great detail in section 1.2 of the EIC White Paper [3]. The successful scientific outcome of the EIC depends critically on: (a) the luminosity, (b) the center-of-mass energy and its range, (c) the lepton and light ion beam polarization, and (d) the availability of ion beams from deuteron to the heaviest nuclei. Two interaction regions are desired to ensure a robust physics program with complementary detector systems.

Luminosity

In the discussion of each physics topic in the previous section we quoted the integrated luminosity needed to perform the corresponding measurements. The EIC is being designed to achieve peak luminosities between 10^{33-34}cm^{-2} sec^{-1}. To put these numbers into context, note that a luminosity of $10^{33}\text{cm}^{-2}\text{s}^{-1}$ and strong hadron cooling ($L_{\text{peak}} = L_{\text{avg}}$) yields an integrated luminosity of 1.5 fb^{-1} per month. Here we assume an 60% operations efficiency for the collider complex as routinely achieved by RHIC. Without strong hadron cooling for the same operations parameters, one would get a 30% reduction, as the average luminosity L_{avg} per fill is reduced to 70% of the peak luminosity L_{peak}. Most of the key physics topics discussed in the EIC White Paper [3] and summarized here are achievable with an integrated luminosity of 10 fb^{-1} corresponding to 30 weeks of operations. One notable exception is the study of the spatial distributions of quarks and gluons in the proton with polarized beams. These measurements require up to a integrated luminosity of 100 fb^{-1} and would therefore benefit from an increased luminosity of 10^{34}cm^{-2} sec^{-1}. It should be noted that many measurements can be performed simultaneously by judiciously choosing beam species and their spin orientation appropriately.

Center-of-Mass Energy

To ensure a wide kinematic reach and large coverage of the phase space, the EIC requires a variable center-of-mass energy $\sqrt{s}$ in the range of $\sim 20 - 100$ GeV, upgradable to 140 GeV [3]. An energy of $\sqrt{s_{eN}} = 140\,\text{GeV}$ is needed to provide sufficient kinematic reach into the gluon dominated regime. Some measurements require a variation in $\sqrt{s}$. The lower center-of-mass energy range is driven by the ability to measure well transverse quantities, which are of the order of 10-100 MeV. This is important for example for the accurate determination of quark TMDs at high values of Q^2.

Polarization of beams

EIC Physics involves two types of asymmetries: (*i*) double spin asymmetries, requiring both electron and hadron beams to be polarized, and (*ii*) single spin asymmetries, requiring only one beam—typically the hadron beam—to be polarized. The statistical uncertainties for spin asymmetries are strongly affected by the degree of polarization achieved. For double spin asymmetries the dependence is $\delta A_{LL} \sim 1/\left[P_e P_p \sqrt{N}\right]$ and for single spin asymmetries $\delta A = 1/\left[P\sqrt{N}\right]$. Therefore, high beam polarizations are mandatory to reduce the statistical uncertainties. Measurements require longitudinal and transverse polarization orientation for protons, deuterons, ^{3}He and other polarizable light nuclei, as well as longitudinal polarization for the electron beam.

Nuclear Beams

Ion beams of the heaviest nuclei (Gold, Lead, or Uranium) combined with the highest $\sqrt{s}$, will provide precocious access to the domain of saturated gluon densities and to understand how color propagates through nuclear matter. Light ions are essential to study the A-dependence of gluon saturation and for precision studies of short range nuclear correlations.

2.5 Scientific Requirements for the Detectors and IRs

The physics program of an EIC, imposes several challenges on the design of a detector and, more globally the extended interaction region as it spans center-of-mass energies from 29 GeV to 141 GeV, different combinations of both beam energy and particle species, and several distinct physics processes. The EIC science program can be categorized in different general processes as shown in Table 2.1.

Table 2.1: Different categories of processes measured at an EIC.

Inclusive DIS: $e + p/\mathrm{A} \longrightarrow e' + X$; for this process, it is essential to detect the scattered electron, e', with high precision. All other final state particles (X) are ignored. The scattered electron is critical for all processes to determine the event kinematics.	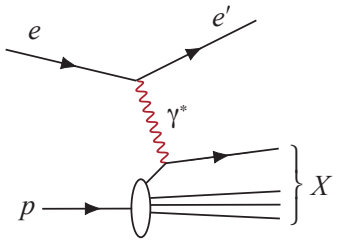
Semi-inclusive DIS: $e + p/\mathrm{A} \longrightarrow e' + h^{\pm,0} + X$, which requires detection of *at least one* hadron in coincidence with the scattered electron.	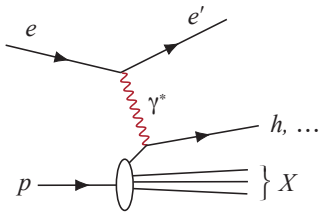
Exclusive DIS: $e + p/\mathrm{A} \longrightarrow e' + p'/A' + \gamma/h^{\pm,0}/VM$, which require the detection of *all* particles in the event with high precision.	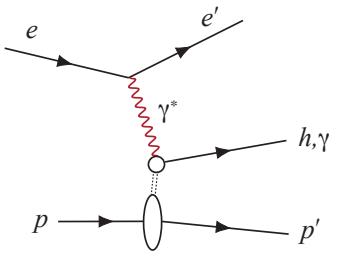
Electro-weak processes: $e + p/\mathrm{A} \longrightarrow \nu + X$; at high enough momentum transfer Q^2, the electron-quark interaction is mediated by the exchange of a $W^{\pm}$ gauge boson instead of the virtual photon. In this case the event kinematic cannot be reconstructed from the scattered electron, but needs to be reconstructed from the final state particles.	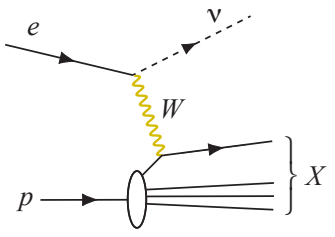

The directions of the beams are defined following the convention used at the HERA collider at DESY: the hadron beam travels in the positive z-direction/pseudo-rapidity and the electron beam travels in the negative z-direction/pseudo-rapidity. We call the hadron going direction the forward region and the electron going one the backward region.

2.5.1 Scientific Requirements for the Detectors

In this section we focus on the scientific requirements on a general purpose detector, which is fully optimized to address the full range of EIC physics. These requirements substantially affect the design of the interaction region. All the different physics processes to be measured at an EIC require having the event and particle kinematics $(x, Q^2, y, W, p_t, z, \Phi, \theta)$ reconstructed with high precision. The key variables x, Q^2, y, and W are either determined from the scattered electron or from the hadronic final state using the Jacquet-Blondel method [36]. In order to access the full $x - Q^2$ plane at different center-of-mass energies and for strongly asymmetric beam energy combinations, the detector must be able to reconstruct events over a wide span in rapidity and scattering angle. This imposes requirements on both detector acceptance and resolution. In contrast to symmetric energy colliders without good coverage of the rapidity range $|y| > 2$, where a significant fraction of the $x - Q^2$ phase space will be missed, this puts much more emphasis on the lepton and hadron endcap. Figure 2.18 illustrates the correlation between pseudo-rapidity / scattering angle and the $x - Q^2$ phase space.

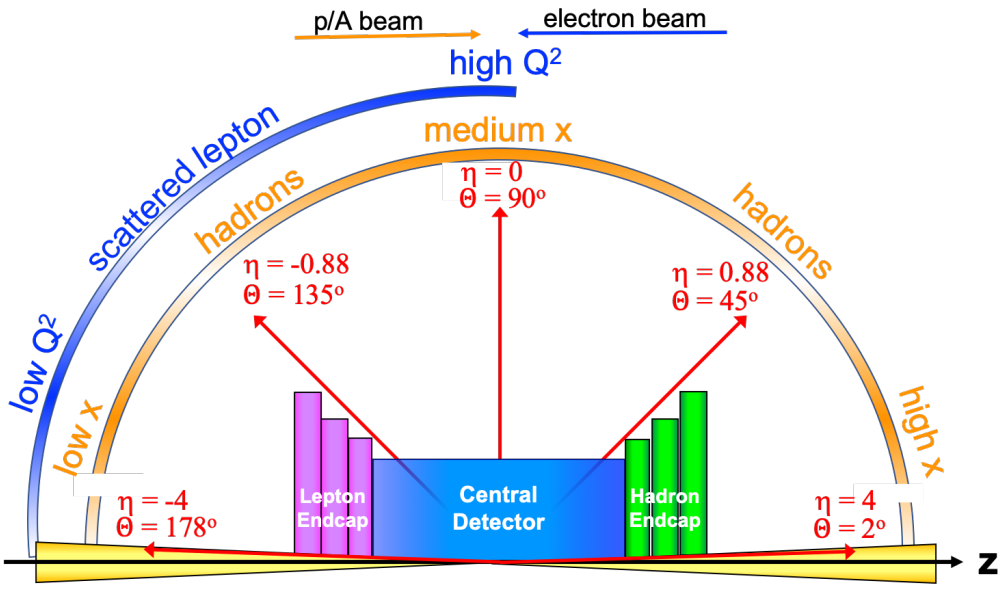

Figure 2.18: A schematics showing how hadrons and the scattered lepton for different $x - Q^2$ are distributed over the detector rapidity coverage.

Methods of Event Kinematic Reconstruction

It is common to reconstruct the event kinematic in DIS with different methods depending on the region of inelasticity y one is accessing. At large inelasticity y, where radiative corrections become large, as illustrated in Fig. 7.25 in [2] and the kinematics of the event is reconstructed from the scattered electron, there are two ways to address this: one is to calculate radiative corrections and correct for them; the other is to utilize the hadronic activity in the detector together with cuts on the invariant mass of the hadronic final state, which will reduce the impact of radiative corrections to a minimum. At small lepton scattering angles or correspondingly small inelasticity radiative corrections are small, but the momentum and scattering angle resolution for the scattered lepton deteriorates. This problem is addressed by re-constructing the lepton kinematics purely from the hadronic final state using the Jacquet-Blondel method or using a mixed method like the double angle method [36], which uses information from the scattered lepton and the hadronic final state. At HERA, these methods were successfully used down to y of 0.005. The main reason this hadronic method renders better resolution at low y follows from the equation $y_{JB} = (E - p_z^{had})/2E_e$, where $(E - p_z^{had})$ is the sum over the energy minus the longitudinal momentum of all hadronic final-state particles and E_e is the electron beam energy. This quantity has no degradation of resolution for $y < 0.1$ as compared to the electron method, where $y_e = 1 - (1 - cos\theta_e)E'e/2E_e$. To allow for efficient unfolding of measured quantities, i.e. cross sections and asymmetries, for smearing effects due to detector resolutions and radiative events and retain the statistical power it is important to have a survival probability in each kinematic bin of $\sim$80% or better. Typically, one can reach for a given center-of-mass energy squared, roughly a decade of Q^2 at fixed x when using only the electron method to determine the kinematics, and roughly two decades when including the hadronic or double angle method. If only using the electron method, one can increase the range in accessible Q^2 by lowering the center-of-mass energy. The coverage of each setting is given by the product of y times s. As lower y_{min} that can be reached, the fewer settings in s are needed. However, this is an important consideration for any measurement, which needs to separate the cross-section components due to longitudinal and transverse photon polarization, i.e. the measurement of F_L where one needs to have full y-coverage at all energies.

Inclusive and Semi-inclusive DIS

Scattered Lepton: To minimize the energy loss and multiple scattering of the scattered electron and not to degrade the resolution of the kinematic variables (x, Q^2, y, W) derived from the scattered electron, *the beam pipe needs to be as thin as possible and made from a low mass material, i.e. Beryllium.* As discussed in Section 2.3.2, the study of non-linear QCD effects at the largest gluon densities requires electron-nucleus (i.e. U, Pb, Au) collisions at the highest center-of-mass energies. At the EIC, this implies 18 GeV electrons colliding with heavy ion beams of 110 GeV to reach $Q^2 < Q_s^2$ ($\sim$1 GeV^2) at the lowest x possible. Figure 2.19 shows the relationship between Q^2 and pseudo-rapidity of the scattered electron. To reach $Q^2 \sim 1\,\text{GeV}^2$, the scattered electron needs to be detected down to a pseudo-rapidity of $\eta = -4$ corresponding to an angle of 2° off the beam line. The electron scattering angle

especially at low Q^2 is independent of the hadron beam energy.

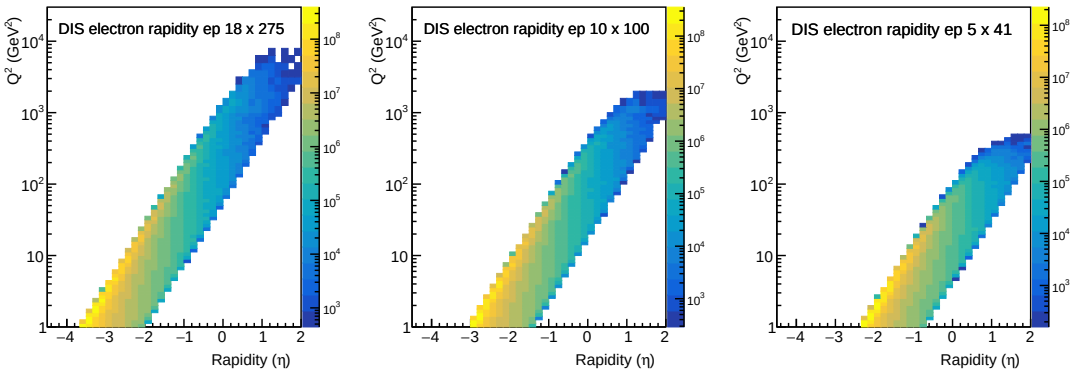

Figure 2.19: Q^2 vs. pseudo-rapidity in the laboratory frame for the scattered electron at different center-of-mass energies. The following cuts have been applied: $0.01 < y < 0.9$, with inelasticity, y, defined as the fraction of the electron's energy lost in the nucleon rest frame. The electron scattering angle especially at low Q^2 is independent of the hadron beam energy.

Figure 2.20 (upper row) illustrates the dependence between the momentum of the scattered lepton and its scattering angle for three different center-of-mass energies. It is clearly shown that as higher the center-of-mass energy the more the lepton goes in the original electron beam direction, corresponding to negative pseudo-rapidity and such very small scattering angles with respect to the beam axis. Varying the hadron beam energy for a fixed lepton beam energy has no influence on the scattered lepton pseudo-rapidity/scattering angle correlation. Several EIC physics topics require going to low x at low Q^2 such an EIC detector needs to have good electron identification and momentum/energy measurement at pseudo-rapidities < -2, which means detecting the scattered lepton 2° of the beam axis with an energy close to the lepton beam energy. *As such, no collider equipment can be installed inside the main detector volume and extend beyond* 1.5°.

Hadron Kinematics: Figure 2.20 (lower row) shows the momentum versus pseudo-rapidity / scattering angle distributions in the laboratory frame for pions originating from semi-inclusive reactions for different lepton and proton beam energy combinations. For the lowest center-of-mass energy, pions are scattered in the forward (ion) direction. With increasing center-of-mass energy, the pions increasingly populate the central region of the detector. At the highest center-of-mass energy, pions are even largely produced going back-ward (i.e. in the lepton beam direction). For increasing hadron beam energies at fixed lepton beam energy the pseudo-rapidity distribution remains the same but the maximum hadron momentum increases at fixed pseudo-rapidity. The kinematic distributions for kaons and protons/anti-protons are essentially identical to those of the pions. The distributions for semi-inclusive events in electron-nucleus collisions may be slightly altered due to nuclear modification effects, but the global features will remain.

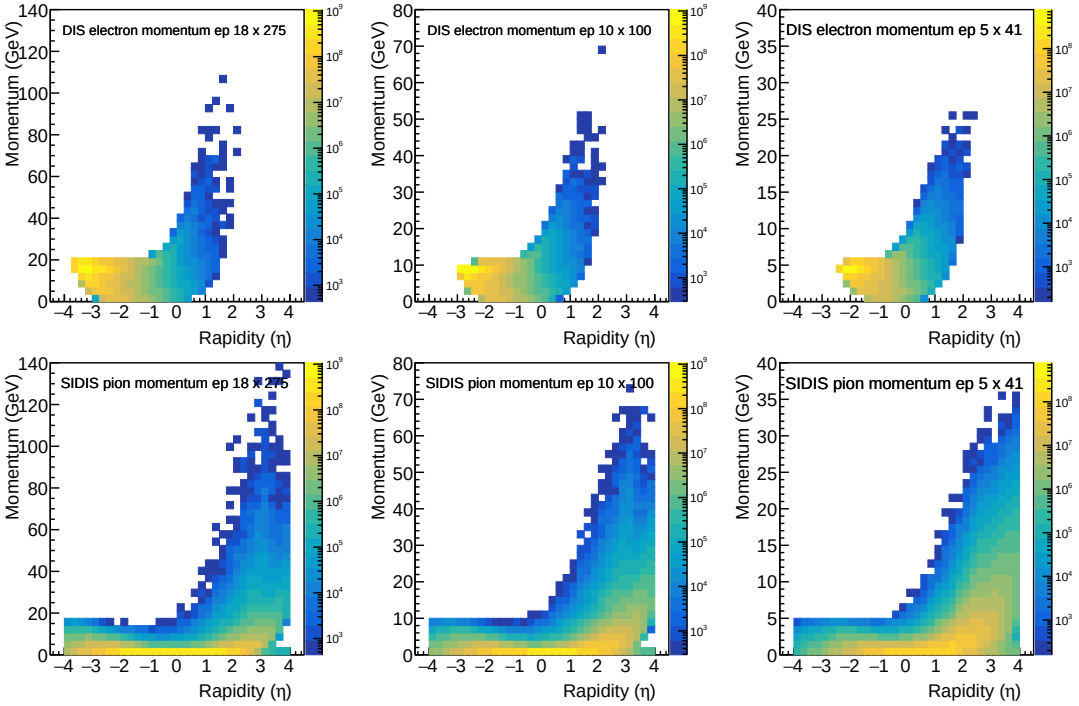

Figure 2.20: Top panel: Scattered DIS lepton momenta as a function of pseudorapidity from left to right for the highest energy collisions of 18 GeV electrons on 275 GeV protons, 10 GeV on 100 GeV and 5 GeV on 41 GeV. Bottom panel: SIDIS pion momenta as a function of pseudorapiity for the same three beam energy combinations. The following cuts have been applied: $0.01 < y < 0.9$, with inelasticity, y, momentum transfer $Q^2 > 1\,\text{GeV}$, and $W^2 > 10\,\text{GeV}^2$, as well as $0.05 < z < 0.95$ for the pions.

Figure 2.21 indicates the momentum/energy range of the scattered electron (black curve), photons (green), negative charged pions (blue) and kaons (cyan) as well as antiprotons (violet) and their sum (magenta) for a center-of-mass energy of 140 GeV (18 GeV on 275 GeV) as function of pseudo-rapidity. This plot provides on the one hand the needed information on the requirements for the scattered lepton identification as well as for identifying pions, kaons and protons. For the entire pseudo-rapidity ($-4 < \eta < 4$) negative pions, kaons and antiprotons show the same momentum distributions, with negative pions having a factor $\sim 3-5$ higher multiplicity as negative kaons and antiprotons. In the central detector region ($-1 < \eta < 1$) the momenta are of typically 0.1 GeV/c to 4 GeV/c with a maximum of about 10 GeV/c. Hadrons with higher momenta go typically in the forward (ion) direction for low lepton beam energies, and in the backward direction for higher lepton beam energies.

The hadrons need to be identified with a purity $> 95\%$ at preferably an efficiency of $> 90\%$ to measure identified hadron double spin asymmetries as small as 0.0001. Events with $Q^2 < 10\,\text{GeV}^2$ typically correspond to negative rapidities ($\eta < -2$) and $Q^2 > 10\,\text{GeV}^2$ correspond to rapidities $-2 < \eta < 1$. Depending on the center-of-mass energy the rapidity

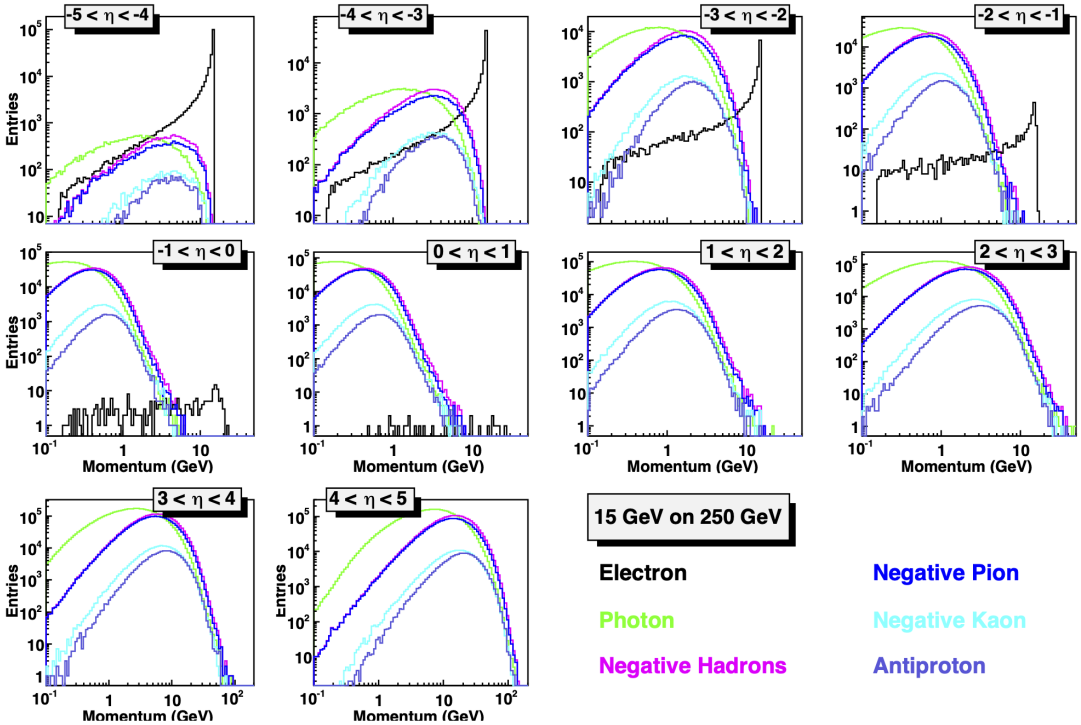

Figure 2.21: The momentum distribution for the scattered electrons (black), photons (greens), and negatively charged hadrons (magenta) for different pseudo-rapidity bins in the laboratory frame for beam energies of 18 GeV on 275 GeV. The distributions for negatively charged Pions (blue), Kaons (cyan) and antiprotons (violet) are shown as well. No kinematic cuts have been applied. (Figure need to be adjusted slightly)

distributions for hadrons (both charged and neutral) and the scattered lepton can overlap and need to be disentangled. For $\eta < -3$ electron, photon and charged hadron rates vary from being comparable to a factor of 10 different. For the higher pseudo-rapidities electron rates are a factor of 100-1000 smaller than photon and charged hadron rates, and comparable at a 10 GeV/c total momentum. For very high Q^2-events a suppression factor of > 100 is needed. This adds another requirement to the detector: **excellent electron identification**. It is noted that the kinematic region in pseudo-rapidity over which hadrons and also photons need to be suppressed, typically by a factor of 10 - 1000, shifts to more negative pseudo-rapidity with increasing center-of-mass energy. Measuring the ratio of the energy and momentum of the scattered lepton, typically gives a reduction factor of $\sim$100 for hadrons. This requires the availability of both tracking detectors (to determine momentum) and electromagnetic calorimetry (to determine energy) over the same rapidity coverage. By combining information from these two detectors, one also immediately suppresses the misidentification of photons in the lepton sample. Having good tracking detectors with similar rapidity-coverage as electromagnetic calorimetry similarly aids the y-resolution at low y from the lepton method. The hadron suppression is further improved by adding a Hadron Calorimeter and/or a Cerenkov detector to the electromag-

netic calorimetry and/or having tracking detectors to provide good dE/dx. *The resulting lepton purities should be* $> 99\%$ *with preferable a detection efficiency of* $> 90\%$.

Exclusive Processes

Exclusive DIS and especially exclusive diffractive processes require a careful design of the detector and the IR in the outgoing proton/nucleus beam direction. Contrary to exclusive electron-proton events, for electron-nucleus collisions it is not possible to tag the outgoing intact scattered nucleus. Therefore, another technique needs to be realized to ensure exclusivity. One can require a "rapidity gap" in the detector, meaning that there is a region in the detector from the hadron beam towards the center of the detector in which there is no activity from the hadronic final state. The efficiency for detecting exclusive events and their purity therefore depends strongly on the rapidity coverage (hermiticity) of the detector. Simulations have shown that a rapidity coverage of -2 to 4 is required to have detection efficiencies $> 90\%$ and a purities $> 90\%$ for exclusive e+A events assuming a cross section ratio of Exclusive-to-DIS events of 10:90 as measured at HERA.

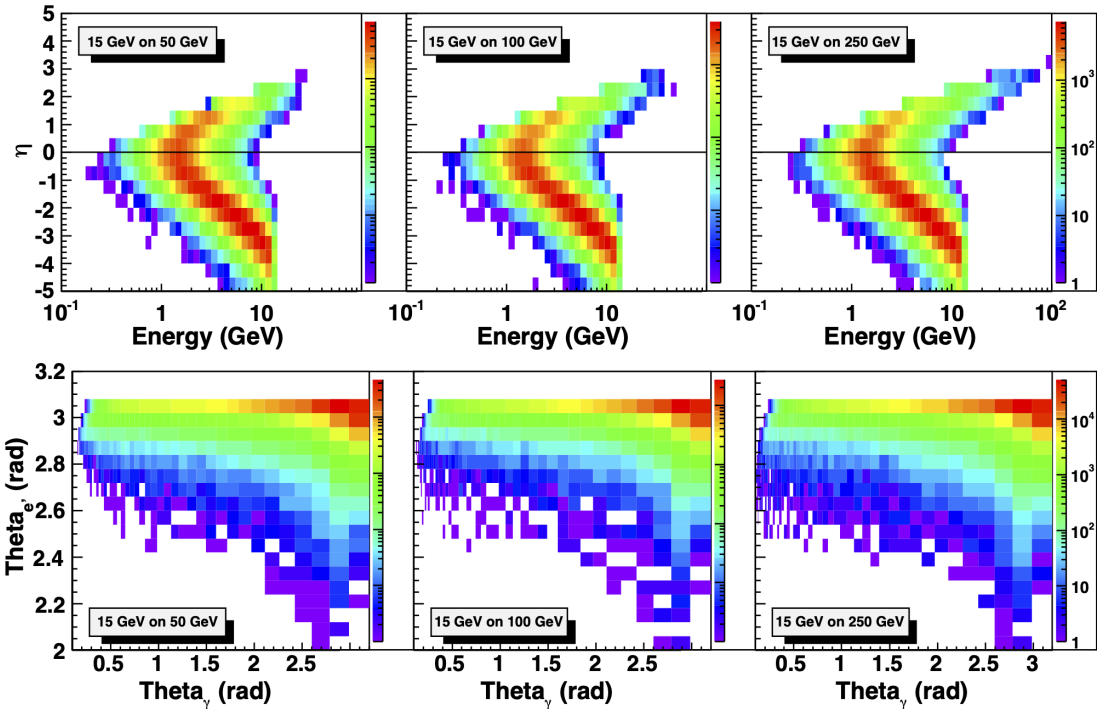

Figure 2.22: The energy vs. pseudo-rapidity in the laboratory frame for photons from DVCS (top) and the correlation between the scattering angle of the DVCS photon and the scattered lepton for three different center-of-mass energies. The following cuts have been applied: $Q^2 > 1\,\mathrm{GeV}^2$, $0.01 < y < 0.85$, and $-5 < \eta < 5$.

As a case example for an exclusive process, Figure 2.22 shows the energy vs. rapidity

distributions for photons from deeply virtual Compton scattering, and the correlation between the scattering angle of the DVCS photon and the scattered lepton in the laboratory frame for different beam energy combinations. The general patterns follow the ones in Figure 2.20, but even at the low lepton beam energies the DVCS photons go more into the backward direction. To separate the DVCS events from their dominant background from Bethe-Heitler events it is important to measure the DVCS photon energy and the lepton momentum down to 1 GeV and to be able to resolve their scattering angle difference $(\theta_e - \theta_\gamma)$ down to below 1^o. The most challenging constraints on the detector design for exclusive reactions compared to semi-inclusive reactions are, however, not given by the final state particle, but to ensure the exclusivity of the event. Exclusivity can be achieved by different methods. In electron-proton scattering by detecting all reactions products, especially the scattered protons going forward under extremely small scattering angles or requiring a rapidity gap between the hadron beam and produced pseudo-scalar/vector mesons and jets. To make the rapidity gap method highly efficient a detector with an acceptance to high pseudo-rapidities is needed. In lepton-nucleus scattering exclusivity can be ensure by the rapidity gap method or by vetoing the nuclear breakup by requiring no decay neutrons in the zero-degree calorimeter. *Therefore no collider equipment can be installed inside the main detector volume and/or extend beyond* 1.5° *in order to not compromise the efficiency and purity of exclusive events that are detected through the rapidity-gap method.*

Detector Requirements

We conclude this section with a brief summary of the key detector requirements that are imposed by the rich physics program of an EIC.

- The EIC requires a *h*ermetic detector with *l*ow mass inner tracking.
- The main detector needs to cover the range of $-4 < \eta < 4$ for the measurement of electrons, photons, hadrons, and jets. It will need to be augmented by auxiliary detectors like low-Q^2 tagger in the far backward region and proton (Roman Pots) and neutron (ZDC) detection in the far forward region.
- The components of an EIC detector will have moderate occupancy as the event multiplicities are low. However, depending on the machine background level certain components close to the beamline might see higher occupancies. For details see Sec. 8.3.2.
- An EIC detector will have to cope with a data rate of up to $\sim$ 500 kHz at full luminosity.
- Compared to LHC detectors, the various subsystems of an EIC detector have moderate radiation hardness requirements.
- Excellent momentum resolution in the central detector ($\sigma_{p_T}/p_T(\%) = 0.05 p_T \oplus 0.5$).
- Good momentum resolution in the backward region with low multiple-scattering terms ($\sigma_{p_T}/p_T(\%) \approx 0.1 p_T \oplus 0.5$).

- Good momentum resolution at forward rapidities ($\sigma_{p_T}/p_T(\%) \approx 0.1 p_T \oplus 1-2$).
- Good impact parameter resolution for heavy flavor measurements ($\sigma \approx 5 \oplus 15/p \sin^{3/2}\theta$ (μm)).
- Good electromagnetic calorimeter resolution in the central detector ($\sigma(E)/E \approx 10\%/\sqrt{E}$).
- Excellent electromagnetic calorimeter resolution at forward rapidities ($\sigma(E)/E < 2\%/\sqrt{E}$).
- Good hadronic resolution in forward region ($\sigma(E)/E \approx 50\%/\sqrt{E}$).
- Excellent PID for 3 σ $\pi/K/p$ separation up to 45 GeV/c in forward region, up to 8 GeV/c in the central detector. and up to 7 GeV/c in the backward region.

2.5.2 Scientific Requirements for the Interaction Regions

To cover the physics program, as described in earlier sections, it is extremely important to integrate the detector into the interaction region *already during the early design stages* of the collider. In the following, the requirements will be discussed, categorized according to the processes described in Table 2.1.

Exclusive Processes

The detection of forward-going scattered protons from exclusive reactions, as well as of decay neutrons from the breakup of heavy ions in incoherent and non-diffractive reactions, is particularly challenging.

Electron-Proton Scattering: In general, for exclusive reactions, one wishes to map the four-momentum transfer, or Mandelstam variable $t = |p_{\text{in}} - p_{\text{out}}|^2$ of the hadronic system, and then obtain an image of the spatial partonic structure of the proton by a Fourier transform of the (un)polarized cross section as function of t Figure 2.23 shows what fraction of the beam momentum ($x_L = p'_L/p_{\text{Beam}}$) is carried by these scattered protons as measured by ZEUS at HERA [37] and the correlation between the proton scattering angle and its momentum. This illustrates that the remaining baryonic states go in the very forward proton-beam direction. Even at a proton energy of 50 GeV, the proton scattering angles only range to about 25 mrad. At proton energies of 250 GeV, this number is further reduced by a factor of five. In all cases, the scattering angles are small. As discussed earlier (see section 2.5.1), the main detector reaches down to a rapidity -4 to 4, corresponding to 35 mrad from the beam line. Therefore, these protons are not seen in the main detector and need a different technique to be detected, i.e. Roman Pots. Their acceptance strongly depends on the exact interaction region design.

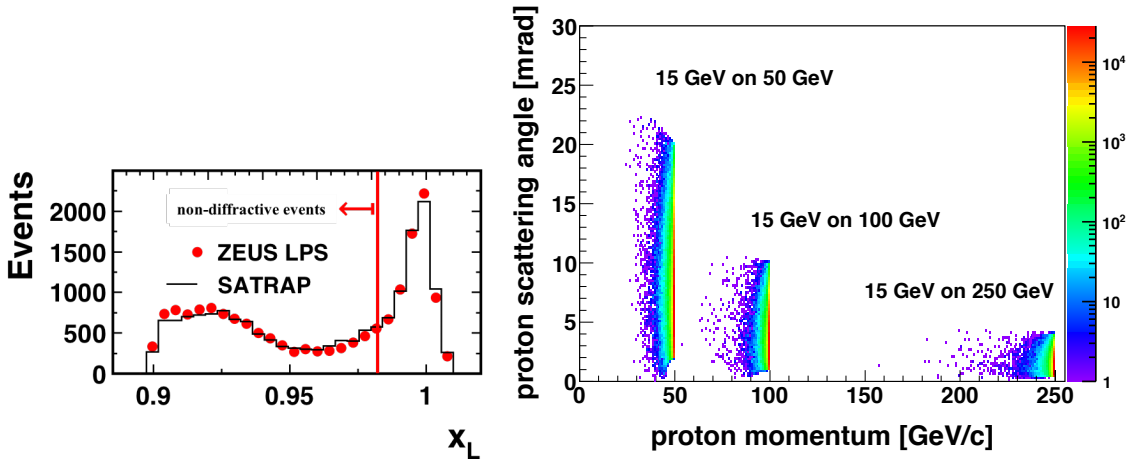

Figure 2.23: Left: Fraction of the beam momentum carried by the scattered protons as measured by ZEUS at HERA. Right: The scattered proton momentum vs. scattering angle in the laboratory frame for DVCS events with different beam energy combinations. The following cuts have been applied: $1\,\mathrm{GeV}^2 < Q^2 < 100\,\mathrm{GeV}^2, 0.01 < y < 0.85, 10 - 5 < x < 0.5$ and $0.01\,\mathrm{GeV}^2 < t < 1\,\mathrm{GeV}^2$. The angle of the recoiling hadronic system is directly and inversely correlated with the proton energy. It thus decreases with increasing proton energy.

Figure 2.24 (top) shows the cross section of exclusive real photon production (DVCS: $ep \longrightarrow e'p'\gamma$) as function of t. The red dots represent the measurements and their statistical precision as obtained at EIC for $\sqrt{s} = 141\,\mathrm{GeV}$ and an integrated luminosity of $10\,\mathrm{fb}^{-1}$ for $0.03\,\mathrm{GeV}^2 < |t| < 1.6\,\mathrm{GeV}^2$ corresponding to an acceptance in p_T of $0.18\,\mathrm{GeV/c} < p_T < 1.3\,\mathrm{GeV/c}$, which is the nominal requirement from the EIC White Paper. The blue curves represent an exponential fit to the measured points for different regions in t with the width of the band representing the uncertainty of the fit. The different rows show the result for different acceptances in p_T of the scattered protons. The lower row shows the impact parameter dependent PDF obtained from a Fourier transform of the cross section measurement with different p_T acceptances. The bands represent the parametric errors in the fit and the uncertainty from different extrapolations to the regions of unmeasured (very low and very high) p_T of the scattered protons. *Based on these studies and the EIC White Paper, protons with* $0.18\,\mathrm{GeV/c} < p_T < 1.3\,\mathrm{GeV/c}$ *need to be transported through the IR such that they can be detected as soon as they are separated from the core of the beam.*

To obtain a full picture of the (un)polarized spatial partonic imaging of the proton it is critical to have measurements of the (un)polarized diffractive cross sections of reactions with a charge exchange, like $e + p \rightarrow e' + n$. In this case the four-momentum transfer t is obtained from the forward scattered neutrons. Figure 2.25 shows the correlation of the scattering angle of the neutrons as function of t for two different beam energy combinations. Like for the protons, the neutrons are scattered at very small angles with respect to the outgoing proton beam. *These neutrons with an angular distribution from 9 mrad (at* $\sqrt{s} = 141\,\mathrm{GeV}$*) to 26 mrad (at* $\sqrt{s} = 32\,\mathrm{GeV}$*) from the hadron beam axis need to be transported through the IR to a zero-degree calorimeter.*

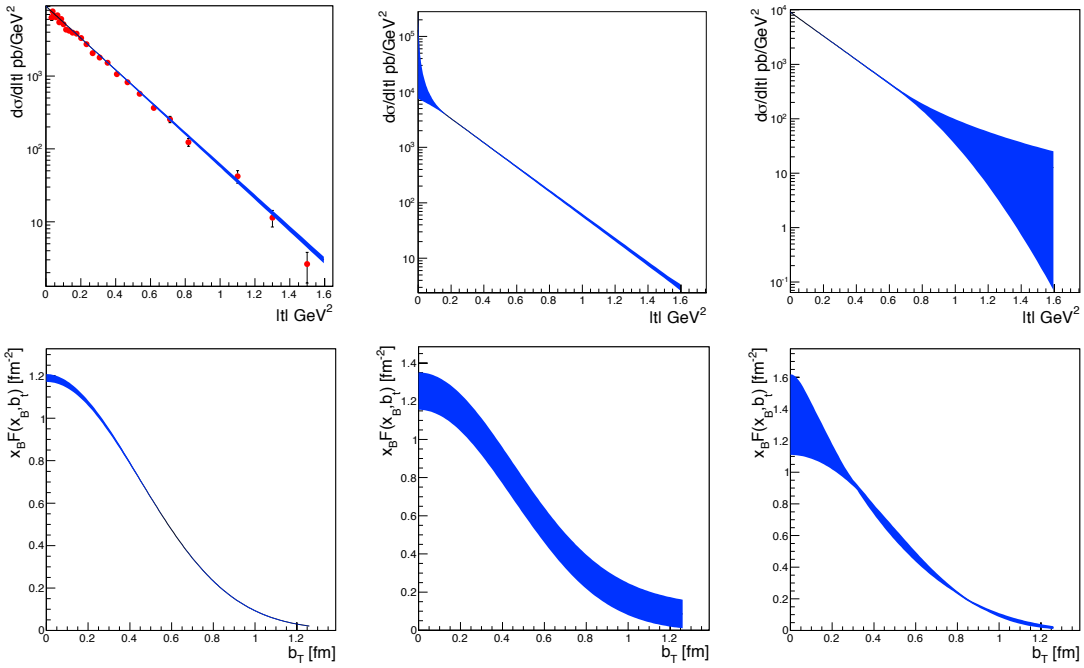

Figure 2.24: Top: The cross section as function of t. The red dots represent the measurements and their statistical precision as obtained at EIC for $\sqrt{s} = 141\,\text{GeV}$ and an integrated luminosity of $10\,\text{fb}^{-1}$. The blue curves represent an exponential fit to the measured points for different regions in t with the width of the band representing the uncertainty of the fit. The different rows show the result for different acceptances in p_T of the scattered protons. Bottom: The impact parameter dependent PDF obtained from a Fourier transform of the measured cross section with different p_T acceptances. The bands represent the parametric errors in the fit and the uncertainty from different extrapolations to the regions of unmeasured (very low and very high) p_T of the scattered protons. Left: $0.18\,\text{GeV/c} < p_T < 1.3\,\text{GeV/c}$, $0.03\,\text{GeV}^2 < |t| < 1.6\,\text{GeV}^2$; Middle: $0.44\,\text{GeV/c} < p_T < 1.3\,\text{GeV/c}$; Right: $0.18\,\text{GeV/c} < p_T < 0.8\,\text{GeV/c}$.

Electron-Nucleus Scattering: The only possible way to tag coherent diffractive exclusive electron-nucleus events for heavy nuclei is to veto nuclear breakup. For coherent diffractive events the intact nucleus is scattered under very small forward angles in the outgoing beam direction and mainly remains inside the beam envelope. Tagging exclusive events can be realized by requiring no neutrons and photons from the nuclear breakup in a zero-degree calorimeter. Figure 2.26 shows the breakup neutron momentum vs. scattering angle in the laboratory frame for different beam energies. *To achieve a very high tagging efficiency of* $\sim$ 100% *for coherent diffractive electron-nuclei scattering events one needs to transport neutrons and photons within a cone of four mrad to six mrad, depending on the beam energy, through the IR to a zero-degree calorimeter.*

For all the different processes, collision geometries in e+A (see Figure 2.27) can be determined by utilizing the ZDC. The number of forward neutrons produced and detected in the ZDC is expected to be sensitive to the path length d of the parton and fragmentation

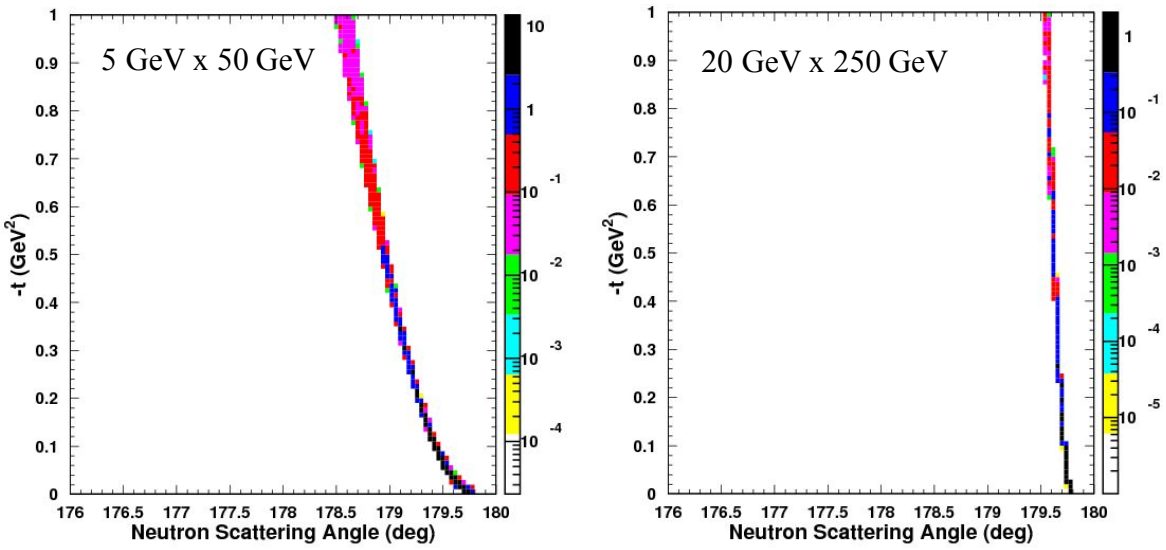

Figure 2.25: The neutron scattering angle as function of t in the laboratory frame for two different beam energy combinations. Note a scattering angle of 180° corresponds to the outgoing proton beam direction in this plot.

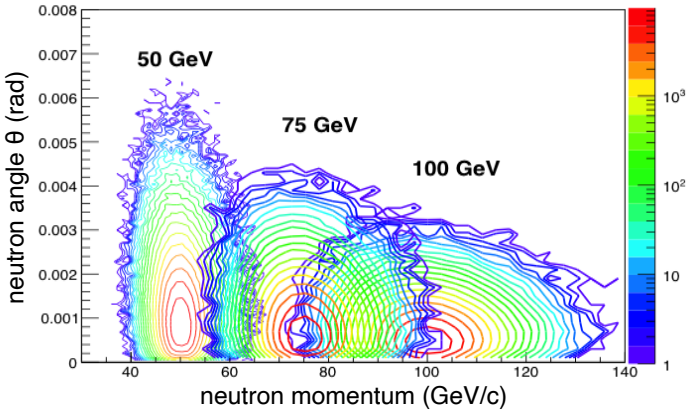

Figure 2.26: The scattered neutron momentum vs. scattering angle in the laboratory frame for different beam energies.

of the colliding nucleon along the virtual photon direction in the nucleus. See Figure 2.27 for the correlation between the number of forward scattered neutrons and the path length. The geometric information is an additional and useful gauge for investigating properties of partonic interactions in nuclei. While the impact parameter b has a correlation with the number of neutrons in the ZDC, the most "central" collision in e+A ($b \sim 0$) can be identified from events with the highest neutron multiplicity since the longest path length of the nucleon fragmentation in the nucleus is expected to be at $b = 0$. This will be an effective tool for selecting events with maximized nuclear effects in SIDIS e+A collisions, like e.g.,

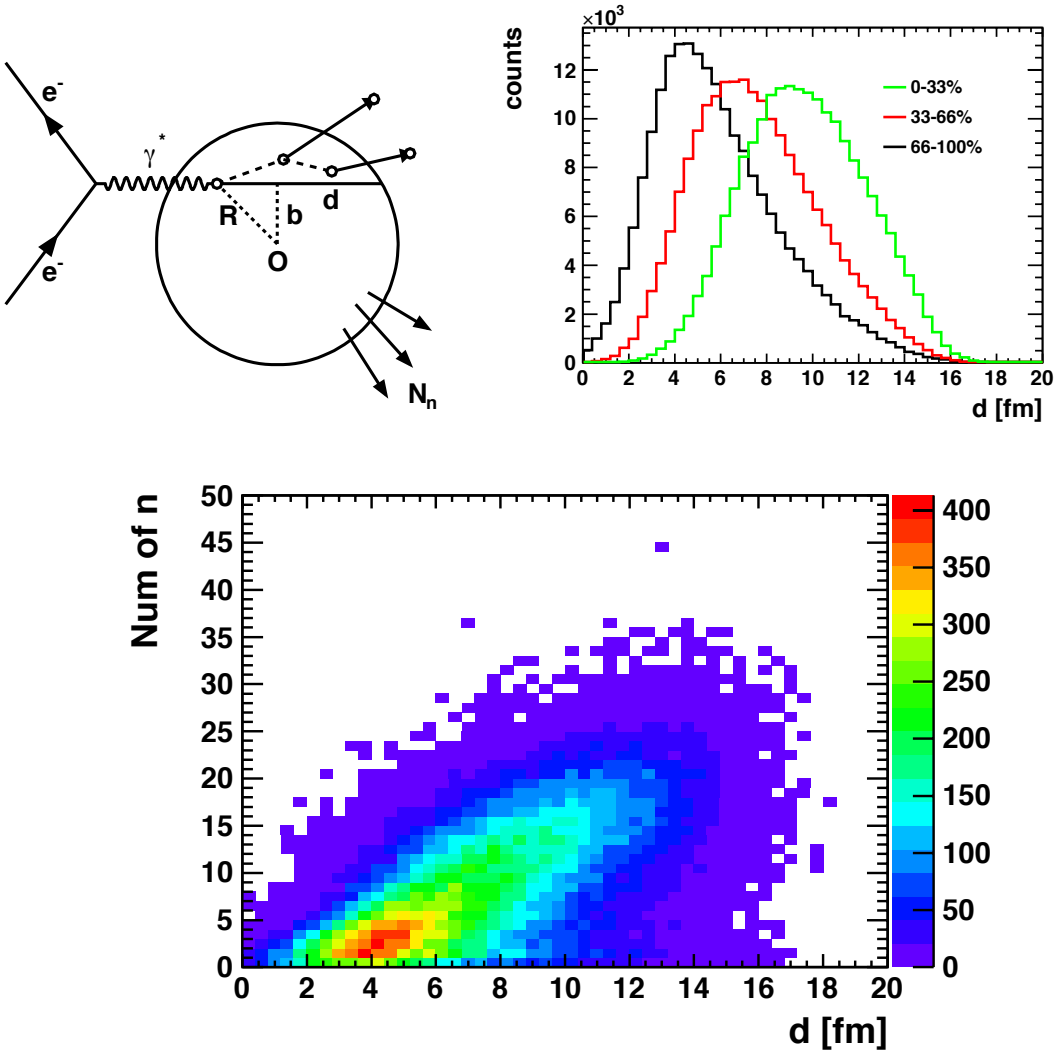

Figure 2.27: Top-left: Collision geometry of e+A, showing the path length d of the parton and fragmentation of the struck nucleon along the virtual photon direction. The impact parameter b is defined as the transverse distance between the center of the nucleon and the virtual photon. Top-right: Distribution of the path length as selected by the neutron multiplicity. The estimate done using DPMJet-III [38]. Bottom: Correlation between number of produced forward neutrons vs. path length of parton and fragmentation of the struck nucleon in the nucleus. All the forward neutrons can be detected in the ZDC.

dihadron correlation studies [27, 39].

Recent physics studies showed that selecting on the number of neutrons to reach a centrality of $> 5\%$ enhances the effective A in the reaction, which is crucial for any measurements of non-linear effects in QCD. This, and the requirement that the four-momentum transfer t in diffractive reactions with a charge exchange is obtained from the neutron, requires a ZDC with higher energy resolution ($\approx 30\%/\sqrt{E}$) than is currently achieved at RHIC

($65\%/\sqrt{E} + 15\%$ for a ZDC size of 10 cm $\times$ 10 cm $\times$ 60 cm). This requires more space in x-y to integrate a ZDC in order to minimize shower leakages in the transverse direction at 30 m from the IR. The required space will depend on the exact detector technology chosen; for examples see [40, 41]. The longitudinal size required would be around one meter.

Inclusive Processes

There are many physics topics beyond what was discussed in the EIC White Paper [3] that benefit from tagging the scattered electron at Q^2 values significantly below 1 GeV^2. An example is the determination of the (un)polarized partonic structure of photons [31].

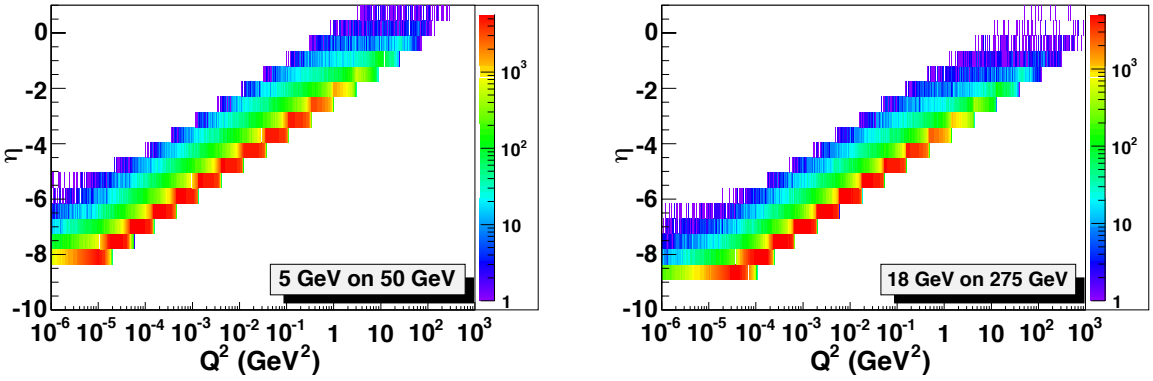

Figure 2.28: Relation between Q^2 of the scattered electron rapidity for 5 GeV and 18 GeV electron beam energy.

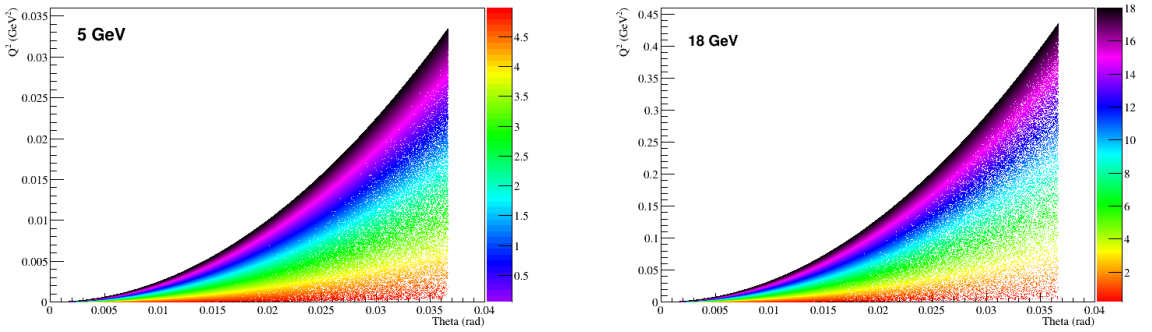

Figure 2.29: The relation between the electron scattering angle and Q^2 for 5 GeV and 18 GeV electron beam energy. The colors indicate the energy of the scattered electron.

Scattered electrons with a $Q^2 < 0.5\,\text{GeV}^2$ cannot be detected in the main detector. Therefore, as was the case in all in HERA detectors, a special low-Q^2 tagger is needed. The scattered electrons will be detected in an electromagnetic calorimeter with several Si-tracking planes in front. Such a device needs to be well-integrated into the IR design and care needs to be taken to separate the scattered electrons from electrons from the bremsstrahlung process, which, due to their high cross-section and the high EIC luminosity will be dominant.

Figures 2.28 and 2.29 show several kinematic relations for the scattered electron, i.e. Q^2 vs. rapidity, Q^2 as function of the electron scattering angle, and its energy.

Electron-Nucleus Scattering

The physics program of an EIC requires electron-(un)polarized proton and neutron collisions to allow full flavor separation of (un)polarized parton distribution functions. As polarized neutron beams are not feasible, (un)polarized ^{3}He and deuterium beams constitute effective proxy for a neutron beam. To ensure that the scattering really occurred on the neutron, the spectator proton(s) need to be detected. Figure 2.30 shows the correlation of momentum and scattering angle for the spectator protons from electron-deuteron and electron-^{3}He scattering for two different values of $\sqrt{s}$. The detection of these spectator protons is challenging as they have small scattering angles and a different rigidity compared to the hadron beam, which leads to stronger bending in the magnets. The (un)polarized ^{3}He and deuterium beams do not only constitute effective neutron beams, but also provide the possibility to study how the proton structure is modified if bound in a nucleus. For this purpose, the spectator neutron needs to be tagged. These neutrons have the same distribution in scattering angle and momentum as the protons. Therefore, a ZDC with its

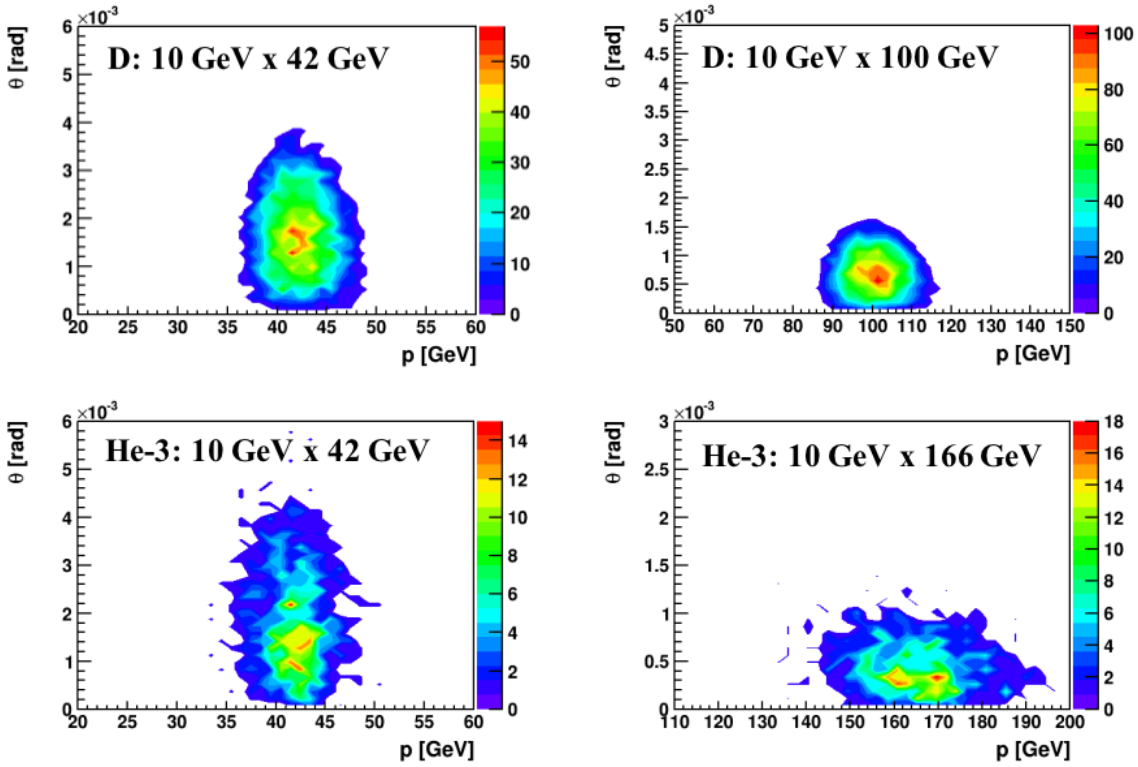

Figure 2.30: The correlation of momentum and scattering angle for the spectator proton in electron-deuteron and electron-^{3}He-scattering for two different values of $\sqrt{s}$.

acceptance optimized for break-up neutrons as described above (see Figure 2.26) will also have a high acceptance for these spectator neutrons.

Auxiliary Detectors

To utilize the full statistical power made possible by the high luminosity of 10^{33} to $10^{34}\,\mathrm{cm}^{-2}\mathrm{s}^{-1}$, it is indispensable to have high precision measurements of the electron and hadron beam polarizations and the luminosity. Doubly polarized electron-hadron colliders are the best way to unravel the internal structure of the nucleons and are the only tool, which will allow us to finally unravel how the spin of the proton is built by its quarks and gluons. Figure 7 in Ref. [11] shows, that for a high precision determination of the gluon contribution to the spin of the proton, the overall systematic uncertainty should be around two percent. An increase of the overall systematic uncertainty of five percent leads to a 30% increase in the uncertainty of the contribution of the gluons to the spin of the protons.

Luminosity The bremsstrahlung process $e + p \longrightarrow e + p + \gamma$ was used successfully for the measurement of luminosity by the HERA collider experiments [42–44]. It has the features of a precisely known large QED cross-section resulting in negligible statistical uncertainty. In contrast to HERA, where only the electron beam was polarized, both the electron and proton/light ion beams will be polarized in EIC. In this case the bremsstrahlung rate is sensitive to the polarization dependent term a in the cross section $\sigma_{\mathrm{brems}} = \sigma_0(1 + aP_eP_h)$. Thus, the polarization (P_e, P_h) and luminosity measurements are coupled, and the precision of the luminosity measurement is limited by the precision of the polarization measurement. This also limits the precision of the measurement of double spin asymmetries $A_{LL} = 1/(P_eP_h)(N^{++/--} - RN^{+-/-+})/(N^{++/--} + RN^{+-/-+})$ through the determination of the relative luminosity $R = L^{++/--}/L^{+-/-+}$. The precision needed for the relative luminosity measurement is driven by the magnitude of A_{LL} at low-x and Q^2, which is typically on the order of 10^{-4}. At RHIC levels of 2 to 4×10^{-4} have been achieved. A factor of 2 to 5 improvement is required for the EIC. As discussed earlier, due to the high luminosity it is critical to minimize the systematic uncertainties; the requirement for the systematic uncertainty is $\delta L/L < 1\%$. The straightforward method for measuring bremsstrahlung is to use a calorimeter at zero degrees in the electron direction counting the resulting photons, the distribution of which is strongly peaked in the forward direction. The calorimeter is also exposed to the direct synchrotron radiation fan and must be shielded, thus degrading the energy resolution. At peak HERA luminosities, the photon calorimeters were hit by 1-2 photons per HERA bunch crossing. At an EIC luminosity of $10^{33}\,\mathrm{cm}^{-2}\,\mathrm{s}^{-1}$, the mean number of photons per bunch crossing is over 20 for electron-proton scattering and increases with Z^2 of the target for nuclear beams. The distributions are broad, with a mean proportional to the number of photons per bunch crossing. The counting of bremsstrahlung photons thus is effectively an energy measurement in the photon calorimeter with all of the related systematic uncertainties (e.g. gain stability) of such a measurement. An alternative method to counting bremsstrahlung photons, used effectively by the ZEUS collaboration at HERA, employs a pair spectrometer. A small fraction of photons is converted into e^+e^-

pairs in the vacuum chamber exit window. A dipole magnet splits the pairs and each particle hits a separate calorimeter adjacent to the unconverted photon direction. Further details about the luminosity monitor can be found in section 8.4.4.

Lepton and Hadron Polarimetry

Lepton Polarization: Compton back-scattering is the established method to measure electron beam polarization in *e+p* colliders. At HERA, there were two Compton back-scattering polarimeters [45], one measuring the transverse polarization (TPOL) of the beam through a position asymmetry, and another one measuring the longitudinal polarization (LPOL) of the beam through an energy asymmetry in Compton back-scattered photons. The TPOL and LPOL systematic uncertainties of HERA RUN-I were 3.5% and 1.6% and Run-II 1.9% and 2.0%, respectively. To balance the expected high luminosity at the EIC, these systematic uncertainties should be reduced to $\sim$ 1%. More details on EIC electron polarimetry can be found in Section 8.6.1.

Hadron Polarization: Measuring the hadron beam polarization is significantly more involved. Contrary to the electron case, there is no process that can be calculated from first principles. Therefore, a two-tier measurement is needed: one providing the absolute polarization, which normally has low statistical power, and a high statistical power measurement that measures the relative polarization. At RHIC [46], the single spin asymmetry A_N of the elastically scattered polarized proton beam on a polarized hydrogen jet is used to determine the absolute polarization. This measurement provides the average polarization per fill and for each proton beam with a statistical uncertainty on the order of $\approx$ 5% and a systematic uncertainty of 3.2%. High-statistics bunch-by-bunch relative polarization measurements are provided by measuring the single spin asymmetry A_N for scattering the polarized proton beam off a carbon fiber target. To obtain absolute measurements, the pC-measurements are cross-normalized to the absolute polarization measurements from the hydrogen-jet polarimeter. The pC-measurements provide the polarization lifetime and the polarization profile per fill with high statistical precision. The achieved total systematic uncertainty for single spin asymmetries until 2015 is 3.4%.

The same concept is currently planned for all polarized hadron beams in the EIC, namely proton, deuterium, and ^{3}He [47]. It is foreseen to continue to have the absolute and relative hadron polarimeters located at IP12 in EIC; therefore, no constraints need to be considered for the IR.

However, there is the requirement for a local polarimeter between the spin rotators to monitor the degree of spin rotation from transverse in the arcs to longitudinal at the experiments. This can be done by integrating a fast, high precision proton-carbon (pC) polarimeter into the extended IR. This pC polarimeter is based on very small angle polarized proton-carbon elastic scattering in the Coulomb-Nuclear Interference region. The analyzing power is maximum for transverse or radial hadron beam polarization and goes to zero for longitudinal polarized hadron beams. The requirements on the extended IR region

are purely spatial ($\sim$ 0.5 to 0.8 m) to integrate the scattering chamber for the carbon target intercepting the beam and the Si-detectors to measure the elastically scattered carbons. More details on the EIC absolute and relative hadron beam polarimetry can be found in Section 8.6.2.

Summary of Requirements for the Interaction Regions

Table 2.2 summarizes the requirements for the overall interaction region design derived from the EIC physics discussed in the 2010 INT Report [2], the EIC White Paper [3], and the document assessing the energy dependence of key measurements [5].

Table 2.2: Summary of the requirements from the physics program on the overall IR design.

	Hadron	Lepton
Machine element free region	$\pm$4.5 m main detector beam elements $< 1.5^\circ$ in main detector volume	
Beam Pipe	Low mass material, i.e. Beryllium	
Integration of detectors	Local Polarimeter	
Zero Degree Calorimeter	60 cm $\times$ 60 cm $\times$ 2 m @$s = 30$ m	
scattered proton/neutron acc. all energies for e+p	Proton: 0.18 GeV/c $< p_T <$ 1.3 GeV/c $0.5 < x_L < 1 (x_L = E'_p/E_{Beam})$ Neutron: $p_T <$ 1.3 GeV/c	
scattered proton/neutron acc. all energies for e+A	Proton and Neutron: $\theta < 6$ mrad (for $\sqrt{s} = 50$ GeV) $\theta < 4$ mrad (for $\sqrt{s} = 100$ GeV)	
Luminosity	Relative Luminosity: $R = L^{++/--}/L^{+-/-+} < 10^{-4}$	
		γ acceptance: $\pm$1 mrad $\rightarrow \delta L/L < 1\%$
Low Q^2-Tagger		Acceptance: $Q^2 < 0.1$ GeV

Chapter 8

The EIC Experimental Equipment

8.1 Realization of the Experimental Equipment in the National and International Context

The path chosen for the consideration of the Experimental Equipment scope of the Electron-Ion Collider differs much from the Accelerator scope. Development of the EIC science and the experimental equipment required to successfully implement the science as documented in the NSAC and NAS reports has been driven by an international EIC community. This community formalized itself in 2016 in the EIC User Group (EICUG, see www.eicug.org). The EICUG has in 2020 grown to over 1100 members representing 235 institutions and 32 countries (see www.eigug.org/pnb).

A handful of general-purpose EIC detectors have been conceptualized. To bring the state of the EIC experimental equipment definition to a next level, and folding in that the EIC is capable of supporting a science program that includes two detectors, the EICUG put into effect a "Yellow Report" activity [1] Much documentation on the ongoing Yellow Report activity are given at http://www.eicug.org/web/content/yellow-report-initiative. The main goal of the Yellow Report activity is to advance the state of documented (i) physics studies (White Paper, INT program proceedings) and (ii) detector concepts (Detector and R&D Handbook) in preparation for the EIC. This will provide both the basis for further development of concepts for experimental equipment best suited to the EIC science needs, including complementarity of the two detector/interaction regions, and input towards future Technical Design Reports of the experimental equipment.

The general community strategy for this Yellow Report activity is both to *Quantify physics measurements for existing or new physics topics and implications for detector design*,

[1] The CERN Yellow Reports series provides a medium for communicating CERN-related work where publication in a journal is not appropriate. Reports include material having a large impact on the future of CERN, as well as reports on new activities which do not yet have a natural platform. The series includes reports on detectors and technical papers, criteria being that the audience should be large and the duration of interest long. The term Yellow Reports is now used frequently for documents with similar purpose in various physics communities unrelated to CERN.

and alternately to *Study detector concepts based on the requirements defined above, and quantify implications for the physics measurements.* The Yellow Report will be completed by January 2021, and will present the EIC community consensus on vision towards the general-purpose EIC experimental equipment, and also discuss detector technologies of relevance for two complementary general-purpose detectors. As such, with this community effort ongoing, and with the realization that the detector technologies for the general EIC science program are in general well understood, this section of the CDR describes a "plausible scenario reference EIC detector". This reference detector can execute the EIC science program as documented in the NSAC and NAS reports, but we include also mention of various alternate detector technologies under consideration for one, or even two, of the possible detectors.

We foresee a call for detector proposals to start after the Yellow Report completion. This folds in the result of a "Call for Expressions of Interest (EOI)" (see https://www.bnl.gov/eic/EOI.php). With this call, Brookhaven National Laboratory in association with TJNAF, invites interested groups to submit a (non-binding) Expression of Interest for their potential cooperation on the experimental equipment in support of a broad and successful science program at the EIC. The call also encouraged interested groups to work together within their country, their geographical region, or as a general consortium, to submit such EOIs. Input of these EOIs will give guidance on the detector scope and also be very influential in determining the trajectory of one or both general-purpose detectors (and their Interaction Regions). We plan to complete the process for selection of EIC detector proposals by the end of 2021, as stepping stone towards the formation of the detector collaboration(s).

In parallel with a nearly two-decade-long community effort of EIC science development and refinement, and experimental equipment conceptualization, Brookhaven National Laboratory in association with TJNAF and the DOE Office of Nuclear Physics established in 2011 a highly successful and still ongoing generic EIC-related detector R&D program (see wiki.bnl.gov/conferences/index.php/EIC_R%25D). This generic R&D program both built bridges between various domestic and international research groups and scientific communities, and was successful in its own right towards detector R&D. Presently, 281 scientists are engaged in the generic EIC-related R&D program, from 75 institutions in 10 countries. Most of the efforts have been organizationally merged in groups of scientists or consortia, which can provide the seeds for the long-term EIC detector collaboration(s).

In general, much due to the longstanding generic EIC-related detector R&D program, the detector technologies to implement a successful comprehensive Day-One EIC Science program exist. This is the reason that at CD-1 the detector presented in the remainder of the Section will be a plausible scenario reference detector, whereas the EIC User Group continues to consider various technologies for many of the different detector functions to implement, with an eye also to possible detector complementarity for a second detector. Indeed, thanks to the ongoing generic EIC-related detector R&D program, the needs for EIC Project-related detector R&D to address risk also are relatively modest. On the other hand, needs for a generic EIC-related detector R&D program do remain. These are driven both by pursuing alternative detector technologies for a complementary second fully inte-

grated EIC detector and Interaction Region, and to prepare for future cost-effective detector upgrades to enhance capabilities addressing new nuclear physics opportunities. Furthermore, the EIC science program is expected to span at least two decades, and will in this period likely also require further detector upgrades driven by its science findings.

Thus, we plan a continuation of the successful ongoing EIC-related detector R&D program, but managed in coordination with OPC-supported Project Detector R&D to underscore the strong connection to EIC detectors. We intend to use the EIC Detector Advisory Committee to provide advice on questions such as: (i) Are the EIC detector technology choices optimal and feasible on the EIC project time scale? (ii) Does the EIC Project-related detector R&D properly address the risk? (iii) Are there opportunities for generic EIC detector R&D to enhance the day-one and the longer-term EIC science program? and (iv) Is the design of the detector(s) sufficiently sound?

8.2 Experimental Equipment Requirements Summary

The physics program of an EIC imposes several challenges on the design of a general purpose detector, and more globally the extended interaction region, as it spans center-of-mass energies from 29 GeV to 141 GeV, different combinations of both beam energy and particle species, and several distinct physics processes. The various physics processes encompass inclusive measurements $e + p/A \rightarrow e' + X$; semi-inclusive processes $e + p/A \rightarrow e' + h + X$, which require detection of at least one hadron in coincidence with the scattered lepton; and exclusive processes $e + p/A \rightarrow e' + N'A' + \gamma/h$, which require the detection of all particles in the reaction with high precision. Section 2.3 and 2.5 discuss in detail how the requirements on the accelerator, the interaction region and the experimental equipment flow down from the EIC science.

The high level requirements for the EIC general purpose detector are:

- The EIC requires a *h*ermetic detector with *l*ow mass inner tracking.
- The main detector needs to cover the range of $-4 < \eta < 4$ for the measurement of electrons, photons, hadrons, and jets. It will need to be augmented by auxiliary detectors like low-Q^2 tagger in the far backward region and proton (Roman Pots) and neutron (ZDC) detection in the far forward region.
- The components of an EIC detector will have moderate occupancy as the event multiplicities are low. However, depending on the machine background level certain components close to the beamline might see higher occupancies. For details see Sec. 8.3.2.
- An EIC detector will have to cope with a data rate of up to $\sim$ 500 kHz at full luminosity.
- Compared to LHC detectors, the various subsystems of an EIC detector have moderate radiation hardness requirements.

The intensive work done in the EIC user group "Yellow Report" activity has resulted in detailed requirements for the different subdetectors forming the central detector and the individual detectors along the beamline. The current status of these requirements is shown in Table 8.2.

The EIC experimental equipment does not stop at the general purpose detector to realize the full science program the design of the IR and the integration of the far forward detectors both along the outgoing lepton and hadron beam are equally critical. The detector performance requirements for these detectors are documented in Table 8.2. The design requirements for the IR are summarized in Table 8.1. Also these requirements are further refined during the continuing "Yellow Report" process. How well the current interaction region design fulfills the requirements is documented in detail in section **??**.

Table 8.1: Summary of the requirements from the physics program on the overall IR design.

	Hadron	Lepton
Machine element free region	± 4.5 m main detector beam elements $< 1.5^\circ$ in main detector volume	
Beam Pipe	Low mass material, i.e. Beryllium	
Integration of detectors	Local Polarimeter	
Zero Degree Calorimeter	$60\,\text{cm} \times 60\,\text{cm} \times 2\,\text{m}$ @$s = 30\,\text{m}$	
scattered proton/neutron acc. all energies for e+p	Proton: $0.18\,\text{GeV/c} < p_T < 1.3\,\text{GeV/c}$ $0.5 < x_L < 1 (x_L = E'_p/E_{Beam})$ Neutron: $p_T < 1.3\,\text{GeV/c}$	
scattered proton/neutron acc. all energies for e+A	Proton and Neutron: $\theta < 6\,\text{mrad}$ (for $\sqrt{s} = 50\,\text{GeV}$) $\theta < 4\,\text{mrad}$ (for $\sqrt{s} = 100\,\text{GeV}$)	
Luminosity	Relative Luminosity: $R = L^{++/--}/L^{+-/-+} < 10^{-4}$	
		γ acceptance: $\pm 1\,\text{mrad}$ $\rightarrow \delta L/L < 1\%$
Low Q^2-Tagger		Acceptance: $Q^2 < 0.1\,\text{GeV}$

Table 8.2: This matrix summarizes the high level requirements for the detector performance. The interactive version of this matrix can be obtained through the Yellow Report Physics Working Group WIKI page (https://wiki.bnl.gov/eicug/index.php/Yellow$_{R}eport_{p}hysics_{C}ommon$).

η	Nomenclature			Tracking				Electrons and Photons			π/K/p		HCAL		Muons
				Resolution	Allowed	minimum-pT	Si-Vertex	Resolution σ_E/E	PID	min E	p-Range	Separati	Resolution σ_E/E	Energy	
-6.9 to -5.8			low-Q2 tagger	σθ/θ < 1.5%; 10-6 < Q2 < 10-2 GeV2											
-5.0 to -4.5						300 MeV pions									
-4.5 to -4.0			Instrumentation to separate charged particles from photons			300 MeV pions		2%/√E(+1-3%)		50 MeV					
-4.0 to -3.5	↓ p/A	Auxiliary De								50 MeV			~50%/√E + 6%		
-3.5 to -3.0										50 MeV					
-3.0 to -2.5			Backward Detector	σpT/pT ~ 0.1%⊕0.5%			σ_xy ~ 30/pT μm +40 μm			50 MeV	≤ 7 GeV/c		~45%/√E+6%		muons useful for bkg, improve resolution
-2.5 to -2.0				σpT/pT			σ_xy ~ 30/pT μm +20 μm	2%/√E(+1-3%)		50 MeV					
-2.0 to -1.5				σpT/pT 0.05%⊕0.5%				7%/√E(+1-3%)		50 MeV					
-1.5 to -1.0										50 MeV					
-1.0 to -0.5			Barrel	σpT/pT ~0.05%×pT+0.5%	~5% or less X		σxyz ~ 20 μm, d0(z) ~d0(rΦ) ~ 20/pTGeV μm + 5 μm		π suppression up to 1:1E-4	50 MeV	≤ 10 GeV/c	≥ 3 σ	~85%/√E+7%	~500 MeV	
-0.5 to 0.0		Central Detector								50 MeV			~85%/√E+7%		
0.0 to 0.5										50 MeV			~85%/√E+7%		
0.5 to 1.0										50 MeV	≤ 15 GeV/c		~85%/√E+7%		
1.0 to 1.5			Forward Detectors	σpT/pT ~0.05%×pT+1.0%		<100MeV pions, 135MeV kaons	σ_xy ~ 30/pT μm +20 μm	(10-12)%/√E(+1-3%)	3σ e/π	50 MeV	≤ 30 GeV/c		35%/√E		
1.5 to 2.0										50 MeV	≤ 50 GeV/c				
2.0 to 2.5										50 MeV					
2.5 to 3.0				σpT/pT ~ 0.1%×pT+2.0%			σ_xy ~ 30/pT μm +40 μm			50 MeV	≤ 30 GeV/c				
3.0 to 3.5							σ_xy ~ 30/pT μm +60 μm			50 MeV	≤ 45 GeV/c				
3.5 to 4.0			Instrumentation to separate charged particles from photons	Tracking capabilities are desirable for forward tagging						50 MeV					
4.0 to 4.5	↑ e	Auxiliary Detectors								50 MeV			35%/√E (goal), <50%/√E (acceptable)*, 3mrad/√E (goal)		
4.5 to 5.0			Neutron Detection			300 MeV pions		4.5%/√E for photon energy > 20 GeV	<= 3 cm granularity	50 MeV					
>6.2			Proton Spectrometer	σintrinsic(|t|)/|t| < 1%; Acceptance: 0.2 < pt < 1.2 GeV/c											

8.3 Operational Requirements for an EIC Detector

EIC is a unique collider with diverse physics topics, which imposes unique requirements on the detector design. Comparing to modern hadron colliders, such as RHIC and LHC, the EIC has much higher crossing frequency ($\sim$ 100 MHz) and high luminosity (10^{34} cm$^{-2}s^{-1}$). However, the EIC cross section ($\sim$ 50 µb) is much smaller than the proton-proton cross section (40-80 mb from RHIC to LHC), making the EIC collision rate ($\sim$ 500 kHz) and particle production rate (4M charged particle per second) a factor 10-1000 lower than that of RHIC and the LHC. Nonetheless, the EIC has a diverse event topology and is sensitive to the machine background and detector noise. All these effects pose challenges to the operational requirements for an EIC Detector. In this section, requirements are studied with integrated detector and IR simulations.

8.3.1 EIC Collision Rates and Multiplicities

The EIC total *e+p* cross-sections is estimated using the PYTHIA6 event generator as listed in Table 8.3. For each collision Figure 8.1 shows particle production rates for the 20 GeV on 250 GeV beam energy configuration, assuming an instantaneous luminosity of $10^{33}cm^{-2}s^{-1}$. Events were simulated using PYTHIA6, and the total cross section reported by PYTHIA6 was used to scale event counts to rates. No cuts, for example on event Q^2 or particle momentum, were applied. The η-range spans the expected acceptance of the main EIC detector. "Charged" particles refers to electrons, positrons, and charged long lived hadrons, while "neutrals" refers to photons, neutrons and K^0_L.

In response to the collisions, the EIC detector response and data rate is studied using full detector GEANT4 simulations of an EIC detector concept based on sPHENIX [48, 49]. The subsystem multiplicity distributions (Figures 8.2, 8.3, and 8.4) and the average data rate (Figure 8.5) are studied in a simulation combining the EIC tune of PYTHIA6, which samples $\sim$ 50 µb of the *e+p* collision cross section, and the full detector GEANT simulation. At the top instantaneous luminosity of 10^{34} cm^{-1}s^{-1}, the collision-induced zero-suppressed

Table 8.3: Total *e+p* cross-section as a function of electron and proton beam energies. The cross-sections were calculated using PYTHIA6 event generator and should be regarded only as rough estimations.

σ_{tot}(µb)		E_e [GeV]			
		5	10	15	20
E_p [GeV]	50	31.4	38.0	42.1	45.3
	100	38.0	45.3	49.8	53.0
	150	42.2	49.8	54.1	57.8
	200	45.2	52.9	57.9	61.4
	250	47.8	55.5	60.6	64.4

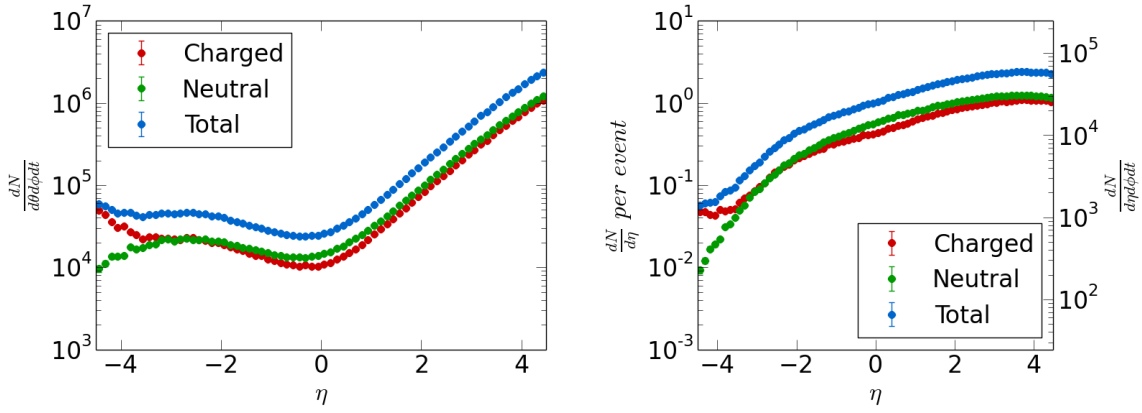

Figure 8.1: Particle production rates as a function of pseudo-rapidity at EIC for 20 GeV on 250 GeV e+p collisions and a luminosity of $10^{33} cm^{-2} s^{-1}$. (a) mean numbers of particles per event (left axis) and particles per second per unit (η, ϕ) (right axis). (b) particles per second per unit (ϕ, θ), i.e., the η-dependent flux at a distance of 1 m from the interaction point.

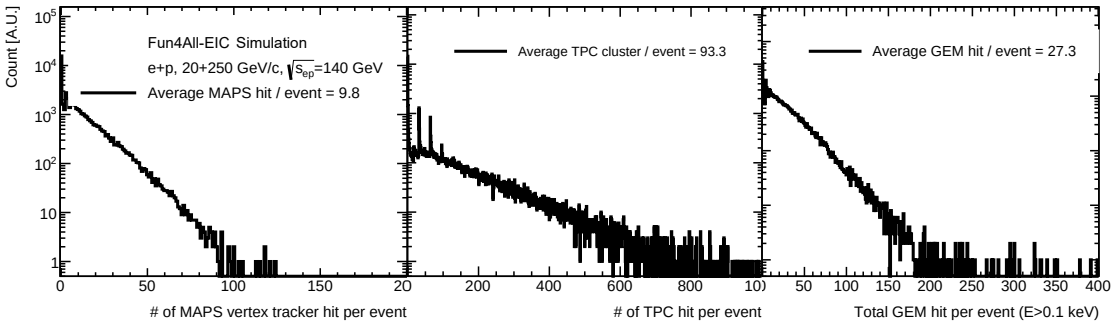

Figure 8.2: Distribution of number of hits in the tracking detectors that originated from a single e+p collision at $\sqrt{s_{ep}} = 140$ GeV.

streaming data rate from EIC collisions is around 100 Gbps, which is the minimal amount of raw data that has to be recorded to disk in order to record all minimum-bias EIC collisions in the central detector without the assumption of online reconstruction and reduction.

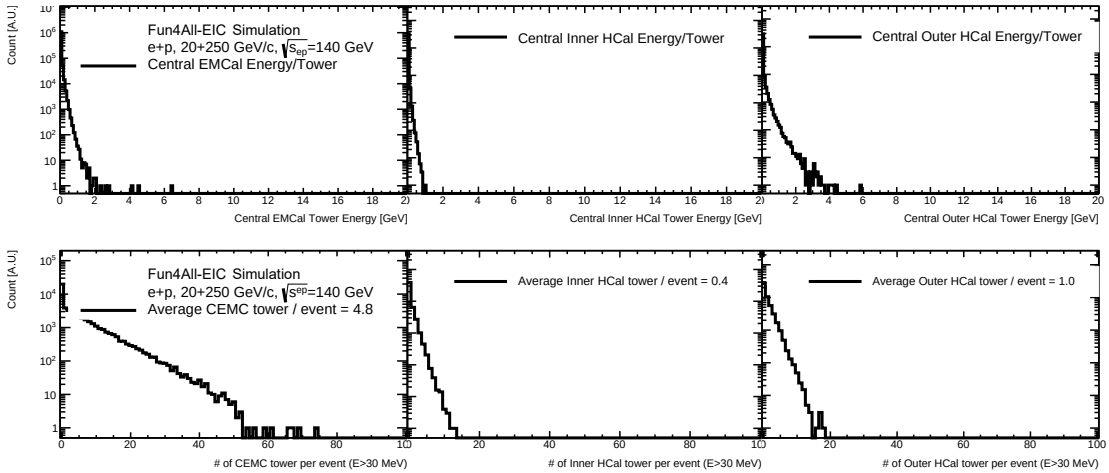

Figure 8.3: Distribution of per-tower energy and the number of active towers in the central calorimeters that originated from a single *e+p* collision at $\sqrt{s_{ep}} = 140$ GeV.

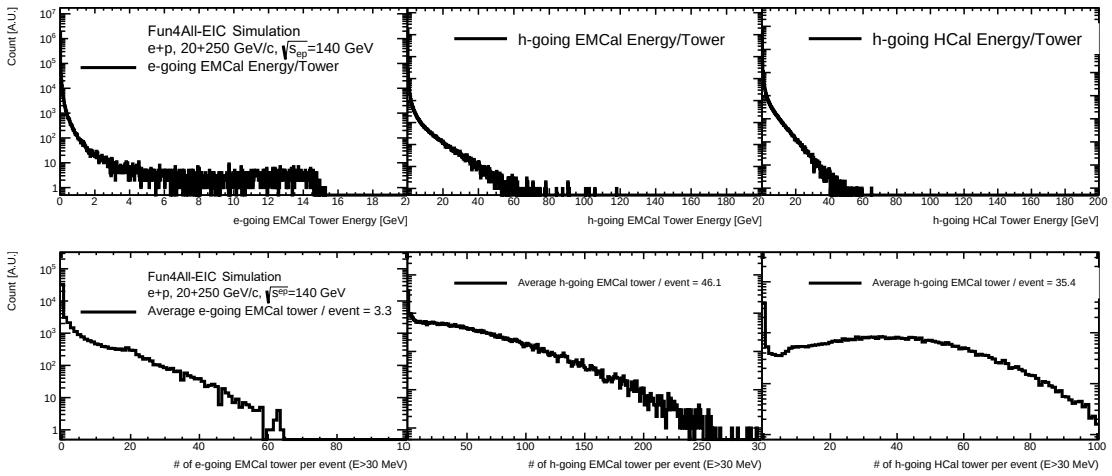

Figure 8.4: Distribution of per-tower energy and the number of active towers in the forward calorimeters that originated from a single *e+p* collision at $\sqrt{s_{ep}} = 140$ GeV.

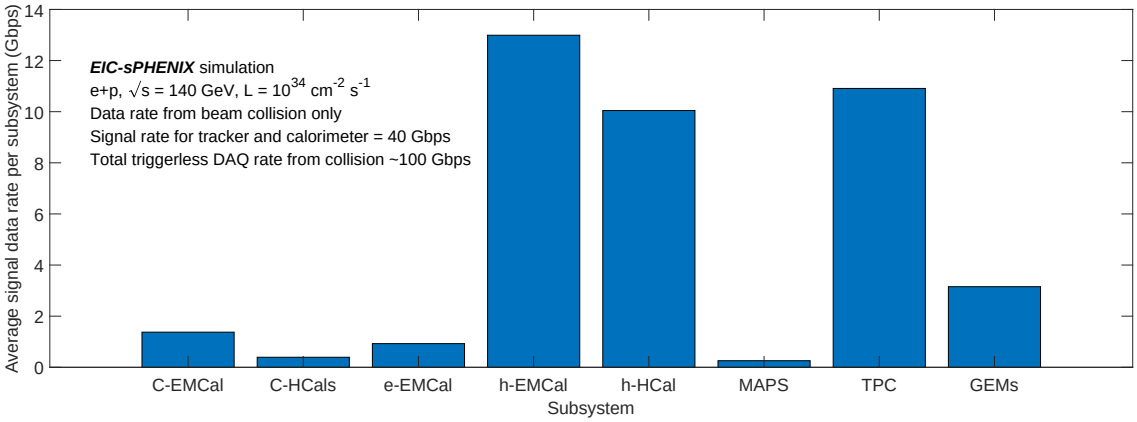

Figure 8.5: Signal data rates from tracking and calorimetric detectors from EIC collisions via full detector GEANT4 simulation of an EIC detector concept based on sPHENIX [48, 49]. Zero-suppression and realistic data format based on sPHENIX prototyping are assumed in this estimation. The overall tracker data rate is 40 Gbps. The estimated rate with PID detector and moderate detector noise would reach 100 Gbps for full experiment. Please note that the backgrounds, e.g. beam gas interaction, excessive detector noise, synchrotron photon hit rate, may dramatically increase the data rate in some detectors, but they are not included in this plot and they will be discussed in Section 8.3.2.

8.3.2 IR Integration and Backgrounds

The combination of the relatively low signal rate of the EIC collision and the stringent systematic control for EIC measurements calls for low background and detector noise at an EIC experiment. And in turn, the types and levels of background is one of the main consideration on the detector design and it is a major consideration for IR integration, such as the arrangement of beam magnets and other beam parameters and optics. The experience at earlier accelerator facilities, especially the previous HERA electron-proton collider, indicates the importance of background studies in the early design phase. Primary sources of machine-induced background are discussed in this subsection.

Ionization radiation dose and Neutron flux from the EIC collisions

The ionization radiation dose and neutron flux from the *e*+*p* collisions are studied using EICROOT and the BeAST detector concept placed in the RHIC IP6 experimental hall. The simulation is generated with the EIC tune of PYTHIA6 with 20×250 GeV beam energy and is based on GEANT3 package with the $HADR = 5$ option. As shown in Figure 8.6, the near-beam-line regions experience relatively high ionizing radiation. For example, the e-going crystal calorimeters show approximately 2.5 kRad/year max ionizing radiation dose from the *e*+*p* collisions at the top luminosity ($10^{34}\,\mathrm{cm}^{-2}\mathrm{s}^{-1}$). The above-100 keV neutron flux is shown in shown in Figure 8.7. The near-beam-line regions, in particular the vertex tracker and the forward-backward calorimeters also experience relatively high neutron flux, exceeding 10^{10} neutrons/cm^2 per year from the *e*+*p* collisions at the top luminosity ($10^{34}\,\mathrm{cm}^{-2}\mathrm{s}^{-1}$).

Synchrotron radiation

Various sources of synchrotron radiation could have an impact on the background level at the IP. When the trajectory of a charged particle is bent, synchrotron photons are emitted that are tangential to the particle's path. Bending and focusing of the electron beam is the main cause of synchrotron radiation within the IR. However, contributions from the upstream electron beam scattering off residual gas must be assessed as well. It is important to place the IP far away from strong bending magnets in the arcs to minimize synchrotron radiation. The tracking detectors in the central detector as well as the calorimeter have to be properly shielded against synchrotron radiation, therefore a number of absorbers and masking must be applied along the electron beam direction. Synchrotron radiation also deposits several kilowatts of power into the beam pipe in the central detector region, which must then be cooled. Additionally, synchrotron radiation can degrade vacuum quality by causing material desorption from vacuum chamber walls and/or heating residual gas. Synchrotron radiation is also a direct and indirect source of background in the luminosity monitor, and low-Q2 tagger located on the downstream electron side of the IR.

A model of the electron beamline has been used in SynRad [50], where synchrotron radiation at the maximal design value of 0.260 Amp of 18 GeV electrons, including 26 mA in a

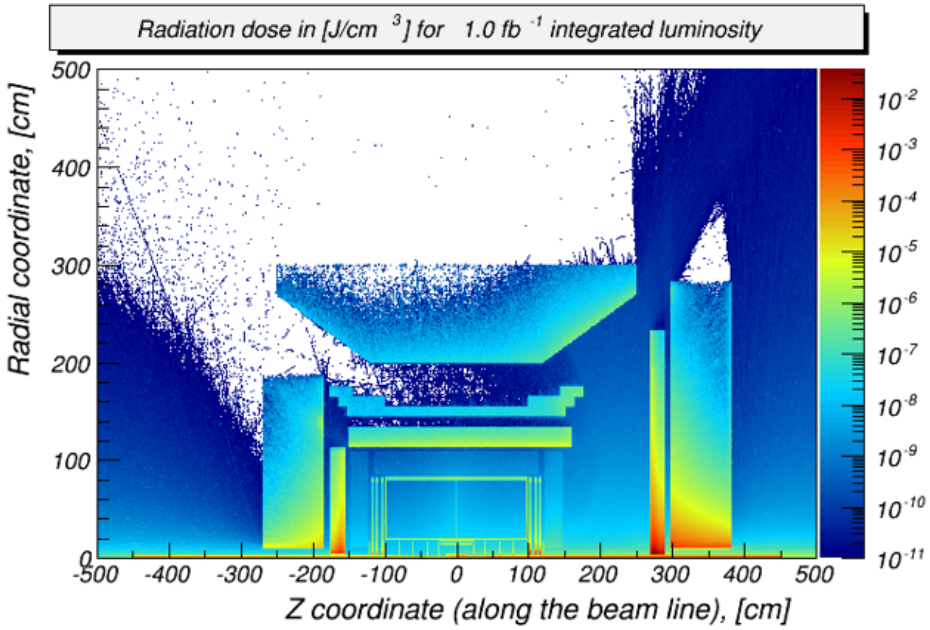

Figure 8.6: Ionizing radiation energy deposition from the e+p collision at $\sqrt{s_{ep}} = 140$ GeV studied using the BeAST detector concept.

broad tail distribution, has been generated. Figure 8.8 shows a view of the upstream electron beamline and IP, with synchrotron radiation generated by the last upstream dipole and FFQ quadrupoles. Electrons enter from the lower left on the figure, at the location of the last dipole, $\approx$ 40 m from the IP. In the background, the IP itself is obscured by the hourglass shape of the central region of the beam pipe.

The energy deposition in the Be beam pipe and Si Vertex Tracker layers is illustrated in Figure 8.10. The dose (energy per mass) in the Si layers is plotted in the right panel of Figure 8.10. The photon flux in these figures is integrated over 0.465 µs of an 18 GeV electron beam at the design current of 0.26 A, including a beam tail.

Furthermore, a GEANT4-based tool-set is being prepared to examine the hit rate that originates from the synchrotron radiation background in the full experiment apparatus. The SynRad synchrotron radiation simulation [50] as prior discussed is interfaced with the detector response as modeled in full detector GEANT4 simulations and the digitization model of an EIC detector concept based on sPHENIX [48, 49], as illustrated in Figure 8.11. The detector hit rate results are pending updated with the July-2020 beam chamber and optics adjustment.

Beam gas interactions

Beam-gas interactions might occur when proton or ion beam particles collide with residual beam gas. Ion beam interactions with gas cause beam loss and halo which may reach

detectors. This may be an important source of neutrons that thermalize within the detector hall. The large synchrotron radiation load could heat the beam pipe and residual gas particles from the beam pipe walls could be released, which would lead to a degradation of the vacuum. A crossing angle and short section of shared beam pipe in the EIC design minimize the beam-gas problem.

A model of the interaction region-1 (IR1), $\pm$ 30 m, including all magnets, the tunnel walls, the detector cavern, and a simplified representation of the detector have been created in FLUKA. This is illustrated in Fig. 8.12. A more detailed view of the detector model is presented in Fig. 8.14.

The studies of the dynamic vacuum in the IR are directly linked to the synchrotron radiation flux impacting the beam pipe. Figure 8.13 illustrates the static vacuum (without synchrotron radiation) in IR1, based on nominal out-gassing rates, the molecular flow conductance of the beam pipe, and the pumping speed of the NEG pumps at $\pm$4.5 m.

In order to efficiently simulate the interactions of the ion beam with the residual gas in the beam-line vacuum, we artificially create a thin "pencil" (diameter 3mm) of air at pressure $P_F = 100$ mbar along the beam-line. A global view of the neutron fluence is presented in the top panel of Figure 8.15. The simulation includes the full cascading and thermalization of secondaries from the primary beam-gas interactions. The figure illustrates the fact that the detector itself, especially the iron flux return, serves as both a neutron sink and neutron source.

The energy spectrum of beam-gas induced neutron at the central Si Vertex Tracker (SiVT)

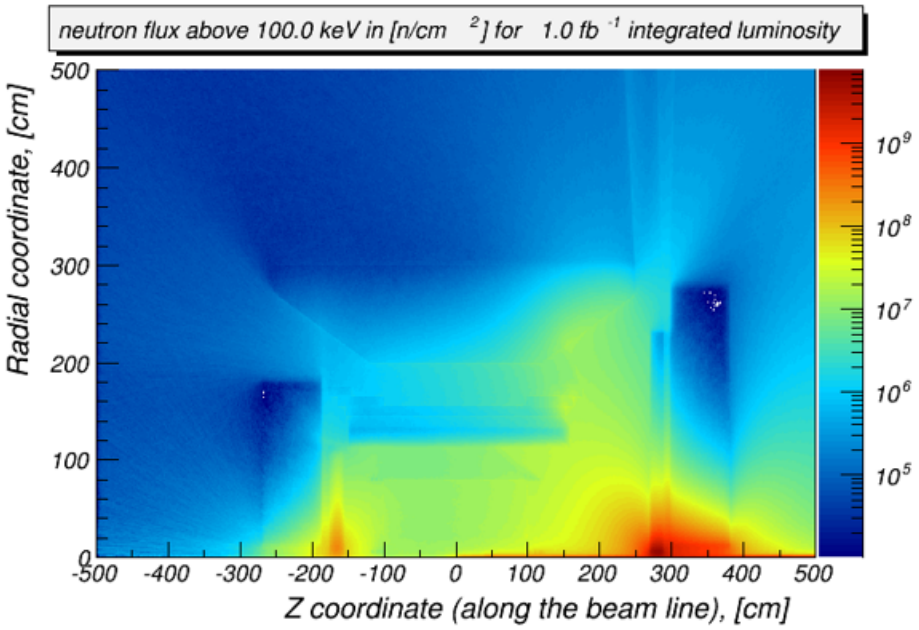

Figure 8.7: Neutron flux from the e+p collision at $\sqrt{s_{ep}} = 140$ GeV studied using the BeAST detector concept placed in the RHIC IP6 experimental hall.

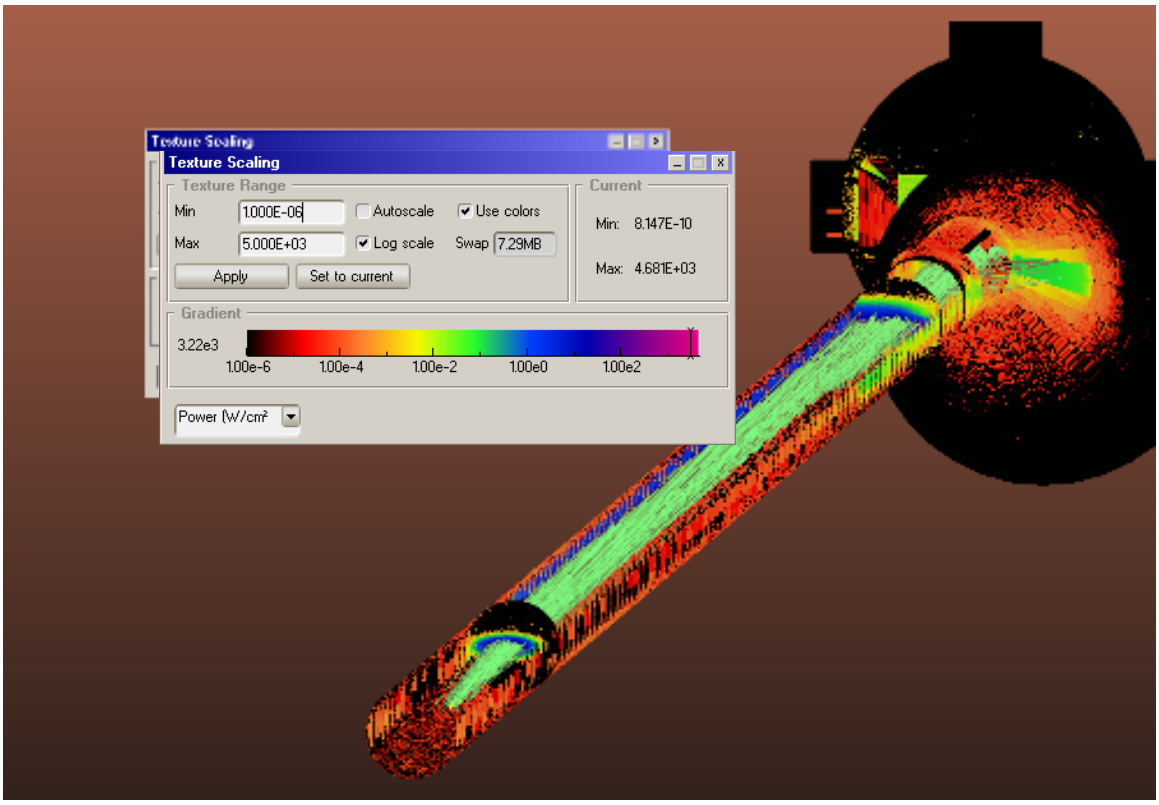

Figure 8.8: SYNRAD generation of synchrotron radiation from 0.260 A of 18 GeV electrons. The color scale is logarithmic, with blue approximately 1 W/cm^2. Electrons enter from the lower left in the figure, the initial radiation fan is generated from the last dipole, at approximately 40 m upstream of the IP. Individual photons are traced by the green lines. The vertical striations on the beam pipe result from the sawtooth inner profile of the pipe, which ensures photons hit the wall locally head-on.

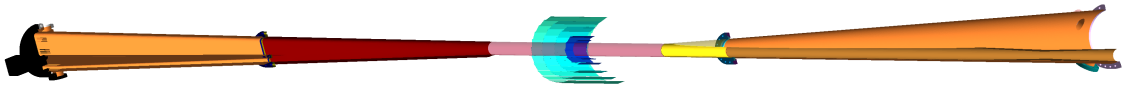

Figure 8.9: GEANT4 model of IR1 Beam Pipe, with Si Vertex Tracker. The electron beam enters horizontally from the right, and exits in the rectangular beam channel to the left. The ion beam enters in the small tube on the lower left, and exits via the large cone on the upper right.

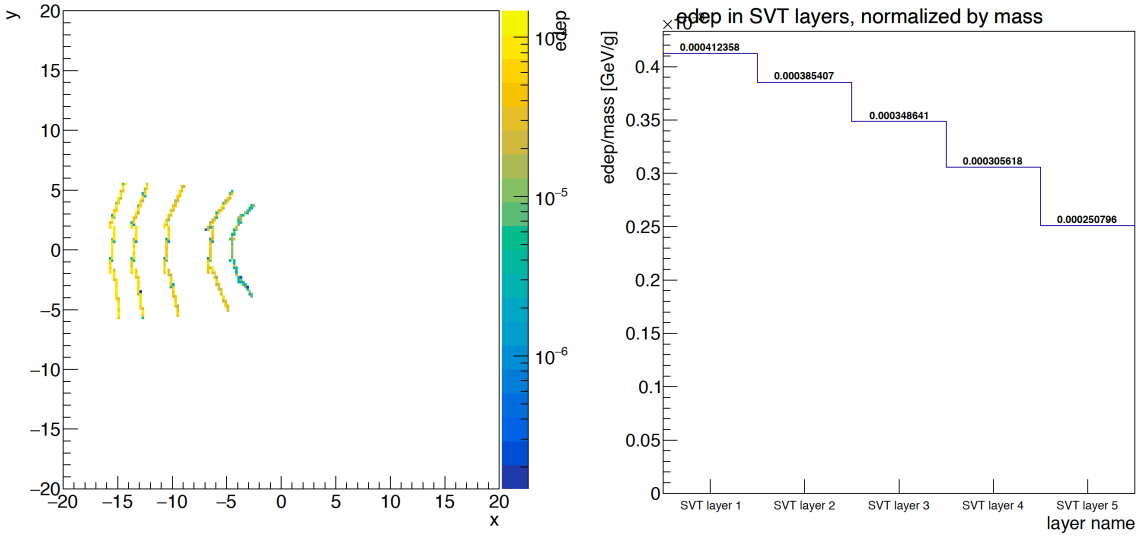

Figure 8.10: Left: synchrotron energy deposition in central Be pipe and 5 layers of SiVT. Energy is integrated over the length of each element. Right: synchrotron radiation dose (GeV/gram) in each of 5 layers of SiVT, which is averaged over the length of each element. The photon flux in these figures is integrated over 0.465 μsec of an 18 GeV electron beam at the design current of 0.26 A, including a beam tail.

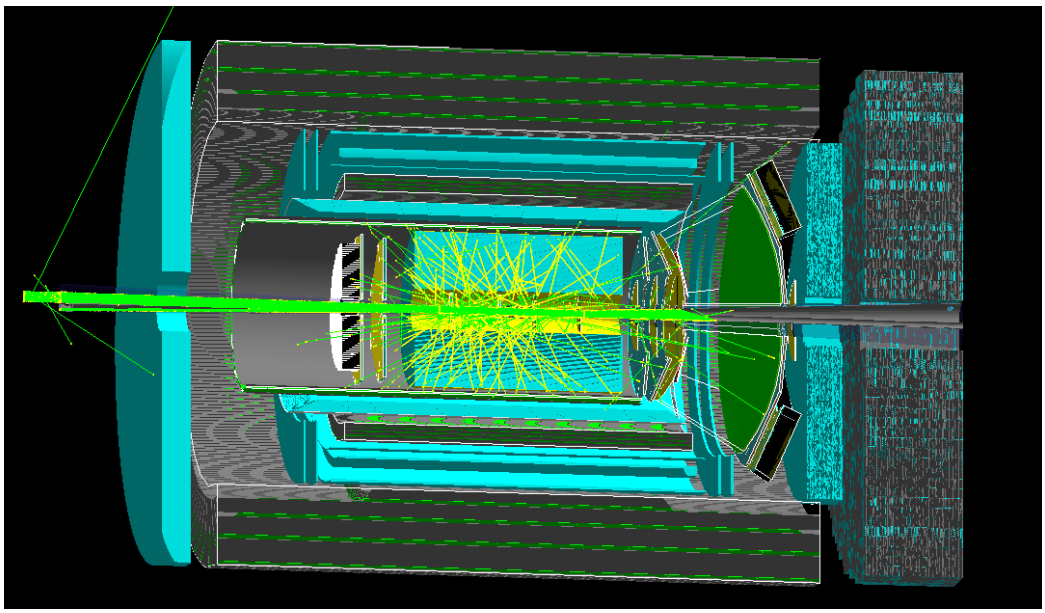

Figure 8.11: GEANT4 simulation of the synchrotron photon background in an EIC detector model [48, 49]. The photons (green lines) are generated in SynRad simulation [50] and the photons are interfaced to the GEANT4 simulation after passing the Final Photon Absorber around $z > 3$ m. Although the inner detectors have the highest flux of synchrotron photon background, the background affects tracking and PID detectors in much higher radii too, due to the scattering and secondary interactions.

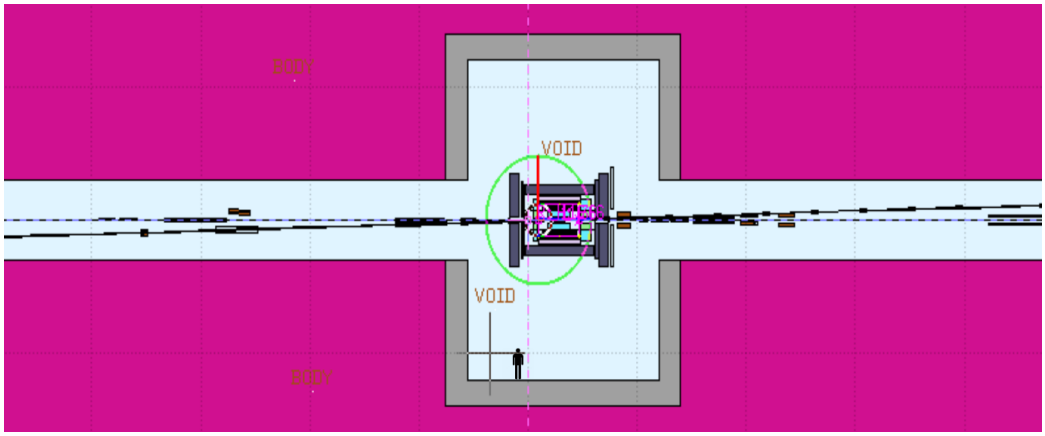

Figure 8.12: Top view of a FLUKA model of the EIC Interaction Region 1 (person for scale comparison is shown at the bottom). Ions enter from lower left, electrons enter on the solenoid axis from the right.

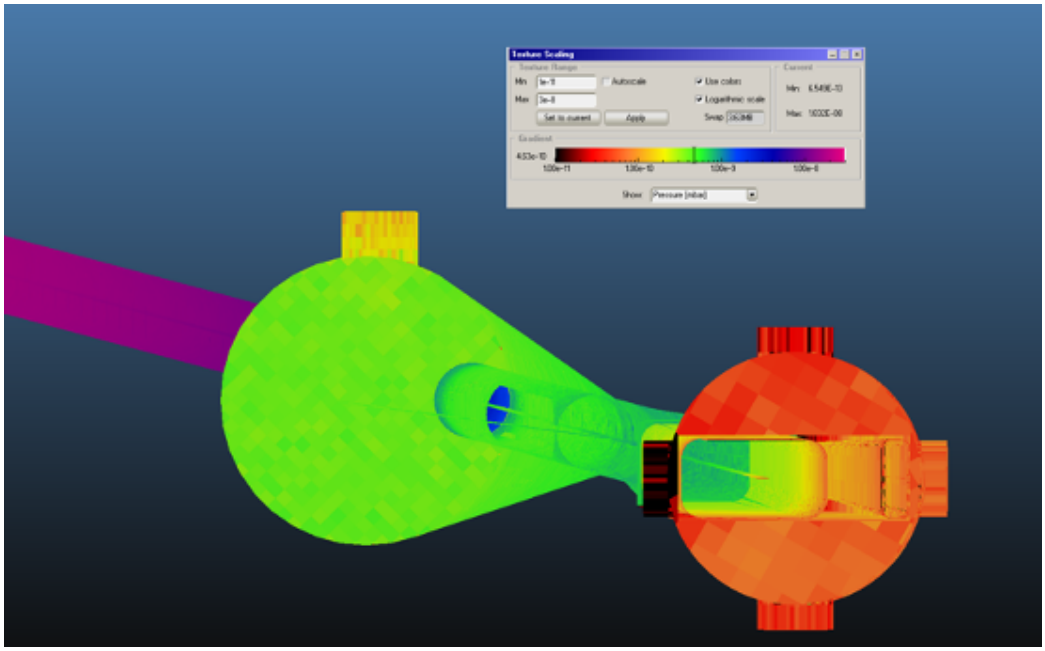

Figure 8.13: MOLFLOW calculation of the static vacuum in the IR. The beam pipe layout is the same as Fig. 8.8. In this view, the electron beam enters from the upper left and exits through the large horizontal aperture on the right. The incident ions enter from the right at $z = -4.5$ m via the smaller upright rectangular aperture. The light green color in the central region indicates a vacuum of $\approx 5 \cdot 10^{-9}$ mbar. The downstream ion beam pipe is not shown beyond the flange at $z = 4.5$ m.

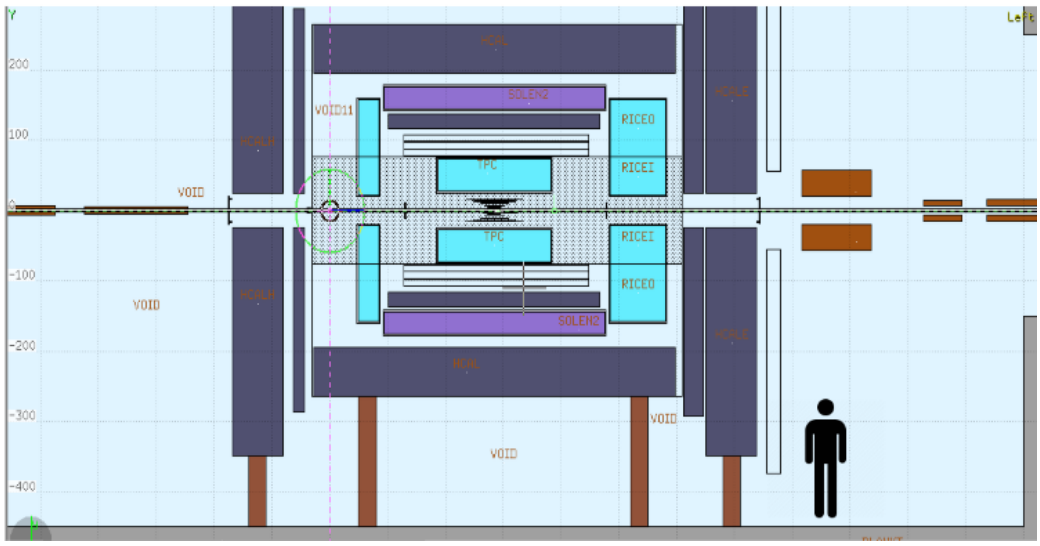

Figure 8.14: Elevation view of the FLUKA model of the EIC Detector. The Si Vertex Tracker (SiVT) in this rendition includes six layers.

is illustrated in Fig. 8.16. The energy distribution shows a clear peak of fully thermalized neutrons below 1 eV, as well as a knee around 10 MeV from evaporation neutrons. Neutron damage to Si sensors occurs primarily via displacement of nuclei from their ideal lattice positions. This can happen both by direct nSi scattering, and also by recoil from Si(n,γ) reactions. The latter can dislodge nuclei, even for neutron energies well below 1 eV.

The damage induced by neutrons is frequently quantified by an equivalent flux of 1 MeV neutrons. This is computed in the bottom of Figure 8.15. From Fig. 8.17, we obtain an annual dose of $6 \cdot 10^{10}\text{n/cm}^2$ (1 MeV equivalent) in the SiVT. This is more than three orders of magnitude less than the suggested tolerance of 10^{14}n/cm^2.

Next we we further estimated the data rate across the whole experiment that originated from the beam-gas interactions. The full detector simulation model as described in subsection 8.3.1 is used to simulate the proton beam hydrogen gas interaction generated with PYTHIA8 in the $p+p$ fixed-target configuration. The hydrogen gas pressure is assumed to be a constant 10^{-9} mbar across the experimental region $|z| < 450$ cm, which leads to approximately 10 kHz inelastic beam gas interaction rate. The result collision is propagated through the detector model as illustrated in Figure 8.18. The result data rate is summarized in Figure 8.19.

Beam halo

Particles produced from elastic collisions of both electron and proton beams with residual gas or beam-beam interactions can form a halo distribution around the beam. Often the result is an on-momentum electron or ion with large scattering angle. These particles can

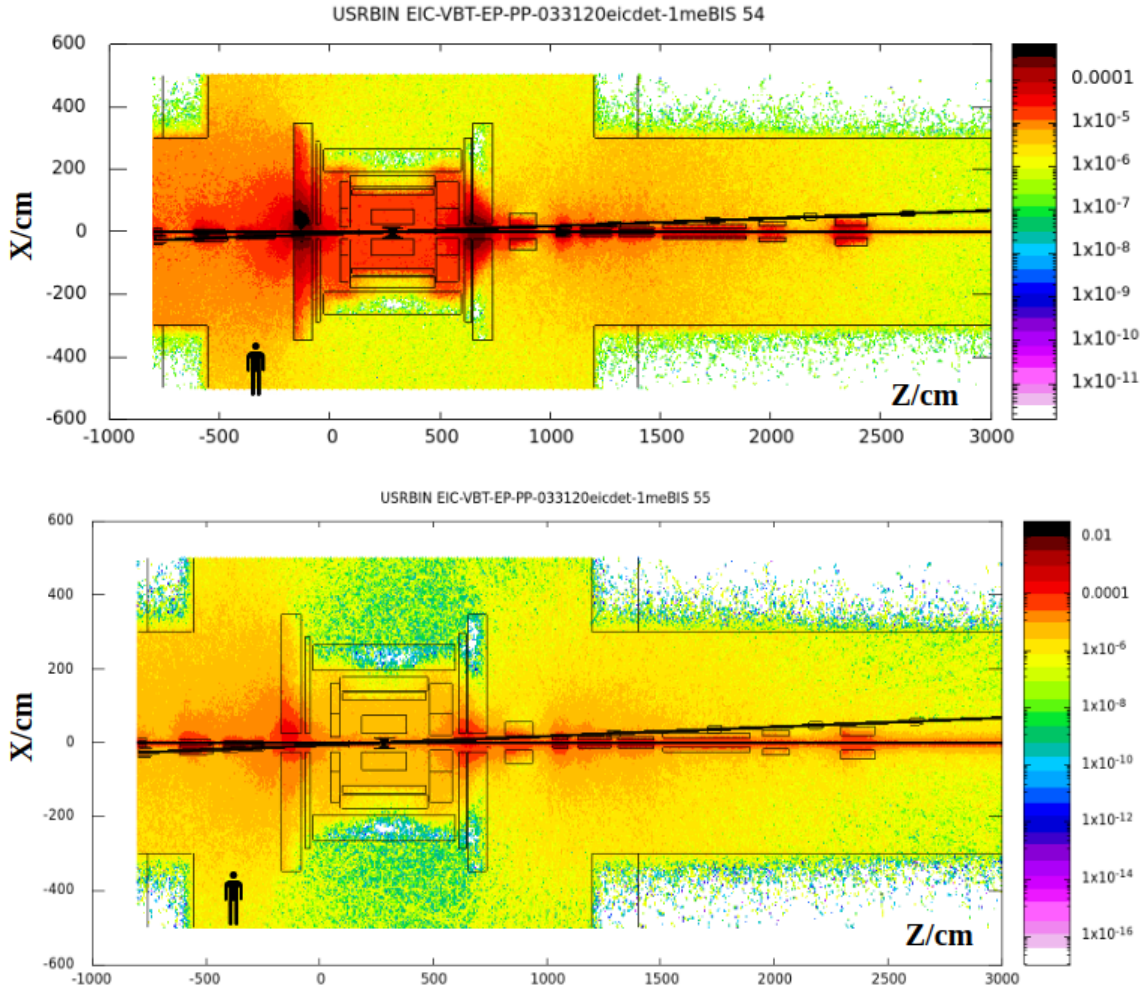

Figure 8.15: Maps for Neutron fluence (top) and 1-MeV-equivalent Neutron fluence (bottom) from $p + Air$ interactions in the beam pipe at proton energy $E_p = 275\,\text{GeV}$ and an artificial pressure P_F ("P-FLUKA") in a thin cylinder along the beam line. The IP is located at $Z = 285$ cm. Neutron fluence is given by the color chart at the right side of the plot in units of neutrons/cm^2/proton at $P_F = 100$ mbar. Normalized rates for current $I = 1$ A and a realistic average beam-line vacuum $P = 10^{-9}$ mbar are obtained by multiplying the color values by $(I/e)(P/P_F) = 6.25 \cdot 10^7$ protons/s. Thus dark red regions (almost yielding to black) correspond to a realistic fluence of $\approx 6 \cdot 10^4$ neutrons/s/cm^2.

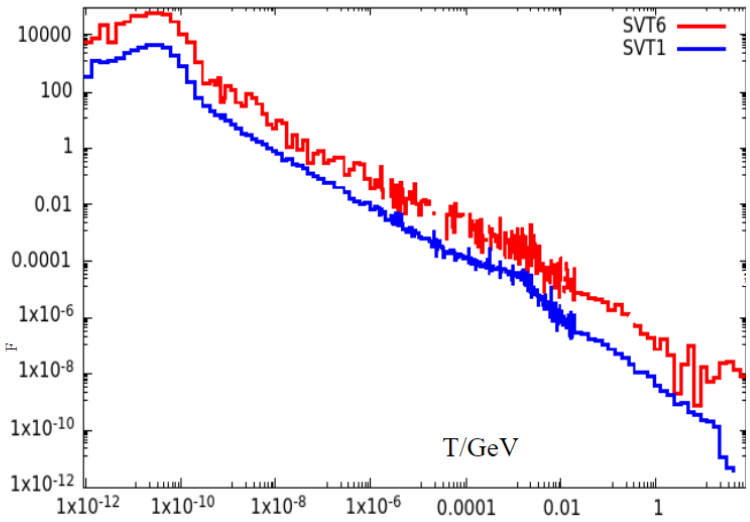

Figure 8.16: Neutron energy spectra from FLUKA simulations in two layers of the SiVT : (1) Outer-most Si layer (SVT1) and (2) Inner-most Si layer (SVT6). The vertical scale is fluence in units of $neutrons/GeV/sr/cm^2/proton$ at pressure $P_F = 100$ mbar. The horizontal scale is neutron energy in GeV. Absolute realistic flux in neutrons/s/sr/cm^2/GeV is obtained by multiplying the vertical axis by $\approx 6.25 \cdot 10^7$ protons/s (see Fig. 8.15 caption).

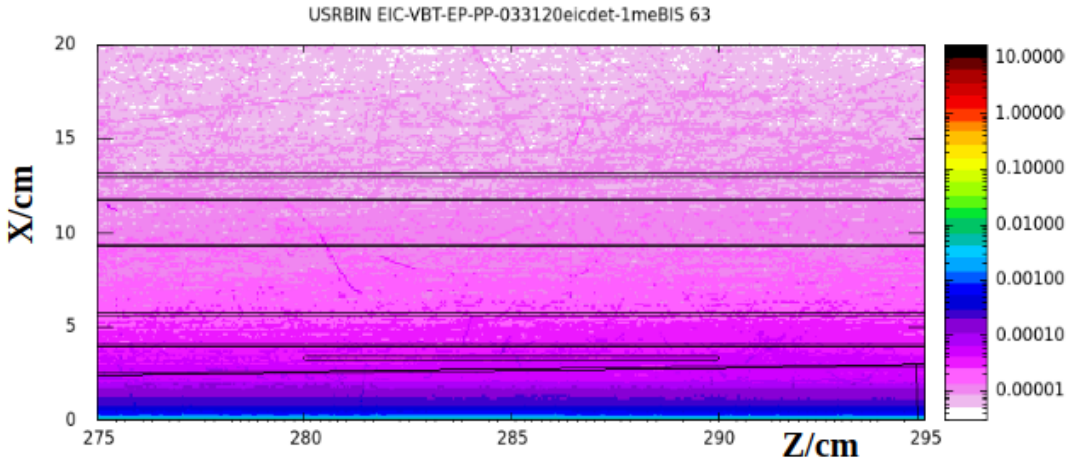

Figure 8.17: One-MeV equivalent neutron fluence map in the area of SiVT; $p + Air$ interactions in the beam pipe at proton energy $E_p = 275$ GeV. IP is located at $Z = 285$ cm. Fluence is given by the color chart at the right side of the plot in units of neutrons/cm^2/proton/P_F, where $P_F = 0.1$ bar is the pressure used in the FLUKA model.

then generate additional background by interacting with the beam pipe and can impact the stability of the beam. Beam halos are being studied to determine whether "scraping" the halo with collimators is required, as well as proper placement of those collimators.

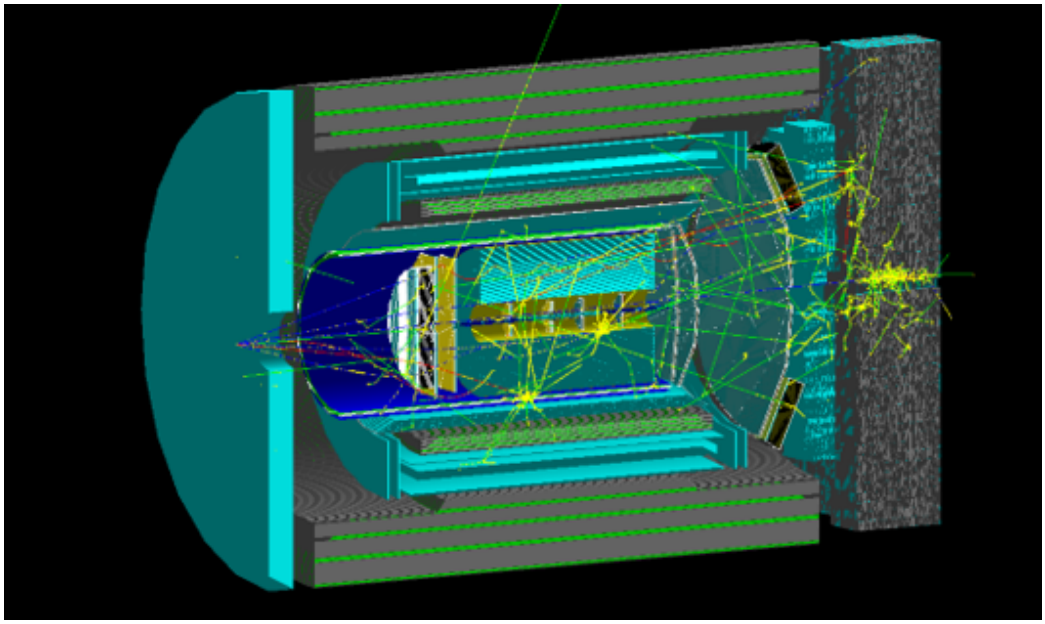

Figure 8.18: GEANT4 simulation of a beam gas interaction background in an EIC detector model [48, 49]. The interaction originate after the last focusing magnet at $z = -4$ m. The produced particle shower will cascade through the central detector stack and induce high multiplicity background throughout the forward and backward spectrometers.

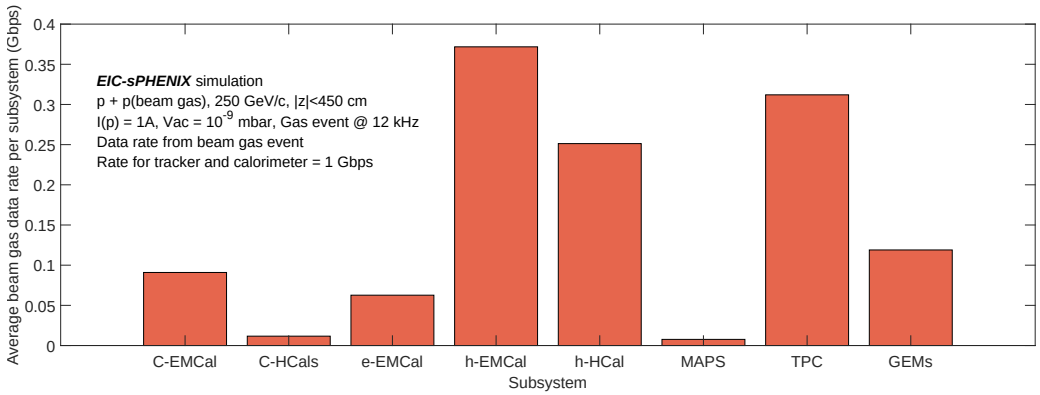

Figure 8.19: Signal data rates from tracking and calorimetric detectors from beam gas collisions via full detector GEANT4 simulation of a detector concept based on sPHENIX [48, 49]. This simulation assumes constant 10^{-9} mbar vacuum in the experimental region of $|z| <$ 450 cm, which would be modified with a dynamic vacuum profile in the future.

Summary and outlook

Although multiple background sources are discussed in this section, at the time of this report, many aspects of these background estimation can still vary considerably as the accelerator and experiment conceptual design proceeds. Nonetheless, we feel it crucial to point out a few key experimental regions which are susceptible to high background.

- A silicon vertex tracker is expected to be installed with a minimal clearance outside the beam pipe in EIC. The overall collision charged particle flux is relatively low (Section 8.3.1). However, the proximity to the beam pipe exposes this detector to the background such as the synchrotron radiation, beam gas interactions, and beam halo. The current estimation shows an annual neutron fluence reaches $O(10^{11})n/\text{cm}^2$. The synchrotron hit rate ranges from $O(10^8)$ to $O(10^{12})$ pixels per second, depending on the choices of the beam chamber coating. Optimization on the machine and detector design is ongoing to reduce and refine the background rate and to protect this key detector from unexpected beam conditions.
- In addition to the silicon vertex tracker, many tracking and PID detector would observe a considerable hit rate from the scatter synchrotron photons, in particular the main barrel tracker and forward-backward silicon tracker, as illustrated in Figure 8.11. Optimization and detailed estimation are still ongoing.
- Hadronic shower leads to enhanced neutron fluence near the first few hadron interaction lengths of calorimeters at the vicinity of the beam pipe. Current estimations are at the orders of $O(10^{10})n/\text{cm}^2$. Further study and refinement will be carried out.

8.4 Reference EIC Detector

8.4.1 Introduction

The physics opportunities at EIC are intimately connected to the overall design of the experiments and to the performance of the required detectors. From the experimental point of view, the broad physics EIC program can be accomplished by the study of (i) inclusive, (ii) semi-inclusive and (iii) exclusive processes, all of them with initial state of electrons and light or heavy nuclei, with polarized electron and light nuclei beams and spanning a wide range of center of mass energies. The main requirements for the experimental apparatus are based on these processes and the requirements of the wide kinematic coverage, adding more and more complexity moving from reactions (i) to (iii):

- Precise scattered electron identification and extremely fine resolution in the measurement of its angle and energy (Sec. 8.4.2) for all experimental channels; another essential tool for the whole physics scope is the central magnet (Sec. 8.4.3) required for momentum measurements;
- More is needed to access the semi-inclusive processes (ii): excellent hadron identification over a wide momentum and rapidity range, full 2π acceptance for tracking and momentum analysis and excellent vertex resolution by a low-mass vertex detector (Sec. 8.4.2);
- Exclusive reactions (iii) impose the capability to accurately reconstruct all particles in the event using a tracker with excellent space-point resolution, high precision electromagnetic resolution and reasonable precision hadronic calorimetry in the end-caps (Sec. 8.4.2), the complete hermeticity of the setup with the additional requirement of very forward detectors such as Roman pots, and large acceptance zero-degree calorimetry to effectively detect neutrons from the breakup of nuclei or neutral decay products from tagged DIS processes (Sec. 8.4.4);
- The entire experimental program will require the precise control of the luminosity (Sec. 8.6);
- The polarized beams impose the use of electron and light nucleus polarimeters (Sec. 8.6);
- The strategy for detector read-out and data acquisition has to be defined taking into account the data rate of the experiment as well as the rapid developments in the field of digital electronics and computing power, suggesting a global approach to the read-out and data acquisition (Sec. 8.4.5) on the one hand and software and computing on the other hand (Sec. 8.5).

8.4.2 General Purpose EIC Detector

A reference detector design, closely following the physics requirements outlined in chapter 2.3, is shown in Figure 8.36. The general requirements for any detector are similar as they stem from the central goal to cover the entire EIC physics program, the expected event geometries and the constrains coming from the overall collider design. Nevertheless, the detector design and the selected technologies may differ.

We assume the following characteristics for the present discussion. The central detector, discussed in this section, instruments the pseudo-rapidity region $-4 < \eta < 4$. It is complemented by the very forward and backward detectors (Sec. 8.4.4) ensuring the hermeticity and the forward tagging required by specific items of the physics program. The main requirements of the central detector dictated by the physics program and the event geometry are related to **(1) tracking and momentum measurements, (2) electron identification, (3) hadron identification** and **(4) jet energy measurements**, while (5) the overall detector size is imposed by collider design considerations:

1. very fine vertex resolution, at the 20 µm level for the three coordinates, is needed, while a moderate momentum resolution around 2% matches the physics requirements;
2. the purity requirements for electron/hadron separation are at the 10^{-4} level in the backward and barrel regions and, for this purpose, the figures for the electron energy resolution are very demanding, in particular in the backward region where an r.m.s. of $2\%\sqrt{(}E)$ is needed; in the same direction, the request is for a light detector, where the material budget should not exceed 5% X_0;
3. the identification of the different hadron species in the whole central detector coverage, namely for hadrons with momenta up to 50 GeV/c, is requested with 3σ π/K separation over the whole range as reference figure;
4. the measurement of jet energy in the forward direction is a necessity, while moderate resolution of the order of $50\%\sqrt{(}E)$ can match the needs;
5. the detector extension along the beam lines impacts on the required length around the IP that has to be kept free of machine elements, typically referred to as L^*: the reference figure is $\pm$4.5 m space around the iteration point.

The required **tracking and momentum resolution** measurements can be obtained with a $\sim$1.5 T solenoidal field equipping the internal volume with a set of coaxial trackers with cylindrical symmetry covering the $-1 < \eta < 1$ region and a set of disk-shaped detectors in the forward and backward direction. Different approaches are considered for the set of tracking detectors. The better established is via a vertex barrel formed by 4 layers of high-resolution **MAPS sensors** with a 20 µm pixel size and an effective thickness of only $\sim$ 0.3% radiation length per layer. The barrel is surrounded by a **TPC**, with internal radius of 20 cm and external one of 80 cm, specifically chosen as the main tracking element because of its small overall material budget as it minimizes the rate of photon

conversions in detector components. The longitudinal extension of the TPC is longer than the vertex layers: therefore, the TPC provides tracking also in part of the forward and backward regions, while the small angle regions are covered by small-size disk trackers by the same technology used for the vertex barrel. Besides this, the TPC should provide charged particle-identification (PID) information at central rapidities complementing the dedicated PID devices. The **disks trackers** are by the same technology used for the vertex barrel. This setup can be empowered by adding a single layer of a high-resolution tracker with fine spatial and time resolution, for instance by micro-RWELL, external to the TPC to provide better angular information. Such a high-resolution tracker is needed if a DIRC is used for PID in the barrel region as it provides fine angular information at the DIRC entrance. It can also contribute to define the event time.

Alternative options for the tracking are considered. The **TPC can be replaced with silicon trackers**, namely increasing the number of layers in the vertex. This would result in a faster detector characterized by finer spatial resolution, even if without the PID capabilities provided by the TPC. The whole silicon tracker option has more limited space requirements, therefore making more space available in the barrel for ECal or PID needs. The length along the beam axis of these external layers is shorter than the TPC one: this detector equips the mere barrel region. Therefore, the diameter of the disk trackers has to be increased in order to cover the forward and backward regions. The most external disk detectors, characterized by the largest diameter, can be replaced by light-material MPGDs: low material budget GEM detectors are considered, where the Cu electrodes are reduced to the mere adhesive Cr-film. Another option, also characterized by low material budget, is **a set of cylindrical coaxial MPGD layers**: microR-WELLs are considered. This option results in a detector faster than the TPC without PID capabilities. A technologically advanced **alternative for the vertex sensors** is represented by a new-generation of **MAPS in 65 nm CMOS imaging technology**, being developed within the ALICE ITS3 project. The sensor specifications and the development timescale are largely compatible with those of the EIC. The expected material budget is only about 0.05% radiation length per layer.

The required **electron identification** as well as measurements of electron kinematical parameters can be obtained with a set of electromagnetic calorimeters of cylindrical symmetry in the barrel region and a set of rectangular shaped detectors in the forward and backward direction. Different approaches are considered for the set of electromagnetic calorimeters as illustrated in Table 8.4.

For hadron physics measurements with electromagnetic probe, good energy resolution and high granularity is needed in the electron-going (backward) direction to detect and identify electrons, photons and neutral pions. Good energy resolution aids in electron-pion separation and to determine the electron scattering kinematics, compactness and high granularity is driven by need for position resolution and separation of single-photons from neutral-pion decays. The EIC high-resolution EM Calorimeters have the following basic requirements:

- Interaction rate capability up to 0.5×10^6 Hz requiring reasonably fast scintillation kinetics

- Sufficient energy resolution and efficiency over a large dynamic range of photon energies, typically from order 50 MeV to 50 GeV
  - In backward region, $\eta <$ -2 or -2.5, energy resolution of order $2.5\%/\sqrt{E}$ to achieve required 10^{-4} π/e rejection (for E $>$ 2 GeV). Or, in other words, to achieve clean electron identification making use of tracking information to determine E/p. For -2 $< \eta <$ -1, an energy resolution of $7\%/\sqrt{E}$ suffices to achieve clean electron identification for E $>$ 2.5-3 GeV
  - In backward and especially far-backward region a small constant term, 1% or less, to aid in determination of electron scattering kinematics. Note that to achieve convergence to good energy resolution including constant term typically requires 20 or more radiation lengths (X_0). For PWO, this is $22X_0$ (20 cm), for CsI 27 X_0 (50 cm).
  - Electron energy range from order 1 GeV to order 20 GeV for $\eta <$ -1, and up to $\sim$40 GeV for $|\eta| < 1$.
  - Photon energy range from order 20 MeV to order several tens of GeV
- Adapted geometrical dimensions to contain the major part of the EM shower
  - Sufficient granularity (0.02-0.03) to separate single photons from π^0 decays
  - In the backward region, at a distance of about 3 meters, need position resolution of order 2-3 mm to pinpoint electron scattering kinematics, and granularity of order 2 cm.
- Moderate radiation hardness up to $\sim$3 krad/year (30 Gy/year) electromagnetic and 10^{10} n/cm^2 hadronic at the top luminosity.

$PbWO_4$ (PWO) meets the requirements of an extremely fast, compact, and radiation hard scintillator material providing sufficient luminescence yield to achieve good energy resolution. Since the highest precision is only needed at very backward rapidities the reference backward endcap electromagnetic calorimeter is a hybrid design with a high-resolution inner part composed of **$PbWO_4$** crystals at room temperature and an outer part composed of radiation-hard **SciGlass**. Due to its larger radiation length, it requires roughly twice the longitudinal length as PWO, for similar energy resolution, but can achieve similar granularity. It also has a high light yield, similar as BGO and CeF_3, that is independent of temperature and high radiation hardness ($>$1000 kRad and $>10^{15}$ n/cm^2). SciGlass is being developed as part of the EIC eRD1 consortium. Successful scaleup has been demonstrated and glass samples of sizes up to $\sim$10 radiation lengths can now be produced reliably. The electron endcap reference hybrid design fulfills the physics requirements and reduces the demand for crystals while keeping the benefits of a homogeneous detector medium.

The reference detector surrounding the barrel is a **Pb/Sc Shashlyk sampling** calorimeter. This technology consists of a stack of absorber and scintillator plates. The light is collected with the help of WLS fibers passing through the plates. For the absorber lead or tungsten are used. The technology is widely used and allows detectors of various resolutions and sizes. The barrel calorimeter provides and energy resolution of $12\%/\sqrt{E}$ or better

to achieve clean electron identification and less than 2-3cm granularity to separate single photons from π^0 decays. In the forward region, at a distance of 3 m, if only done with the EMcal requires granularity $<$ 2.5 cm to identify for momenta up to 50 GeV/c. The reference hadron endcap detector is a **W powder/ScFi sampling** calorimeter. In this technology fibers are embedded into a heavy material like lead or tungsten. In one implementation the fibers are glued between lead sheets. Such SPACAL-type detectors have been used in several experiments. In an alternative implementation, tungsten powder is used for the absorber. This technology has been developed for the sPHENIX experiment.

Alternative options for the electromagnetic calorimeters are provided by replacing the reference with an alternative option studied by the community. The less demanding outer part of the electron endcap electromagnetic calorimeter could be replaced by one of the heterogeneous sampling options listed in Table 8.4. The radiation-hard SciGlass could provide a homogeneous alternative for the large-volume barrel or the hadronic endcap. Another option, characterized by a heterogeneous material approach, is to replace Pb/Sc Shashlyk in the barrel with a different absorber W/Sc Shashlyk or W powder/ScFi, provided that sufficient performance to meet EIC physics requirements can be demonstrated.

The required jet energy measurements can be obtained with a set of **hadronic calorimeters** in the barrel and forward and backward directions. The hadron calorimeters should be compatible with the requirements:

- Sufficient energy resolution and efficiency over a large dynamic range, typically from order 100 MeV to 100 GeV
  - In the forward direction, $\eta > 1$ high resolution $<40\%/\sqrt{E}$ +5% is desired for hadron jet measurements
- Sufficiently high granularity to disentangle the different contributions, i.e. proper assignment of signal to the neutral components of the jet
  - currently anticipated granularity 10 cm $\times$ 10 cm
- Adapted geometrical dimensions to contain the major part of the hadron shower
  - In regions $|\eta| < 1$ and backward region 5 λ_{int} are sufficient as particle energies are $<$ 20 GeV/c
  - In the forward region, $\eta > 2.5$, should be of order 6-7 λ_{int}
- Moderate radiation hardness up to 3 krad/year (30 Gy/year) electromagnetic and 10^{10} n/cm2 hadronic at the top luminosity.
- Compatibility with Particle Flow Approach for jet reconstruction
- Preferably mechanical sturdiness allowing to build self-supporting structures to minimize space required for passive mechanical support structures.

Due to the large size required for hadron calorimeters, these detectors are typically of the sampling type and consist of an EMCal followed by an HCal part. In such a binary system

the performance for electromagnetic energy and hadron energy resolution has to be balanced, e.g. for a high resolution EMCal the hadronic resolution is poor and is determined by fluctuations in the energy sharing between the EM and the hadronic calorimeter section, which have very different e/h values. Precision measurements of energy with sampling calorimeters require sufficiently high sampling fraction and sampling frequency to keep sampling fluctuations and fluctuations in the number of signal quanta (EM energy resolution) at the desired level. An increase in sampling fraction leads to significant dilution of the final density of the calorimeters. In addition, calorimeters with large sampling fraction require additional space for mechanical stability, as they are usually not self-supporting.

The best hadronic calorimeters providing hadron energy resolutions of $\sim 35\%/\sqrt{E}$ + (1.3-3.5)% (ZEUS Depleted Uranium, DU/Sc, E864 Pb/ScFi, and the WA80 DU/Sc ZDC) were compensated. Their total hadronic resolution has been dominated by sampling fluctuations. This is a direct consequence of compensation (e/h=1), which requires small sampling fractions, e.g. 2.3% for Pb/Sc detectors and 5.1% for DU/Sc detectors. To give an idea of required space in the detector for high resolution calorimeter systems; the ZEUS calorimeter system took almost 4 meters of space, half of space occupied by high resolution DU/Sc calorimeter and the rest by backing calorimeter to control longitudinal leakages. The E864 Pb/ScFi calorimeter system takes about 2 meters of space just for Pb/ScFi structure plus an additional 0.7 meters of space for readout.

The reference EIC hadron calorimeter for all detector regions is of the **binary type composed of W/ScFi for the EM and Fe/Sc sampling for the hadronic part**. The steel absorber is preferable over other absorbers like Pb as it allows to serve the dual purpose of magnetic flux return for the overall EIC detector. Steel also generates less neutrons, which can be advantageous for the envisioned SiPM readout. In the backward direction, where particle momenta are at most 20 GeV/c the total depth of the hadronic calorimeter may be less than that in the forward direction that will provide jet energy measurements for particle momenta up to nearly 100 GeV/c. W/ScFi was chosen for the EM part to simplify the construction of an EM calorimeter with high sampling frequency and small sampling fraction (approximately being compensated). This hadronic calorimeter reference design is expected to achieve a hadronic energy resolution of $50\%/\sqrt{E}$ + 10% and spatial resolution of 30mm.

Alternative options for the hadronic calorimeters are provided by replacing the reference with an alternative option studied by the community. In regions where the calorimeter material does not play a considerable role in containing the magnetic field a technology based on a different absorber could be used, e.g. Pb/Sc or DU/Sc. An alternate design with Pb/Sc shashlik for the EM part and Fe/Sc for the hadronic part would also be possible. Another option could be an imaging calorimeter based on silicon RPC/DHCAL, which could provide additional particle identification information and possibly improve the jet energy resolution. One of the most promising methods to achieve better performance for hadronic calorimeters is dual readout. By comparing the signals produced by Scintillation light (S) and Cherenkov light (C) in the same detector, the EM shower fraction, whose fluctuations are the main culprit for problems encountered with hadronic calorimetry, can be determined for individual events. The validity of this principle has been demonstrated

with the DREAM fiber calorimeter. However, two factors impacting hadronic resolution remain: sampling fluctuations and fluctuations in the Cherenkov light yield. Homogeneous materials such as crystals and glasses in which both S and C light are generated in the same optical volume have the potential to eliminate these two issues.

Hadron identification requires different approaches and technologies in the various regions of the central detector in order to cover different momentum ranges and because of different space constraints imposed by the overall setup arrangement.

The reference option for hadron identification in the barrel region is by a **high performance DIRC** complemented by **dE/dx measurements**. The DIRC focuses Cherenkov light released and internally reflected in precision quartz bars. The light is channeled away from the central region for detection providing a compact system with photon sensors outside the detector acceptance. High performance is obtained by adding full focalization to the BABAR DIRC concept. It is so possible to obtain 3σ π/K up to 6 GeV/c.

The measurement of dE/dx complementing the particle identification in the barrel is provided by tracking technologies, e.g. TPC. TOF options in the barrel region are not promising because of the short lever arm available. In the forward region, the **dRICH (dual RICH)** is the reference detector. It includes two radiators, namely a fluoro-carbon gas and aerogel, can cover a wide momentum range with π/K separation at 3σ level or better from 3 GeV/c to 60 GeV/c. An array of mirrors focalizes the light onto an area with limited instrumentation outside the RICH acceptance with reduced constraints on material budget and radiation tolerance. This facilitates the possibility to use SiPMs as photon sensors, able to operate in magnetic field and to detect single photons. The capability of tolerating the foreseen radiation levels requires confirmation.

The reference hadron-PID device in the backward direction is the **modular RICH**: it uses aerogel radiator in a proximity-focusing arrangement, where the resolution is increased thanks to the use a Fresnel lens as focusing element. The Fresnel lens also filters short wavelength light, which suffers in aerogel by severe Rayleigh scattering dispersion. It can use either SiPMs or Large Area psecPhoton Detectors (LAPPD) as sensors. It provides 3σ π/K separation up to 10 GeV/c. A characterizing aspect of this option is the modular construction, a design that simplifies construction, quality control and assembly of a large system.

Alternative options for hadron-PID are considered for all the various kinematic regions. In the barrel, the **BaBar DIRC** bars can be reused, even if posing mechanical problems related to the bar length. Moreover, it would result in a 3σ π/K separation up around 4 GeV/c. TOF options in the barrel region are not promising because of the short lever arm available. In the forward direction, an alternative is a **windowless gaseous RICH**, where the gas radiator also provides the atmosphere of the gaseous MPGD-based sensors. In this case, the use of a single radiator species makes possible the design of a central optics, limiting the effect of the spherical aberration. This gaseous RICH requires to be complemented by a device for lower momenta making use of aerogel, e.g. mRICH modules, or TOF measurements taking advantage of the $\sim$3 m lever arm available. In both dRICH and windowless RICH, an ecofriendly alternative to the C-F gas is represented

by **pressurized Ar**. Varying the pressure up to about 3.5 bar, Ar can mimic C-F gasses providing the same favorable figures for high Cherenkov photon yield and limited chromaticity. In the backward region, similarly to the forward region, the lever arm for a possible TOF system is of a few meters and, therefore, also this option is considered. About **TOF technologies**, two fine time-resolution sensors are considered: **LAPPD**s, based on the MCP principle, detecting the Cherenkov light generated in the window by the through-going ionizing particle with 5-10 ps time resolution and **Low Gain Avalanche Detectors (LGAD)**, with 20-35 ps time resolution and also providing an accurate space point for tracking.

The devices for hadron identification, can also contribute to **electron/pion separation**, where the electromagnetic calorimetry play the major role. Nevertheless, the separation power by calorimeters is optimal only above $\sim$4 GeV/c and it depends on the technology: it can be at the 10^{-4} for $PbWO_4$ crystals, while it is around 10^{-2} for heterogeneous sampling options. In the backward region, mRICH can provide 3σ e/π separation up around 2 GeV/c, in the forward region dRICH is capable of 3σ e/π separation up around 15 GeV/c. No relevant contribution can come from the DIRC, due to the high refractive index of the quartz radiator. An **alternative option for electron/pion separation** in the backward region is the use of a **Hadron Blind Detector (HBD)** using CF_4 radiator, similar to the one used in the PHENIX experiment, with pion threshold at $\sim$4 GeV/c. Improvements in the MPGD-based photon detectors can be implemented with the addition of more multiplying layers in the gaseous sensor.

Alternative options for e/h separation are by adding a **TRD** in the forward and backward directions. A TDR concept making use of GEM as sensor is under development and the preliminary indications for the separation power is at the 10^{-1} level. The device can also provide precise tracking information.

Table 8.5 summarizes the subdetector performance parameters obtained by the technologies described above and summarized in table 8.4. The interactive version of this matrix allows to correlated the listed performance with details about the technology and the simulations used to obtain the performance.

Table 8.4: Possible detector technologies for the Main Detector fulfilling the Physics requirements.

system	system components	reference detectors	detectors, alternative options considered by the community		
tracking	vertex	MAPS, 20 um pitch	MAPS, 10 um pitch		
	barrel	TPC	TPC [a]	MAPS, 20 um pitch	MICROMEGAS [b]
	forward & backward	MAPS, 20 um pitch	GEMs with Cr electrodes		
ECal	barrel	Pb/Sc Shashlyk	SciGlass	W powder/ScFi	W/Sc Shashlyk
	forward	W powder/ScFi	SciGlass	Pb/Sc Shashlyk	W/Sc Shashlyk
	backward, inner	$PbWO_4$	SciGlass		
	backward, outer	SciGlass	PbWO4	W powder/ScFi	W/Sc Shashlyk [c]
h-PID	barrel	High performance DIRC & dE/dx (TPC)	reuse of BABAR DIRC bars	fine resolution TOF	
	forward, high p	fluorocarbon gaseous RICH	double RICH combining aerogel and fluorocarbon	high pressure Ar RICH	
	forward, medium p	aerogel			
	forward, low p	TOF	dE/dx		
	backward	modular RICH (aerogel)			
e/h separation at low p	forward	TOF & areogel & gaseous RICH	adding TRD		
	backward	modular RICH & TRD	Hadron Blind Detector		
HCal	barrel	Fe/Sc	RPC/DHCAL	Pb/Sc	
	forward	Fe/Sc	RPC/DHCAL	Pb/Sc	
	backward	Fe/Sc	RPC/DHCAL	Pb/Sc	

[a] TPC surrounded by a micro-RWELL tracker
[b] set of coaxial cylindrical MICROMEGAS
[c] also Pb/Sc Shashlyk

Table 8.5: This matrix summarizes the high level performance of the different sub detectors. The interactive version of this matrix can be obtained through the Yellow Report Detector Working Group (https://physdiv.jlab.org/DetectorMatrix/).

η	θ	Nomenclature			Tracking						Electrons and Photons			π/K/p		HCAL		Muons
					Resolution	Relative Momentum	Allowed X/X_0	Minimum-pT	Transverse Pointing Res.	Longitudinal Pointing Res.	Resolution σ_E/E	PID	Min E Photon	p-Range (GeV/c)	Separation	Resolution σ_E/E	Energy	
< -4.6		↓ p/A	Far Backward Detectors	low-Q2 tagger														
-4.6 to -4.0						Not Accessible												
-4.0 to -3.5						Reduced Performance												
-3.5 to -3.0						σ_p/p ~0.2%×p⊕5%												
-3.0 to -2.5											1%/E ⊕ 2.5%/√E ⊕ 1%	π suppression up to 1:1E-4	20 MeV					
-2.5 to -2.0				Backward Detector				70-150 MeV/c (B=1.5 T)						≤ 10 GeV/c		50%/√E⊕10%		
-2.0 to -1.5						σ_p/p~ 0.04%×p⊕2%			dca(xy) ~ 40/pT μm ⊕ 10 μm	dca(z) ~ 100/pT μm ⊕ 20 μm	2%/E ⊕(4-8)%/√E ⊕ 2%	π suppression up to 1:(1E-3 - 1E-2)	50 MeV					Muons useful for bkg. improve resolution
-1.5 to -1.0																		
-1.0 to -0.5																		
-0.5 to 0.0			Central Detector															
0.0 to 0.5				Barrel		σ_p/p ~0.04%×p⊕1%	~5% or less X	200 MeV/c	dca(xy) ~ 30/pT μm ⊕ 5 μm	dca(z) ~ 30/pT μm ⊕ 5 μm	2%/E ⊕(12-14)%/√E ⊕ (2-3)%	π suppression up to 1:1E-2	100 MeV	≤ 6 GeV/c	≥ 3 σ	100%/√E+10%	~500MeV	
0.5 to 1.0																		
1.0 to 1.5																		
1.5 to 2.0				Forward Detectors		σ_p/p ~0.04%×p⊕2%		70 - 150 MeV/c (B = 1.5 T)	dca(xy) ~ 40/pT μm ⊕ 10 μm	dca(z) ~ 100/pT μm ⊕ 20 μm	2%/E ⊕ (4*-12)%/√E ⊕ 2%	3σ e/π up to 15 GeV/c	50 MeV	≤ 50 GeV/c		50%/√E+10%		
2.0 to 2.5																		
2.5 to 3.0						σ_p/p ~0.2%×p⊕5%												
3.0 to 3.5																		
3.5 to 4.0		↑ e		Instrumentation to separate charged particles from photons		Reduced Performance												
4.0 to 4.5						Not Accessible												
> 4.6			Far Forward Detectors	Proton Spectrometer														
				Zero Degree Neutral Detection														

8.4.3 Central Magnet Consideration

The EIC detector is built around a central solenoid magnet with optional correction trim coils required to meet the solenoid field specification. Tracking resolutions in the central pseudo-rapidity range suggest the nominal field of 1.5 T, but a range between 1.5 T and 3 T makes physics measurements accessible. A central field as high as 3 T is needed to maximize the effective $|B|\cdot$dl integral for particles scattered at small polar angles, both in forward and backward directions. High magnetic fields come at the cost of reducing the low-pT acceptance of charged tracks. The acceptance for low-pT particles down to the momenta $\sim$100 MeV/c requires that a fraction of physics data are taken at a substantially lower field. Field polarity flip is a standard measure to address systematic effects due to a different acceptance for the positively and negatively charged particles, hence a bipolar magnet operation with a polarity switch is one of the magnet requirements.

Physics studies available to date suggest a solenoid with a bore diameter 2.5-3.5 m in a traditional composition of an EIC detector. Specifications on coil length, presently assumed to be able to provide a $\sim$3.0 m magnetic length as a reference figure, cryostat radial space, and coil configuration require an optimization integrated with the overall detector design. The solenoid design is characterized by three regions, the barrel and backward endcap with the field parallel to the magnet axis and the RICH detector in the forward direction, which extends from +100 cm to +240 cm with respect to the magnet centre, where the field lines should be projective with respect to the nominal IP location. A flux return path could be provided through the hadronic calorimeter assemblies in the forward and backward directions. Correction coils in the hadron end-cap may be required to meet the RICH detector readout on field projectivity. The need for these coils should be avoided as they will adversely affect the hadron calorimeter performance, but if needed, should be allowed to occupy a maximum of 10 cm of the available linear space.

Alternative detector integrated designs, where a dipole or toroidal field are superimposed with the solenoid field in the central region of the detector, have been considered to improve the $|B|\cdot$dl integral at small scattering angles. These integrated designs could be an option if an acceptance that meets the physics requirements can be demonstrated.

Re-use of the existing BABAR/sPHENIX magnet is an alternative to the realization of a new solenoid with optimized design. Whereas the new solenoid main specifications are an up-to 3T magnetic field, a 2.5-3.5 m diameter bore, and a magnetic length of $\sim$3 m, the BABAR/sPHENIX magnet provides an up-to 1.5 T field, a 2.8 m diameter bore, and similar magnetic length. The magnet for the BABAR experiment at PEP-II at SLAC, CA was manufactured by Ansaldo, Italy in 1997 and was commissioned in 1998. It was then transferred to BNL, NY in 2015 for use in the sPHENIX experiment where it still resides today. It received a high-field test (up to 1.3 T) in 2018. The prolonged use of the BABAR/sPHENIX magnet requires the implementation of several maintenance and improvement modifications, including new protection circuits such as voltage taps, inspection of and as needed reinforcement of the internal mechanical support, including new strain gauges, and replacement of control instrumentation sensors. Several of these implementations involve the delicate operation of disassembly of the magnet. To repair an existing small leak in the

valve box for the cryogenic cooling system requires a replacement of the valve box or disassembly to inspect cooling pipework and to repair leaks. Moreover, additional changes are required for re-using the magnet, for example those needed to match the requirements of projective field lines in the RICH region.

The main parameters of both a new superconducting solenoid magnet, at the present stage of magnet optimization integrated with the overall detector design, and the existing BABAR/sPHENIX magnet are shown in Table 8.6. For a new magnet, a slightly larger bore of 3.2 meter is chosen as compromise between, on one hand, magnet complexity and mechanical Hall space considerations, and on the other hand providing some much-needed space in the bore to ensure more detector technology choices to ensure functionality of tracking, hermetic electromagnetic calorimetry and particle identification (both e/π and $\pi/K/p$) over a large range of particle momenta. The choice of NbTi conductor in a Cu matrix for the new magnet is driven by that for EIC no detection beyond hadronic calorimetry is foreseen beyond the bore, alleviating a material requirement on small radiation lengths and allowing use of Cu facilitating the magnet mechanical design.

The coil length is driven by the present definition of the barrel region as between pseudorapidity of -1 and 1. This corresponds to an angle of $\sim$40 degrees. This means that for a certain bore size, the space for the mechanical length of the magnet cryostat is roughly 20% larger, or 3.84 meter for a 3.2-meter bore. Folding in an approximate need of 12 cm additional need on each side of the magnet coil for inner vacuum and helium vessels, and multi-layer isolation, determines the coil length requirement to be 3.6 meter. A somewhat larger coil length of 3.8 meter would not be a major issue, but likely not much more as the edge of the cryostat is one of the regions where detector infrastructure (support, cabling, etc.) will reside, and deliberations between the need for equal coverage of tracking and electromagnetic calorimeter as trade-off with particle identification detector readout will occur.

Parameter	New Magnet	BABAR/sPHENIX Magnet
Maximum Central Field (T)	3	1.5
Coil length (mm)	3600	3512
Warm bore diameter (m)	3.2	2.8
Uniformity in tracking region (z = 0, r $<$ 80 cm) (%)	3	3
Conductor	NbTi in Cu Matrix	Al stabilized NbTi
Operating Temperature (K)	4.5	4.5

Table 8.6: Summary of some of the main requirements of the EIC detector solenoid magnet.

The main advantage of accessibility of low central solenoid fields (down to $\sim$0.5 T) is towards the low-PT acceptance of charged-particle tracks. A central field of 0.5 T roughly equates to a detection capability of charged particles down to transverse momenta of below $\sim$ 0.1 GeV/c. This is for example relevant for mapping the decay products of heavy-flavor mesons. The main advantage of a 3 T versus a 1.5 T central solenoid field is for

the momentum resolution of charged particles as function of pseudo-rapidity. Doubling the magnetic field can lead to a reduction of the momentum resolution by a factor of ≈2 from a leading order $\sim 1/B$ dependence. This is relevant in the central region, but even more so in the forward pseudo-rapidity regions, $\eta > 2$, where the momentum resolutions rapidly worsen. For example, for $\eta \sim 3$, a momentum resolution of ∼2-3% is achievable for pions with momenta up to about 30 GeV/c with a 3 T central field, and only double that resolution for a 1.5 T central field.

8.4.4 Detectors along the Beamline

Far-Forward Detectors

The measurement of exclusive and diffractive e+p and e+A events require careful design considerations for the Far-Forward ($\eta > 4.6$) region of the IR, as well as optimized placement of several detector subsystems, and careful choices of technology. In this section we will describe each detector subsystem in detail and present the physics reach demonstrated by the combined FF detector system.

The overall layout of the Far-Forward (FF) region is shown in Fig. 8.20, with a summary of the general acceptances of each current subsystem shown in Table 8.7.

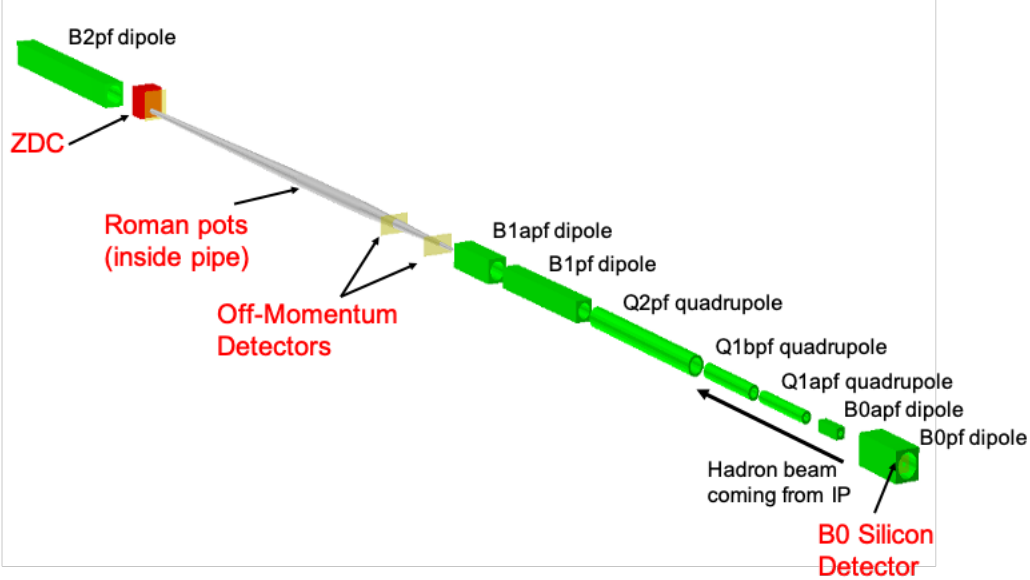

Figure 8.20: GEANT4 rendering of the far-forward hadron beam magnets and the four detector subsystems currently included.

The entire FF detector system consists (currently) of four main components: 1) the Roman Pots system, 2) the B0 spectrometer, 3) the off-momentum detectors, and 4) the zero-degree calorimeter. The main particles which are considered for detection in these subsystems are protons (in 1-3), neutrons (4), and photons (4 and potentially 2). In principle, nuclear

Detector	(x,z) Position [m]	θ [mrad]	Notes
ZDC	(0.96 m, 37.5 m)	θ <5.5	~4.0mrad at $\phi = \pi$
Roman Pots (2 stations)	(0.85, 26.0), (0.94, 28.0)	$0.0 < \theta < 5.5$	10σ cut.
Off-Momentum Detector	(0.8, 22.5), (0.85, 24.5)	$0.0 < \theta < 5.0$	$0.4 < x_L < 0.6$
B0 Spectrometer	(x = 0.19, $5.4 < z < 6.4$)	$5.5 < \theta < 13.0$	~20 mrad at ϕ=0

Table 8.7: Summary of far-forward detector locations and angular acceptances for protons, neutrons, and light nuclei or nuclear fragments. In some cases, the angular acceptance is not uniform in ϕ, as noted in the table.

fragments and charged pions could also be detected in the silicon sensors intended for protons, but PID would need to be considered in the case of proton/pion separation.

Roman Pots: The Roman Pots consist of two stations with anywhere from 2–5 sensor planes, with the stations spaced 2 m apart. The current straw-man design (see Fig. 8.21) assumes an L-shaped sensor with movement only in the y-direction, due to space considerations in the x-directions making additional movement in x challenging. Other designs are also under consideration to ensure maximal coverage of the acceptance.

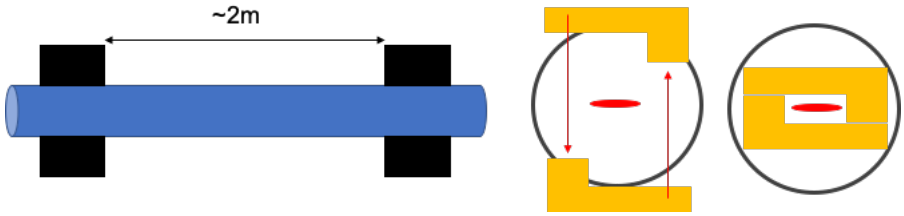

Figure 8.21: Straw-man sketch of a possible Roman Pots detector configuration allowing for only vertical movement, but covering both the horizontal and vertical acceptance. The sensors are situated in the beam pipe, a few centimeters from the beam and generally contained in an aluminum vessel known as a "pot" with a window for proton detection.

A new silicon technology using AC-coupled Low Gain Avalanche Diodes (AC-LGADs) is under consideration to be used to meet the requirements of the Roman Pots. The AC-LGADs provide both timing and spatial information for reconstruction. The Roman Pots system can accept charged particles with a scattering angle of $0.0 < \theta < 5.0$ mrad, and a longitudinal momentum fraction compared to the beam $0.8 < x_L < 1.0$. The lower bound of the angular acceptance is determined by the angular cutoff of the 10σ safe distance of the sensors from the beam, where $\sigma_{x,y}(z) = \sqrt{\beta_{x,y}(z)\epsilon_{x,y}}$ is the transverse size of the beam. This 10σ cut is dependent on both the beam energy, and the optics configuration (so-called "high acceptance" or "high divergence" configurations). Reconstruction of particle tracks is carried out using a linear transfer matrix which is used to calculate the IP coordinates from the local coordinate of the RP hits. This transfer matrix describes the particle transport through the magnetic lattice components from the IP to the RP location.

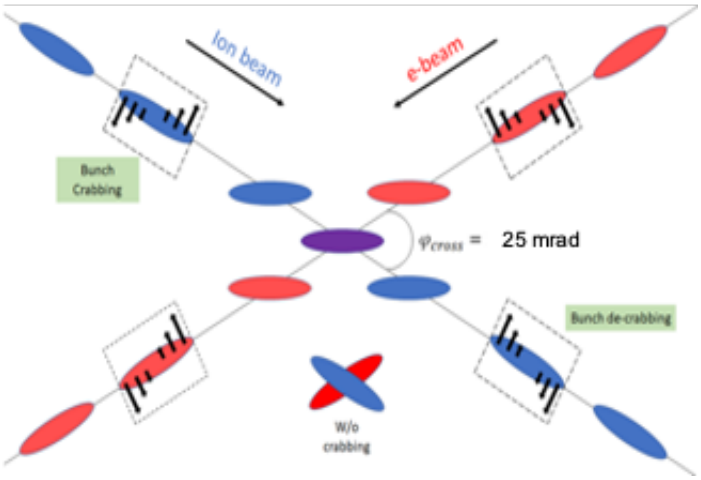

Figure 8.22: Cartoon sketch of the hadron and electron bunches rotated by the crab cavities with a 25 mrad crossing angle. The rotation of these bunches induces a vertex smearing with respect to the FF detectors. This can be removed with timing sufficient to isolate the collision vertex within the bunch.

The contributions to momentum smearing come from the following sources: 1) angular divergence, 2) vertex smearing due to the rotation of the bunch by the crab cavity, 3) finite detector pixel size, 4) beam momentum spread. In general, the angular divergence is the dominant source of momentum smearing, but can be reduced by a different choice of optics (e.g. high acceptance configuration) that will reduce the size of the beam (β-functions) at the Roman Pots location at the expense of reduced overall luminosity.

The contribution from the crab cavity rotation comes from the transverse momentum components imposed on the particles in the bunch by the cavity, with the goal of rotating the bunches such that they overlap at zero degrees at the IP, maximizing the luminosity (see Fig. 8.22). When the hadron bunch undergoes crab rotation (rotation in the x-z plane), the x-coordinate of the primary vertex is smeared by approximately half the crossing angle times the bunch length. Assuming a 25 mrad crossing angle with a 10 cm long bunch yields vertex smearing of 1.25 mm.

The crab cavity induced vertex smearing can be fully mitigated by the inclusion of timing $\sim$30–40 ps, which comes from the reduction of the effective bunch length to 1 cm (yielding a vertex smearing of 125 µm) divided by the speed of light. In addition to mitigating the smearing induced by crab cavity rotation, this fast timing will also be needed to reduce the background associated with high beam currents that will make the beam+machine and beam+gas backgrounds high enough to compete with the DIS rates in the detectors.

Finite pixel size induces smearing by providing uncertainty in the location of a particle hit left by a charged particle. This smearing is best balanced with reasonable channel count by using a (500 µm)$\times$(500 µm) pixel pitch. In order to reduce the potentially large number of required channels in the detector, novel silicon pad patterns (such as zig-zags) are being considered. The beam momentum spread has a negligible contribution to the

overall smearing. For the various beam energies + smearing contributions, the integrated p_T-smearing is 15-50 MeV/c. Figure 8.23 shows reconstruction of the momentum transfer, -t, for two different beam energies. Even with the 50 MeV/c total smearing in reconstructed p_T potentially present in the top beam energy configuration, the reconstruction is adequate for extracting a slope - needed for extraction of the impact parameter distribution related to the gluon GPD.

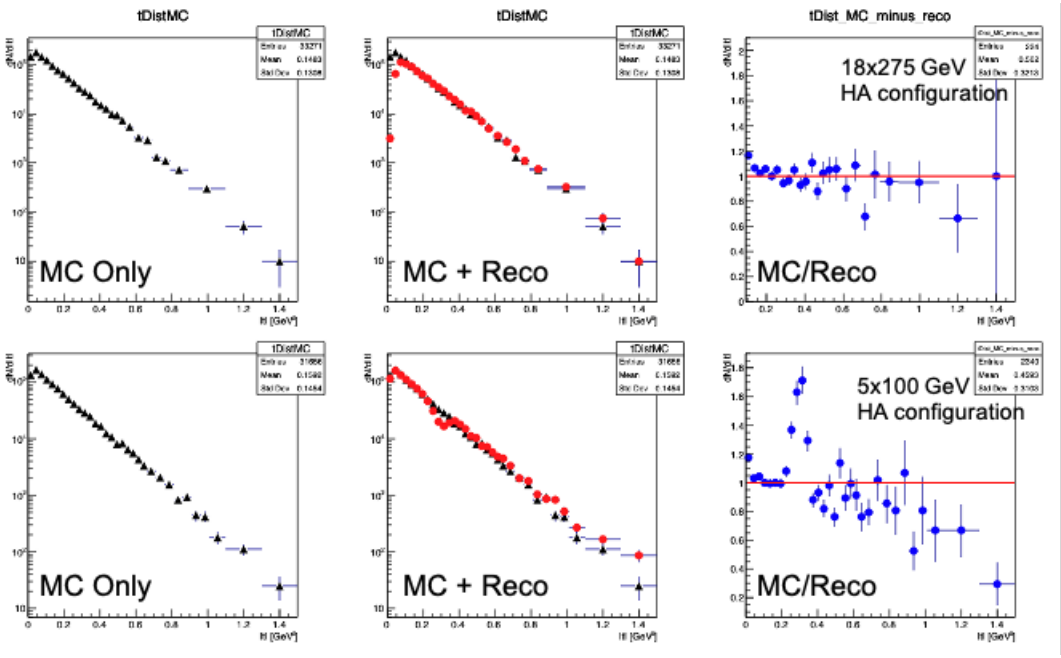

Figure 8.23: Momentum transfer, t, distributions for 18x275 GeV (top row) and 10x100 GeV (bottom row) DVCS events generated with MILOU. The first panel in both rows is the MC generated distribution, the middle panel is the MC (black) plotted with the reconstructed distribution (red), and the third panel is that ratio of the generated distribution over the reconstructed distribution. The acceptance gap between the RP and B0 detectors causes the peak at 0.38 GeV^2, while the residual slope at high-$|t|$ is caused by bin migration due to momentum smearing.

B0 Spectrometer: The B0 spectrometer consists of several planes of silicon placed inside the bore of the B0pf dipole magnet. A GEANT4 rendering of the subsystem is shown in Fig. 8.24.

The B0 spectrometer can in principle capture charged particles (or potentially photons if an ECAL is included) with scattering angle $5.5 < \theta < 20.0$ mrad, although on the side closest to the IP, the upper bound is closer to 13 mrad due to the electron quadrupole location with respect to the hadron beam pipe. Reconstruction of tracks with the B0 detector is done in the GEANT4 simulations using a conventional Kalman Filtering technique, and is therefore more sensitive to the choice of pixel pitch. This detector will require a minimum of (50 µm)×(50µm) pixels to achieve the necessary resolution. Access to this detector system will be challenging due to its location in the FF lattice, and the engineering considerations

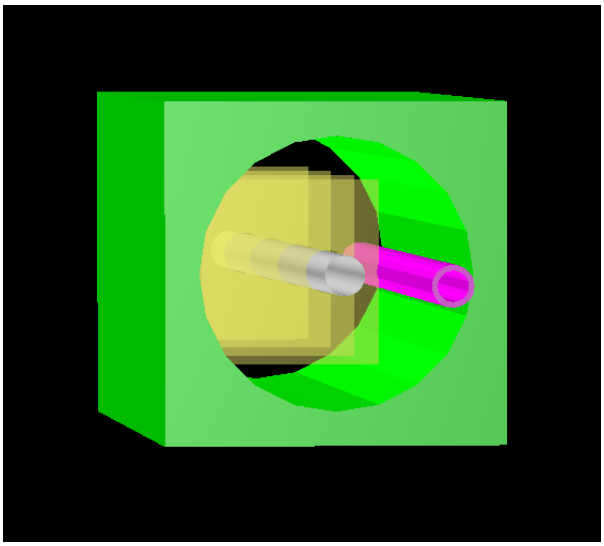

Figure 8.24: Closeup image of the B0 spectrometer rendered with GEANT4. The green block is the B0pf dipole magnet, the magenta cylinder is the electron quadrupole, the silver cylinder is the hadron beam pipe, and the yellow rectangles are the silicon active area.

are still under discussion.

Since the sensors will be in a warm portion of the bore, conventional silicon sensors can be employed, but fast (30–40 ps) timing will still be required to reduce smearing and background. A combination of MAPS sensors plus timing layers may be sufficient to supply the necessary spatial and temporal resolution. Additionally, the radiation load in the B0 spectrometer will likely be the highest of any of the FF detectors due to the proximity to the IP, and the amount of machine components which serve as secondary scattering centers for charged particles, which will be directed into the B0 detector.

Off-Momentum Detectors: The Off-Momentum Detectors (OMD) are silicon planes placed just after the B1apf dipole magnet and outside the beam pipe. The silicon sensors will be identical to those used for the Roman Pots subsystem, and have a similar acceptance for charged particles, but with a different range of longitudinal momentum fraction compared to the beam momentum x_L ($0.4 < x_L < 0.6$). This subsystem is required to measure charged particles from nuclear breakup events, where the final state hadrons have a much different rigidity than the nuclear beam, and therefore experience more bending in the dipole magnets, causing them to be deflected outside of the beam pipe before reaching the Roman Pots. Many of these nuclear breakup hadrons will also be captured in the B0 spectrometer, but with a larger scattering angle (> 5 mrad).

The OMD system will have overall better acceptance at small scattering angles (< 1 mrad) because these sensors will sit outside the beam pipe and will therefore require no 10σ cut for detector safety. Reconstruction using the normal transfer matrix approach invoked in the Roman Pots will potentially need to be refined due to the non-linear bending expe-

rienced in the quadrupole magnets for very off-momentum particles. This imposes additional smearing for especially low-x_L protons ($x_L < 0.3$). Solutions to this non-linear transport are under consideration.

Zero-Degree Calorimeter: As discussed in Sec. 2.1.2, a zero-degree calorimeter (ZDC) is required both for detection of neutrons in nuclear breakup events, and for veto of heavy-nuclear breakup events. Additionally, the inclusion of a preshower electromagnetic calorimeter will be required for detection of low-energy photons from nuclear excitation, or high-energy photons from forward π^0 decay. In order to achieve the required energy resolution for the hadronic calorimetric portion of the ZDC, a large transverse size (minimum 60 cm $\times$ 60 cm) and longitudinal length (minimum 1 m) will be required to contain the hadronic shower.

Current simulations assume a ZDC with $\frac{\sigma_E}{E} = \frac{50\%}{\sqrt{E}} \oplus 5\%$ and $\frac{\sigma_\theta}{\theta} = \frac{3 \text{ mrad}}{\sqrt{E}}$, but a better resolution may be required to reduce the smearing effects from this assumed resolution on observables. Currently the ALICE Forward Calorimeter (FoCal) [51] ZDC design is being considered as a starting point for the ZDC in the EIC IR, which makes use of tungsten silicon fibers for the hadronic section, and lead-tungstate crystals ($PbWO_4$) for the electromagnetic portion of the calorimeter.

Far Backward Detectors:

The path of the electron beam downstream of the interaction point is shown in Fig. 8.25. The horizontal axis is aligned with the direction of the beam at the collision point, along which photons from e+p and e+A interactions will travel. These photons come predominantly from the bremsstrahlung process used for luminosity determination. The lower left of the figure shows possible instrumentation for the luminosity measurement. Bremsstrahlung also produces electrons with momenta slightly below the beam energy. After being bent out of the beam by lattice dipoles they may be measured by taggers as shown in the top left of the figure.

Luminosity Measurement: The luminosity measurement provides the required normalization for all physics studies. At the broadest scale it determines absolute cross sections, such as needed for the structure function F_2 and derived PDFs. On an intermediate scale, it is also required to combine different running periods, such as runs with different beam energies needed to measure F_L, or runs with different beam species to study A dependencies. Asymmetry measurements are conducted using beams with bunches of both spin states. On the finest scale, the relative luminosity of the different bunch crossings is needed to normalize the event rates for the different states; the uncertainty on the relative bunch luminosity is a limiting factor for asymmetry measurements.

The bremsstrahlung process $e + p \longrightarrow e + p + \gamma$ was used successfully for the measurement of luminosity by the HERA collider experiments [42–44]. It has a precisely known

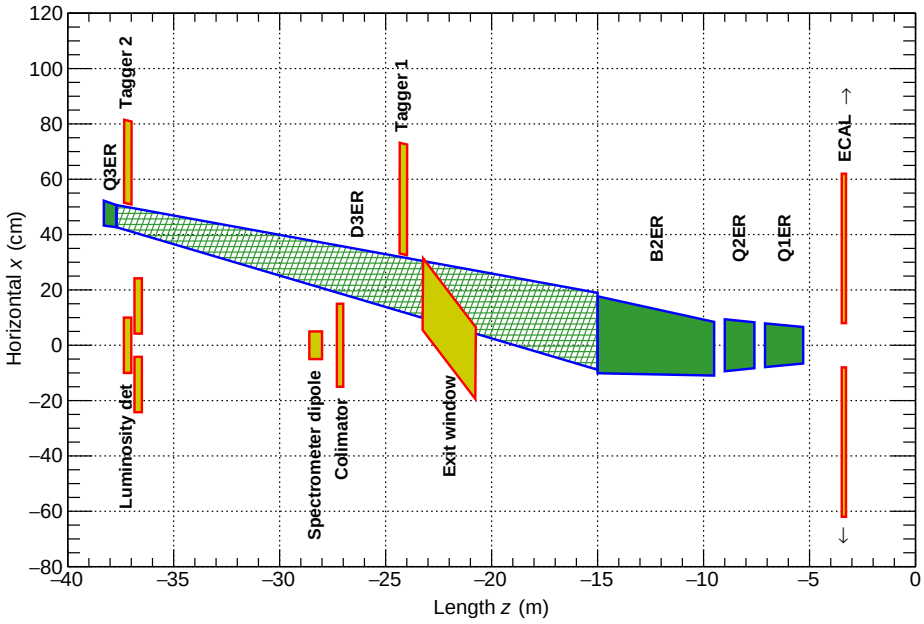

Figure 8.25: The region downstream of the interaction point in the electron direction.

QED cross-section which is large, minimizing theoretical uncertainty and providing negligible statistical uncertainty. Thus the scale uncertainty of the luminosity is determined by the systematic uncertainties of the counting of bremsstrahlung events. The ZEUS collaboration at HERA measured luminosity with a 1.7% scale uncertainty; further improvements at the EIC should be able to reduce this to <1% as required by the physics program.

In contrast to HERA, where only the electron beam was polarized, both the electron and proton/light ion beams will be polarized in the EIC. In this case the bremsstrahlung rate is sensitive to the polarization dependent term $a(P_e, P_h)$ in the cross section $\sigma_{\text{brems}} = \sigma_0(1 + a(P_e, P_h))$. Thus, the polarizations P_e, P_h and luminosity measurements are coupled, and the precision of the luminosity measurement is limited by the precision of the polarization measurement. This is especially important for relative luminosities for asymmetry measurements, where the bremsstrahlung process used for normalization has different cross sections for different spin states. The precision needed for the relative luminosity measurement is driven by the magnitude of the physics asymmetries which can be as low as 10^{-4}; the uncertainty on relative bunch luminosities must reach this level of precision.

The bremsstrahlung photon energy E_γ distributions for EIC beam energies are shown in the left of Fig. 8.26. They diverge as $E_g \to 0$ and have sharp cutoffs at the electron beam energies. As shown in the right of Fig. 8.26, the bremsstrahlung photons are strongly peaked in the forward direction with typical values of $\theta_\gamma \approx m_e/E_e$, with values of 20–60 µrad at the EIC. The RMS angular divergence of the electron beam is significantly larger than these values and will dominate the angular distribution of bremsstrahlung photons.

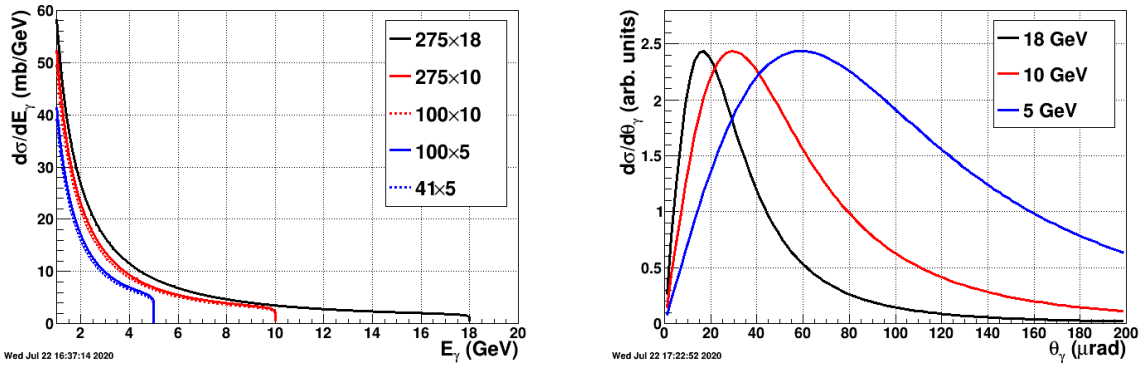

Figure 8.26: Bremsstrahlung photon energy (left) and angular (right) distributions for EIC beam energies.

Bremsstrahlung Photon Detectors: The straightforward method for measuring bremsstrahlung situates a calorimeter at zero degrees in the electron direction counting the resulting photons, as shown lower left of Fig. 8.25. The calorimeter is also exposed to the direct synchrotron radiation fan and must be shielded, thus degrading the energy resolution. This also imposes a rough low energy cutoff on photons typically ≈ 0.1–$1\,\mathrm{GeV}$ below which the calorimeter is insensitive. At peak HERA luminosities, the photon calorimeters were sensitive to 1-2 photons per HERA bunch crossing. At an EIC luminosity of $10^{33}\,\mathrm{cm}^{-2}\,\mathrm{s}^{-1}$, the mean number of such photons per bunch crossing is over 20 for electron-proton scattering and increases with Z^2 of the target for nuclear beams. The per bunch energy distributions are broad, with a mean proportional to the number of photons per bunch crossing. The counting of bremsstrahlung photons thus is effectively an energy measurement in the photon calorimeter with all of the related systematic uncertainties (e.g. gain stability) of such a measurement.

An alternative method to counting bremsstrahlung photons, used effectively by the ZEUS collaboration at HERA, employs a pair spectrometer. A small fraction of photons is converted into e^+e^- pairs in the vacuum chamber exit window. A dipole magnet splits the pairs vertically and each particle hits a separate calorimeter adjacent to the unconverted photon path. The relevant components are depicted in the lower left of Fig. 8.25. This has several advantages over a zero-degree photon calorimeter:

- The calorimeters are outside of the primary synchrotron radiation fan.
- The exit window conversion fraction reduces the overall rate.
- The spectrometer geometry imposes a low energy cutoff in the photon spectrum, which depends on the magnitude of the dipole field and the location of the calorimeters.

The variable parameters of the last two points (conversion fraction, dipole field and calorimeter locations) may be chosen to reduce the rate to less than or of order one e^+e^-

coincidence per bunch crossing even at nominal EIC luminosities. Thus, counting of bremsstrahlung photons is simply counting of e^+e^- coincidences in a pair spectrometer with only small corrections for pileup effects.

The locations of a zero-degree calorimeter and pair spectrometer are shown in the bottom left of Fig. 8.25. Careful integration into the machine lattice is required, not only to allow for enough space for the detectors, but also to accommodate the angular distribution of the photons. This is dominated by the angular divergence of the electron beam, with RMS values as high as 0.2 mrad. Thus a clear aperture up to a few mrad is required to measure the angular distribution and minimize the acceptance correction. The spectrometer rate is directly proportional to the fraction of photons which convert into e^+e^- pairs, placing stringent requirements on the photon exit window. It must have a precisely known material composition, and a precisely measured and uniform thickness along the photon direction.

Calorimeters are required for both luminosity devices, for triggering and energy measurements. The high rates dictate a radiation hard design, especially for the zero-degree calorimeter, which must also have shielding against synchrotron radiation. The spectrometer must also have precise position detectors to measure the $e^{\pm}$. Combined with the calorimeter energy measurement this allows reconstruction of the converted photon positions. The distribution of photon positions is required to correct for the lost photons falling outside the photon aperture and detector acceptances.

Bremsstrahlung and Low-Q^2 Electron Detectors: Downstream of the interaction point the electron beam is accompanied by a flux of electrons at small angles with respect to the beam direction and at slightly lower energy. They are predominantly final state electrons from the bremsstrahlung process $e + p \longrightarrow e + p + \gamma$, with an energy distribution the mirror image of the left of Fig. 8.26 with $E'_e = E_e - E_\gamma$. Also, a fraction of the electrons in this region are produced in quasi-real photoproduction with $Q^2 \approx 0$.

The final state bremsstrahlung electrons provide a powerful tool for calibrating and verifying the luminosity measurement with photons. Tagging bremsstrahlung electrons and counting corresponding photons in the photon detectors provides a direct measure of the luminosity detector acceptance in the tagged energy range. This is of paramount importance to precisely determine the pair conversion probability for the luminosity spectrometer, which depends on the exit window composition and thickness.

Tagging of low-Q^2 processes provides an extension of the kinematic range of DIS processes measured with electrons in the central detector. It crosses the transition from DIS to hadronic reactions with quasi-real photons. An example of acceptance as a function of Q^2 for measurements with the central detector and electron taggers as depicted in Fig. 8.25 is shown in Fig. 8.27. The electrons are generated by a simple model of quasi-real photoproduction [52] and Pythia. The taggers provide useful acceptance in the range $10^{-6} < Q^2 < 10^{-2}\,\mathrm{GeV}^2$. Application of the electron taggers for low-Q^2 physics will face a challenge from the high rate bremsstrahlung electrons, which can be addressed by tagger design and correlation with information from the central detector.

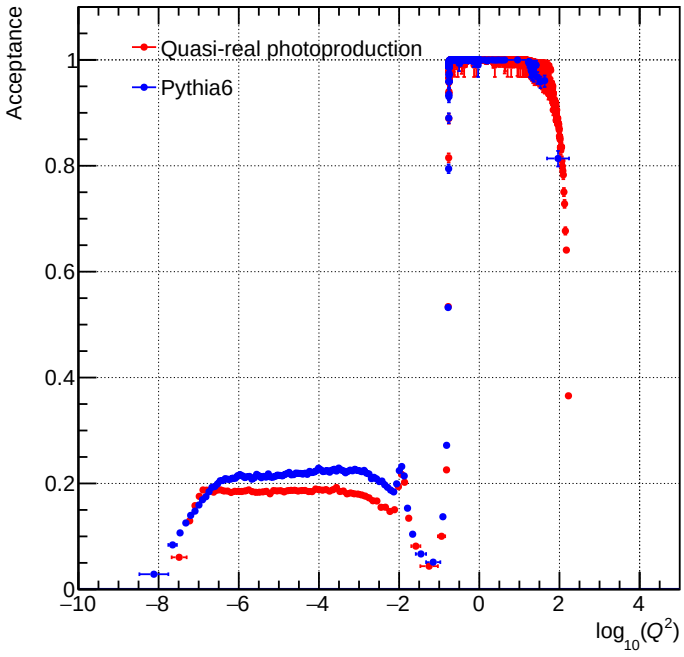

Figure 8.27: Acceptance as a function of Q^2 for electrons measured in the central detector (right plateau) and downstream taggers (left plateau). The electrons are generated by a simple model of quasi-real photoproduction and Pythia.

Possible locations of detectors for these electrons are shown in the top left of Fig. 8.25. Electrons with energies slightly below the beam are bent out of the beam by the first lattice dipole after the interaction point. The beam vacuum chamber must include exit windows for these electrons. The windows should be as thin as possible along the electron direction to minimize energy loss and multiple scattering before the detectors.

The taggers should include calorimeters for triggering and energy measurements. They should be finely segmented to disentangle the multiple electron hits per bunch crossing from the high rate bremsstrahlung process. The taggers should also have position sensitive detectors to measure the vertical and horizontal coordinates of electrons. The combined energy and position measurements allow reconstruction of the kinematic variable Q^2 and x_{BJ}. If the position detectors have multiple layers and are able to reconstruct the electron direction this will overconstrain the variable reconstruction and improve their measurement; this may also provide some measure of background rejection. The beam angular divergence will introduce significant errors on the variable reconstruction. The reconstructed versus generated Q^2 is shown in Fig. 8.28 with smearing from beam divergence. There is reasonable resolution for Q^2 as low as $10^{-3}\,\mathrm{GeV}^2$; below $10^{-4}\,\mathrm{GeV}^2$ meaningful reconstruction of Q^2 based on the electron is not possible.

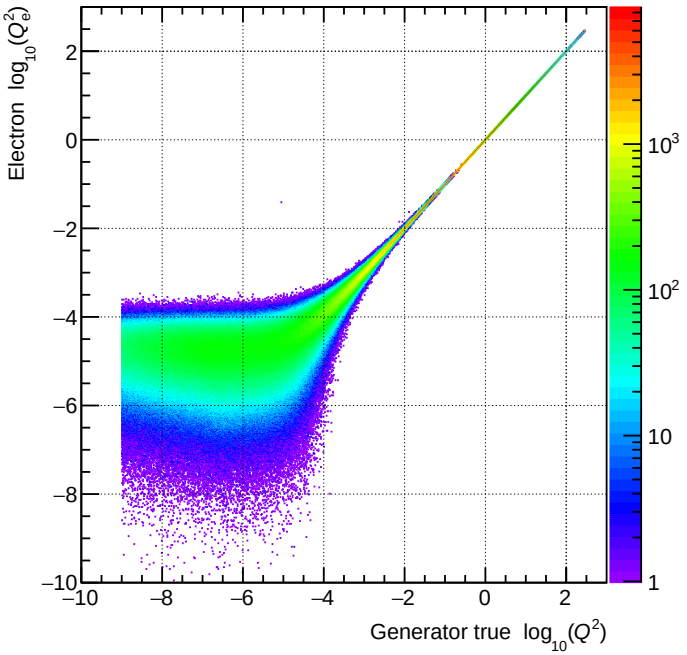

Figure 8.28: Comparison of reconstructed and reconstructed electron Q_e^2 with smearing for beam angular divergence.

8.4.5 Read-out electronics chain and data acquisition

Readout Electronics

As shown in Figure 8.29, the on-detector front-end boards (FEB) consist of Application Specific Integrated Circuits (ASIC) for signal processing. For some sub-detectors, the data digitized on FEBs can be transmitted to the DAQ system via fibers. For other sub-detectors, the analog or digital signals can be sent to an intermediate stage front-end processors (FEP); after pre-processing, data is transmitted to the DAQ system. The global timing system fans out system clock, synchronization, and configuration to FEBs and FEPs, to synchronize the whole system.

On the FEBs, ASICs will perform a series of processing tasks on the signals from the detector electrodes. For calorimeters, PID and various gaseous detectors, after the pre-amplifier and shaper, amplitude and fine timing information can be obtained by waveform digitizers, or discriminators and time-to-digital converters. The streaming readout architecture allows the signals to be continuously digitized and streamed out with or without a real-time trigger signal. For the candidate vertex tracker, Monolithic Active Pixel Sensors (MAPS), digital data processing will be integrated into the sensor, in order to process the position and hit count information. We expect that MAPS sensors will output high speed serial data streams to the back-end (relayed and multiplexed by FEPs and finally to the DAQ system). The detailed specifications of front-end ASICs will depend on the requirements of each sub-detector, for instance the dynamic range, detector capacitance,

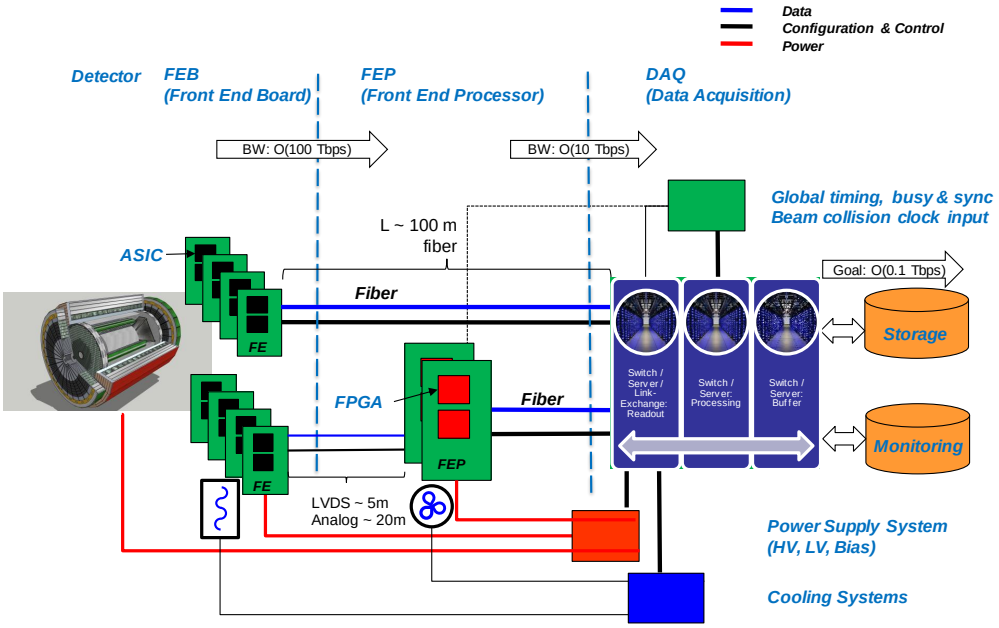

Figure 8.29: Diagram of the detector readout and DAQ system.

resolution, density and limit of power and cooling. These requirements will determine the gain, peaking time, buffer depth, dead time of the design, and the selection of CMOS technology. Most of the ASIC designs in use by current nuclear physics or high energy physics experiments are based on CMOS technology nodes between 65nm and 250nm.

From the FEBs, digital data from the ASICs can be sent out directly by electrical cable or optical fiber links. Analog signals can be sent out via cables to FEPs for further processing. The front-end ASICs may have integrated serializers, or use standalone serializer and deserializer ASICs for high speed data transmission. Radiation hardened optical links, for example the Versatile Link [53], can be used to convert electric to optical signals. For ASICs with slow digital outputs, devices such as GBT [54], LpGBT can be used to aggregate the data and transmit data at a higher speed, in order to reduce the quantity of fibers.

For the inner detectors, limitations due to available space, power, cooling and integration may prevent their FEBs from digitizing and output data via an optical link. In this case, the FEB output may have a limited range, 1-20 m, such as the case for the analog or LVDS signals. Then, the FEP boards are employed. The FEPs receive these signals from the FEBs, and transmit output data to the DAQ system after further data multiplexing and potential further processing. The main components on the FEPs are the on-board commercial off-the-shelf (COTS) Field Programmable Gate Arrays (FPGA). FPGA selection mainly de-

pends on the its available resources, including high-speed transceivers, differential pins and the logic resources for digital data processing. Standardization of inputs to the FEBs is not easy at an early stage of design; output from the FEBs may also be specific to the ASIC design. The aim is to use a common format (header, timestamp, etc.) for the data stream from the FEPs to the DAQ system. The Printed Circuit Board (PCB) design, fabrication and assembly will be in compliance with standards defined by IPC (Industry Association for Printed Circuit Board and Electronics Manufacturing).

High precision timing distribution is important to synchronize all the front-ends including the FEBs and FEPs. The clock and control commands can be fanned out from the timing system directly to the front-end, or via the custom part of DAQ system, by using the reverse path of the detector data readout. The latest FPGAs support adjusting the phase of clock and data at a resolution of a few picoseconds, which is enough to reduce and compensate for the skew of the timing distribution system. The readout electronics will work together with the DAQ system, handling flow control and busy on and off control and while also meeting the latency and buffering requirements.

The high channel density and power dissipation within the detector volume will require consideration of cooling systems, both liquid and forced convection, as an integral part of the detector package design. We propose to employ readily available equipment (COTS) to support cooling, high voltage, low voltage and bias distribution and these already include the appropriate control infrastructure. Our grounding and shielding plan is based on the use of these COTS equipment, which support floating supplies with grounding referenced at the detector clean ground grid. We also propose to follow the National Electrical Code (NEC) safety standards for wiring and cabling and the FCC standards for minimizing Electro-Magnetic Interference (EMI) to reduce overall noise and maintain good signal integrity.

Data Acquisition System

The data stream from FEB and FEP will be transmitted to the back-end via fibers. We envision a free-streaming DAQ with links going to the DAQ system directly. The DAQ system will mainly consist of COTS components, for instance servers with CPU, GPU or FPGA accelerator cards supporting strong computing capability, high bandwidth network with switches and network-interface-cards (NIC), and devices for permanent data storage. Both Ethernet and Infiniband are under development towards a terabit per second level of speed. For the EIC, existing technology with 25-100G bandwidth are expected to be sufficient.

Depending on the detailed design of the FEPs, and if supporting network interfaces, the fibers can go to the switches of the DAQ system directly. To design a common and robust DAQ system for all the front-ends, a common first stage can be developed in the DAQ system. A PCIe based framework, for example, such as FELIX [55], as the first stage of the DAQ system can be a commercial server with custom or commercial PCIe cards. These cards support interfacing the FEBs, FEPs, and global timing system directly. It can receive

clock, control, trigger and configuration commands from the timing system, and fan them out to the FEBs and FEPs via fibers. On the reverse direction, it receives data via dedicated optical links and buffering, and monitoring information from the FEBs and FEPs. It will also support handling busy and flow control. The detector data can be processed in the main components FPGAs, or be sent to the network switches through the PCIe bus and COTS NIC cards. Besides PCIe, other technologies can also be used to transfer data to the network switches, for example the 100GbE RDMA over Converged Ethernet, implemented in FPGA with external DDR modules or internal high bandwidth memory (HBM).

As discussed in Section 8.3, the total data rate is still uncertain and evolves with the detector and machine designs. Therefore, in the case of unexpected high background, we envision risk mitigation with possible additional background and noise filtering at the DAQ. One well-established technique is to throttle the detector data stream with calorimeter based trigger signals either in the DAQ FPGA or in the memory of the servers. With advanced real-time algorithms, we envision excessive noise can also be suppressed with signal feature extraction algorithms such as clustering and tracklet building.

Online Computing

If we compare the needs of the EIC with the High Luminosity run of the LHC we see quite striking differences; HL-LHC is planned for a peak luminosity of 7.5×10^{34} cm^{-2} s^{-1}, i.e. 7.5 times larger than the peak luminosity of EIC of 10^{34} cm^{-2} s^{-1}. The p+p cross section at 14 TeV is 1000 times larger than the e+p cross section at the EIC, and the average number of charged hadrons produced in p+p (about 70) is larger by a factor of 10 as compared to e+p.

In order to cope with this the LHC experiments, targeting the study of low cross section reactions, have agreed to limit their collection rate to 10 kHz. Nonetheless the very high hadronic cross section ($\sim$ 80 mb) sided by the high luminosity result in a pile-up of 200 events coming together with the triggered interesting event, a factor of 20 compare to LHC Run2. Present reconstruction time for p+p data is, e.g. for ATLAS [56], 1300HS06 s, or about 100 s at present cores with 13.1 HS06. In 10 years we expect the reconstruction time going down by a factor 10, but while event sizes at the HL-LHC will increase linearly with the pile-up, the reconstruction time will scale exponentially with respect to LHC in Run2.

EIC will collect events at a maximum rate of 500 kHz, 50 times larger than HL-LHC, corresponding to the full 30-60 μb cross section as estimated in Table 8.3. Pile-up will not be an issue since for a 1000 times smaller cross section and a factor 10 smaller rates the probability to have a pileup event is around 1%. Nevertheless we expect higher machine background from electrons, as compared to p+p accelerators, an aspect which will have high value in the design of the interaction regions at the EIC as discussed in Section 8.3.

With the machine design not yet frozen, and the detector under development, at the present stage we may only estimate upper bounds for the computing needs on the experiment at the EIC, by using some reasonable assumptions. If we assume as upper bound a 10^{-3} occupancy for the vertex part of the detector, dominated by machine background,

and 1% for the rest of the apparatus (5×10^5 Hz times 2×10^8 pixels times 10^{-3} detector occupancy times 4 Bytes address of the hit pixel, with the contribution of the rest of the detector of about 5%) the data flow from the detector will be about 400 GB/s, with an event size of 0.8 MB. Please note this is a conservative estimation assuming vast majority data are background and noise, and the data from the EIC collision signal is only a modest portion of this data flow estimation discussed in Figure 8.5. Nonetheless this estimated flow is within present capabilities.

8.5 Offline Software and Computing

This section will describe the computing needs for the reference detector at the EIC and discuss the foreseen software developments.

Aside from possible contribution of machine backgrounds, the reconstruction of events at the EIC will be easier than the same task at present LHC or RHIC hadron machines, and, in perspective, much easier than for the high luminosity LHC (HL-LHC), which will start operating two years earlier than the EIC, when we may expect a gain in performance for CPUs of about a factor of 10 with respect to now.

Reconstruction time of DIS events at presently running experiments is around 0.35 s (or $\sim$ 5HS06 s) both at COMPASS and at CLAS12, with event sizes of 0.03 MB and 0.02 MB respectively. Filtering out machine background with high efficiency will allow to keep the reconstruction time at 5HS06 s also in 2030. Processing events at the same speed of acquisition, or 500 000 events per second, on today nodes will therefore require 200 000 cores or 1500 nodes, a computing farm well in the size of the EIC project. The expected gain in CPU power in the next 10 years, as well as the possible improvement in the reconstruction software from the use of machine learning techniques give a considerable margin to cope with higher event complexity that may come by higher backgrounds rates.

Software design and development will constitute an important ingredient for the future success of the experimental program at the EIC. Moreover, the cost of the IT related components, from software development to storage systems and to distributed complex e-Infrastructures can be raised considerably if a proper understanding and planning is not taken into account from the beginning in the design of the experiment itself.

A growing group dedicated to this effort already exists. An important step in the clustering of a core group focusing on computational aspects at an EIC has been the approval by the EIC Generic R&D program of the eRD20 proposal, creating in 2016 the EIC Software Consortium or ESC. ESC has been the backbone to form in 2018 the Software Working Group within the EICUG. The Software Working Group has supported the Yellow Report initiative and provided the tools for simulations and helped in the creation of the infrastructure for storage and documentation.

The Software Working Group is starting in parallel a greenfield development that will focus on different aspects of future needs:

- Simulations for detector optimization, to cover the more immediate needs of the design and integration of the various sub detectors
- Help in the development of state of the art Monte Carlo event generators for the full spectrum of EIC physics. Validation of these generator will be possible by using data from running experiments.
- Development of a full simulation-reconstruction chain allowing to benchmark the performances of the reconstruction software.
- Development of modern "event reconstruction" schemes both using standard approaches but also exploring novel methods based on artificial intelligence machine learning techniques.

The reconstruction software will have to cope with the streaming read-out scheme adopted and will be design to match the chosen solution.

Software tools: While developing the software for simulation and reconstruction of events from a detector which will be up and running in 2030, we need to inquire ourselves about the long term perspective of software used in today HEP experiments and evaluate different options. Leaving aside for the moment both full purpose or dedicated Monte Carlo Event Generator discussed in a separate section, this means that we have to decide on: how to describe the detector; which program to use for particle transportation/interaction; reconstruction tools and the data model.

The choice of LHC experiments for the Run4 and after may guide us in this task.

DD4hep [57] is a toolkit for detector description developed within the AIDA2020 EU program (Advanced European Infrastructures for Detectors at Accelerators). It can be an interesting option for the EIC since recently the CMS collaboration announced that it plans to use it to provide the structure of the experiment to all their data processing applications.

It is worth considering it for the EIC since it is designed to answer a very common need of experiments, i.e. the development of a coherent set of software tools for the description of high-energy physics detectors from a single source of information. Detector description in general includes not only the geometry and the materials used in the apparatus, but all parameters describing, e.g., the detection techniques, constants required by alignment and calibration, description of the readout structures, conditions data and more.

Given it use withing CMS choice, it is expected that DD4hep will be supported over the entire experiment life-time.

DD4hep reuses existing software components, combines the functionalities and thus optimizes the flexibility, minimizing the efforts required by users to leverage the benefits. Reused components include elements of the ROOT geometry package [58] and the GEANT4 simulation toolkit [59].

GEANT4 [59] is the baseline for detector simulation on all LHC experiment and is a natural choice for the EIC. We have developed strong connections with the core developer team

of GEANT4 and the improvements in physic list and in non standard geometries which may be needed for the EIC are being discussed with them. About one year ago, the core team of the Software Working Group organized together with the GEANT4 Collaboration a Technical Forum on the EIC. The Forum allowed to discuss both the information on recent updates on GEANT4, but also the physics list for the EIC as maintained by the EIC Software Consortium. The requested improvements on photo-nuclear and electro-nuclear reactions were included in GEANT4version 10.6, and this is under test right now. The study of vectorizing this transportation, as done withing the GEANT4, the vector transport R&D collaboration [60] will offer interesting improving options for GEANT4 itself and we will follow this activity closely.

ROOT [58] is by nowadays standards a fundamental ingredient of virtually all HEP workflows, being used for data persistency, modeling, graphics, and analysis. It is structured to have excellent, active connections with the experiments including, at least for LHC, direct investment by the experiments. The developing team is investing in future developments for HL-LHC, and is also assuming interesting approaches to machine learning tools. It pushes in fact the HEP community to not develop its own machine learning tools but, maybe in a more efficient way, to collaborate with other sciences on improving and growing tool-sets. For that they offer a Toolkit for Multi Variate Analysis TMVA to bridge between ROOT and external machine learning tools such as scikit-learn, XGBoost, TensorFlow, Keras, mxnet, or PyTorch.

ACTS [61] (A Common Tracking Software) is an experiment-independent toolkit for (charged) particle track reconstruction in (high energy) physics experiments, implemented in modern , with 2017 standards. It is being developed for the HL-LHC, but is also targeting sPHENIX. Adopts a highly-templated design allowing to avoid virtual lookup, and it is agnostic of detectors and magnetic fields for high portability. Another important aspects with respect to development is the designed rigorous unit tests, an essential aspect for the future EIC software. All these characteristics made this software an interesting option worth evaluation for the reconstruction software for the EIC reference detector.

Many others codes are under evaluation, like GENFIT [62], a generic track-fitting toolkit, GAUDI [63, 64], a software architecture and framework for building HEP data processing applications, JANA2 [65], a multi-threaded event reconstruction and others.

Finally, following the large worldwide spread, we are moving to the use of tools facilitating collaborative analysis and logbook as presently done at CERN with SWAN [66], as a Service for Web-based ANalysis, built upon the widely-used Jupyter notebooks.

Simulations for detector optimization: The tools developed for the Yellow Report initiative will be expanded and used for extensive full simulations of the reference detector. This is a short term goal for software developers in order to support with detailed simulation studies the finalization of the reference detector, thus allowing to move from the CDR stage toward the full technical design.

Monte Carlo event generators for the EIC: The EIC Software Working Group, and before the eRD20 Software Consortium have initiated a project with the Monte Carlo communities in the US and Europe (MCnet) to work on MCEGs for the EIC, requiring MCEG

for polarized e+p, , and ^{3}He as well as e+A measurements. The MCEG initiative is connecting the MCEG efforts in NP and HEP and is encouraging a strong interplay between experiment and theory already at an early stage of the EIC. As an initial step, we have started a workshop series on âœMCEGs for future e+p and e+A facilitiesâ[U+009D] where the third workshop was held in November 2019 at the Erwin Schrödinger International Institute for Mathematics and Physics in Vienna, Austria. During the workshop, we reviewed the theory for physics with light and heavy ions and discussed the modifications needed on the general-purpose MCEGs to simulate unpolarized observables also for e+A where a precise treatment of the nucleus and its breakup is needed. There were presentations about pioneering MCEG projects for e+A (BeAGLE, spectator tagging in , Sartre), as well as on the ongoing development of the e+A adaptation of JETSCAPE and the Mueller dipole formalism in Pythia8. We also summarized the status of MCEG-data comparisons in HZTool/Rivet that are critical to tune MCEGs to existing DIS and heavy ion data as well on the ongoing work of verifying MCEGs for TMDs with TMD theory/phenomenology. Our current focus is on benchmarks and validation. We are working with the EICUG on benchmark MC productions and the validation of MC results. This will facilitate the adaption of modern MCEGs that have been so far only used by the LHC community.

As a recent development, the DIRE authors [67,68] introduced radiative effects in the simulation of the DIS. This is an important step, since a full multidimensional analysis will be needed in the study of TMDs and GPDs, given the dependence of the cross section over many kinematic variables. From the experimental point of view, and without entering to much in detail of the analysis, this means that detectors and RC effects will have to be accounted together at simulation level in order to derive matrices transforming from raw counts in the detector to Born cross sections.

The DIRE parton showers is a modern MCEG, usable as a extension of the general purpose event generation frameworks PYTHIA, and will be included as an option from the 8.3 release. This will allow to check the prediction of the Monte Carlo both using the data of running DIS experiments (at JLab and COMPASS at CERN) and with the outcome of the simulation of DJANGO [69,70], the reference tool for the study of RC effects at HERA.

The use of Artificial Intelligence and Machine Learning techniques:

In the world of computing there is growing excitement for what is perceived as the revolution of the new millennium: artificial intelligence (AI). In particular the R&D program of the future EIC could be one of the first programs systematically exploiting AI.

AI is becoming ubiquitous in nuclear physics [71]. According to a standard taxonomy [72], AI encompasses all the concepts related to the integration of human intelligence into machines; a subset of AI is machine learning (ML), which is usually grouped into supervised, unsupervised and reinforcement learning; deep learning (DL) is a particular subset of ML based on deep (*i.e.*, made by many hidden layers) neural networks, which is often considered the evolution of ML since it typically outperforms other methods when there is a large amount of data and features, provided sufficient computing resources. In the most frequent applications in our field, features are selected and a model is trained for classification or regression using signal and background examples.

Experimental particle and nuclear physics is big data [73]: the gigantic data volumes produced in modern experiments are typically handled with "triggers"—a combination of dedicated hardware and software—to decide near-real-time which data to keep for analysis and which to toss out. In this respect, AI plays already an important role in experiments like LHCb [74], where machine learning algorithms (see, *e.g.*, topological trigger and ghost probability requirements) make almost 70% of these decisions, from triggers to higher level analysis of reconstructed data.

Supported by modern electronics able to continuously convert the analog detector signals, new approaches like Streaming Readout [75] could further the convergence of online and offline analysis: the incorporation of high level AI algorithms in the analysis pipeline can lead to better data quality control during data taking and shorter analysis cycles. Recently the Fast Machine Learning workshop [76] highlighted emerging methods and scientific applications for DL and inference acceleration, with emphasis on ultrafast on-detector inference and real-time systems, hardware platforms, co-processor technologies, and distributed learning. In this context, AI (used here in a broader sense to embrace different approaches) could foster in the next years significant advances in areas like anomaly detection (see, *e.g.*, [77]) and fast calibration/alignment of detectors.

For tracking detectors, particle tracking is always a computationally challenging step. Several approaches have been developed recently for tracking based on deep learning [78], but there are still open questions about the best way to incorporate such techniques. The problem in Nuclear Physics experiments is typically different, being characterized by most of the computing cycles spent in propagating the particles through inhomogeneous magnetic fields and material maps. Here AI can contribute to determine the optimal initial track parameters allowing to decrease the number of iterations needed by Kalman-Filter.

As for particle identification and event classification, we have witnessed in the last years a growth of applications based on machine learning both for global particle identification (see, *e.g.*, [79]) as well as custom novel solutions which combine different architectures for specific detectors (see, *e.g.*, [80] for imaging Cherenkov detectors).

The search for rare signatures in large acceptance detectors at high intensities necessitates advanced techniques to filter those events. The GlueX experiment at Jefferson Lab for example is searching for exotic hadrons and demonstrated the utility of machine learning techniques based on BDTs [81] to achieve the required performance in filtering events with rare reactions [82].

The utilization of jets at the future EIC can be beneficial for a variety of fundamental topics [83], including the gluon Wigner distribution, the gluon Sivers function, the (un)polarized hadronic structure of the photon, the (un)polarized quark and gluon PDFs at moderate to high momentum fraction (x) as well as studies of hadronization and cold nuclear matter properties. Machine Learning is having a major impact in jet physics, empowering powerful taggers for boosted jets as well as flavor tagging, and various deep learning applications like recursive neural network which leverage an analogy to natural language processing [84] have been developed. ML4Jets [85] is a series of workshop dedicated to these topics.

Another area where AI can significantly contribute is that of fast simulations. Simulating the detector response of large scale experiments like EIC is typically slow and requires immense computing power. One of the most computationally expensive step in the simulation pipeline of a typical experiment is the detailed modeling of the high multiplicity physics processes characterizing the evolution of particle showers inside calorimeters. AI, could speed up simulations and potentially complement the traditional approaches. Recent advances with generative networks (see, *e.g.*, GAN, VAE, Flow-based models [86–88]) look as a compelling alternative to standard methods with orders of magnitude increase in simulation speed [89] but so far usually at the cost of reduced accuracy.

Detector design is another fundamental area of research for EIC. Advanced detector design often implies performing computationally intensive simulations as part of the design optimization process. One of the conclusions from the DOE Town Halls on AI for Science on 2019 [90] was that "*AI techniques that can optimize the design of complex, large-scale experiments have the potential to revolutionize the way experimental nuclear physics is currently done*". There are at present various AI-based optimization strategies based on, *e.g.*, reinforcement learning or evolutionary algorithm [91, 92]. Among these, Bayesian Optimization (BO) [93, 94] has gained popularity for its ability of performing global optimization of black-box functions that are expensive to evaluate and that can be in addition noisy and non-differentiable. It consists in a surrogate modelling technique where the regression is typically done through Gaussian processes or decision trees depending on the dimensions of the problem, and a cheap acquisition function is used to suggest which design points to query next, overall minimizing the number of evaluations.

Recently, an automated, highly-parallelized, and self-consistent procedure has been developed [95] and tested for the dual-radiator Ring Imaging Cherenkov (dRICH) design, which has been considered as a case study. These studies not only showed a statistically significant improvement in performance compared to the existing baseline design but they also provided hints on the relevance of different features of the detector for the overall performance. This procedure can be applied to any detector R&D, provided that realistic simulations are available. One example is the optimization of detector materials, e.g. the optimization of large size aerogel composites for aerogel-based detectors in [96].

Beyond individual subdetectors AI can be also used to efficiently optimize the design of different sub-detectors combined together, taking into account mechanical and geometrical constraints. An interesting approach consists in a multi-objective optimization (see, *e.g.*, [97–99]), which allows to encode the performance of the detectors as well as other aspects like costs in the design process, to determine the Pareto front [100]. Currently ongoing activities within the EIC R&D program which are leveraging AI for optimization include the EM/Hadronic Calorimetry, *e.g.*, optimizing the glass/crystal material selection in "shared rapidity regions" for best performance of the EM calorimeter. Even more, AI has the ability to optimize the collection of all subdetectors of a large detector system, using more efficiently the figures of merit we use to evaluate the performance that drive the detector design. Remarkably, the design optimization of multiple subdetectors operating together has not been explored yet. This is a high dimensional combinatorial problem that can be solved with AI.

This is undoubtedly a strategic moment to discuss how to fully take advantage of the new opportunities offered by AI to advance research, design and operation of the future EIC. The interest of the community has been evidenced by the number of contributions and attendance of workshops dedicated to AI in Nuclear Physics, e.g. at the [71, 101], and the 2021 AI4EIC-exp workshop [102], which bring together the communities directly using AI technologies and provide a venue for discussion and identifying the specific needs and priorities for EIC.

8.6 Lepton and Hadron Polarimetry

Rapid, precise beam polarization measurements will be crucial for meeting the goals of the EIC physics program as the uncertainty in the polarization propagates directly into the uncertainty for relevant observables (asymmetries, etc.). In addition, polarimetry will play an important role in facilitating the setup of the accelerator.

The basic requirements for beam polarimetry are:

- Non-destructive with minimal impact on the beam lifetime
- Systematic uncertainty on the order $\frac{dP}{P} = 1\%$ or better
- Capable of measuring the beam polarization for each bunch in the ring - in particular, the statistical uncertainty of the measurement for a given bunch should be comparable to the systematic uncertainty
- Rapid, quasi-online analysis in order to provide timely feedback for accelerator setup

8.6.1 Electron Polarimetry

The most commonly used technique for measuring electron beam polarization in rings and colliders is Compton polarimetry, in which the polarized electrons scatter from 100% circularly polarized laser photons. The asymmetry from this reaction is measured via the scattered electrons or high energy backscattered photons. A brief review and description of several previous Compton polarimeters can be found in [103]. A particular advantage of Compton polarimetry is that it sensitive to both longitudinal and transverse polarization.

The longitudinal analyzing power depends only on the backscattered photon energy and is given by,

$$A_{\text{long}} = \frac{2\pi r_o^2 a}{(d\sigma/d\rho)}(1-\rho(1+a))\left[1-\frac{1}{(1-\rho(1-a))^2}\right], \tag{8.1}$$

where r_o is the classical electron radius, $a = (1+4\gamma E_{\text{laser}}/m_e)^{-1}$ (with the Lorentz factor $\gamma = E_e/m_e$), ρ is the backscattered photon energy divided by its kinematic maximum, E_γ/E_γ^{max}, and $d\sigma/d\rho$ is the unpolarized Compton cross section. In contrast, the transverse

analyzing power depends both on the backscattered photon energy and the azimuthal angle (ϕ) of the photon (with respect to the transverse polarization direction);

$$A_{\text{tran}} = \frac{2\pi r_o^2 a}{(d\sigma/d\rho)} \cos\phi \left[\rho(1-a) \frac{\sqrt{4a\rho(1-\rho)}}{(1-\rho(1-a))} \right]. \tag{8.2}$$

This azimuthal dependence of the asymmetry results in an "up-down" asymmetry (assuming vertically polarized electrons) and requires a detector with spatial sensitivity.

Plans for electron polarimetry at EIC include a Compton polarimeter at IP 12, where the electron beam is primarily vertically polarized. A Compton polarimeter near the primary detector in the vicinity of IP 6, where the beam will be a mix of longitudinal and transverse polarization, is also under investigation; since that region of the ring is extremely crowded, care must be taken in the assessment of whether a polarimeter can be accommodated. A schematic of the placement of the Compton polarimeter at IP 12 is shown in Fig. 8.30.

Nominal electron beam parameters at IP 12 are provided in Table 8.8. Of particular note is the relatively short bunch lifetime at 18 GeV. Table 8.9 shows the average transverse analyzing power, luminosity, and time required to make a 1% (statistics) measurement of the beam polarization for an individual bunch, assuming a single Compton-scattered event per crossing. The constraint of having a single event per crossing is related to the need to make a position sensitive measurement at the photon and electron detectors. Note that even with this constraint, the measurement times are relatively short and, in particular, shorter than the bunch lifetime in the ring.

Table 8.8: Beam parameters at IP12 for the EIC nominal electron beam energies.

Parameter	5 GeV	10 GeV	18 GeV
Bunch frequency [MHz]	99	99	24.75
Beam size (x) [µm]	390	470	434
Beam size (y) [µm]	390	250	332
Pulse width (RMS) [ps]	63.3	63.3	30
Intensity (avg.) [A]	2.5	2.5	0.227
Bunch lifetime [min]	>30	>30	6

Table 8.9: Asymmetries, measurement times needed for a 1% statistical measurement for one bunch and needed luminosities for three different beam energies for a 532 nm laser.

E_{beam} [GeV]	σ_{unpol} [barn]	$\langle A_\gamma \rangle$	t_γ[s]	$\langle A_e \rangle$	t_e[s]	L[1/(barn·s)]
5	0.569	0.031	184	0.029	210	1.37E+05
10	0.503	0.051	68	0.050	72	1.55E+05
18	0.432	0.072	34	0.075	31	1.81E+05

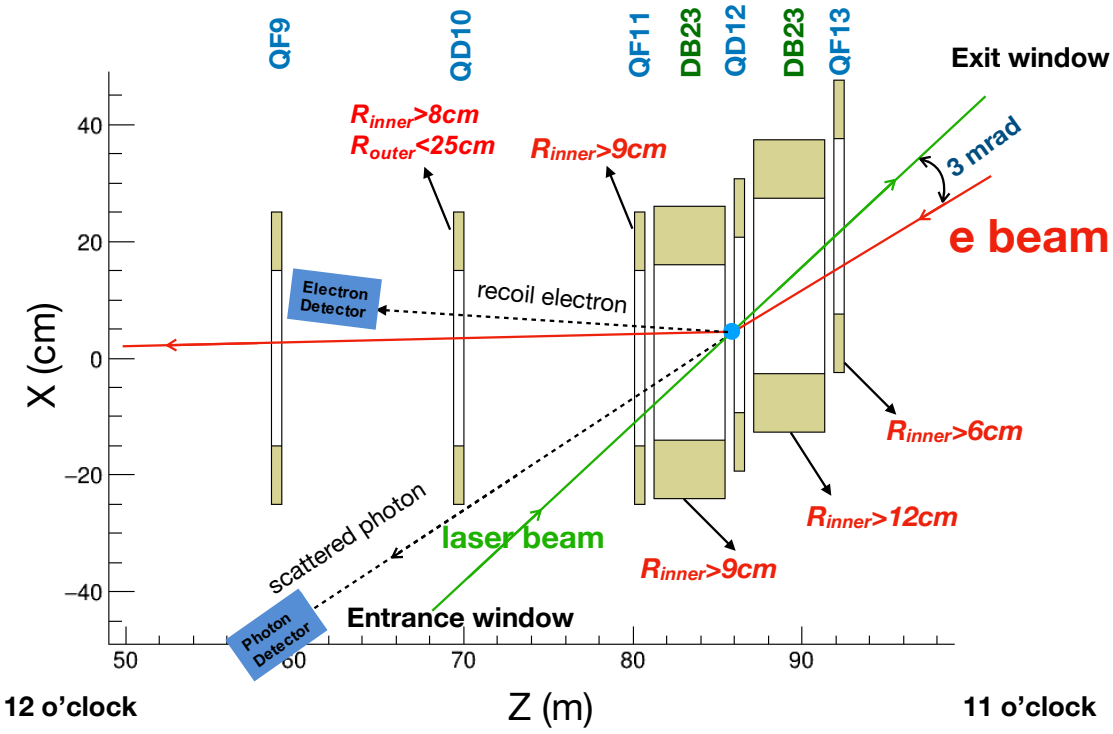

Figure 8.30: Layout of the Compton polarimeter at IP 12. In this figure the electron beam travels from right to left - the laser beam collides with the electrons just downstream of QD12. The dipole just downstream of the collision (DB12) steers the unscattered electrons allowing detection of the backscattered photons about 25 m downstream of the collision. DB12 also momentum-analyzes the scattered electrons, facilitating use of a position sensitive electron detector downstream of QD10. Also noted in the figure are constraints on required apertures of the magnets needed to allow transport of the laser beam, backscattered photons, and scattered electrons.

Even for a single electron bunch (circulating through the ring at a frequency of ≈75 kHz), the luminosities provided in Table 8.9 can be readily achieved using a single-pass, pulsed laser. Since the electron beam frequency varies with energy, it would be useful to have a laser with variable pulse frequency. A laser system based on the gain-switched diode lasers used in the injector at TJNAF [104] would provide both the power and flexible pulse frequency desired. Such a system would make use of a gain-switched diode laser at 1064 nm, amplified to high average power (10-20 W) via a fiber amplifier, and then frequency doubled to 532 nm using a PPLN or LBO crystal. The repetition rate is set by the applied RF frequency to the gain-switched seed laser.

The detector requirements for the EIC Compton polarimeters are dictated by the requirement to measure the transverse and longitudinal polarization simultaneously. For longitudinal polarization, this means the detectors will require sensitivity to the backscattered

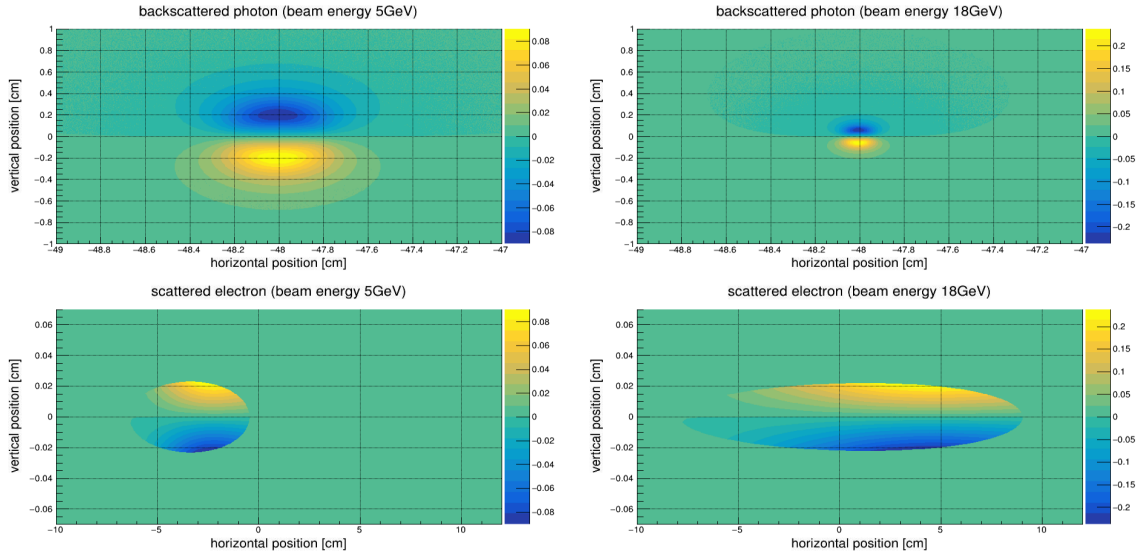

Figure 8.31: Compton (transverse) analyzing power at the nominal photon and electron detector positions for the IP 12 polarimeter.

photon and scattered electron energy. The photon detector can make use of a fast calorimeter, while the electron detector can take advantage of the dispersion introduced by the dipole after the collision point to infer the scattered electron energy from a detector with position sensitivity in the horizontal direction.

To measure transverse polarization, position sensitive detectors are required to measure the up-down asymmetry. This is particularly challenging given the very small backscattered photon cone at the highest EIC beam energy. At HERA, the vertical position of the backscattered photon was inferred via shower-sharing between the optically isolated segments of a calorimeter [105]. Calibration of the non-linear transformation between the true vertical position and the energy-asymmetry in the calorimeter was a significant source of uncertainty. The proposed detector for the EIC Compton will measure the vertical position directly via segmented strip detectors, avoiding the calibration issues faced at HERA.

The transverse Compton analyzing power vs. position at the detector for the backscattered photons and scattered electrons at 5 and 18],GeV is shown in Fig. 8.31. The backscattered photon cone will be largest at the lowest energy (5 GeV) - this will determine the required size of the detector. The distribution at 18],GeV, where the cone is the smallest, sets the requirements for the detector segmentation. Note that the scattered electrons are significantly more focused than the photons. Monte Carlo studies indicate that the transverse polarization can be reliably extracted at 18 GeV with a vertical detector segmentation of 100 µm for the photon detector and 25 µm for the electron detector. The detector size should be at least $16 \times 16\,\mathrm{mm}^2$ for the photons and $10\,\mathrm{cm} \times 1\,\mathrm{mm}$ for the scattered electrons. The horizontal segmentation for the electron detector can be much more coarse due to the large horizontal dispersion introduced by the dipole.

Diamond strip detectors are a feasible solution for both the photon and electron detectors.

Diamond detectors are extremely radiation hard and are fast enough to have response times sufficient to resolve the minimum bunch spacing (10 ns) at EIC. Tests of CVD diamond with specialized electronics have shown pulse widths on the order of 8 ns [106]. For the photon detector, about 1 radiation length of lead will be placed in front of the strip detectors to convert the backscattered photons. As an alternative to diamond detectors, HVMAPS detectors are also under consideration. The radiation hardness and time response of HVMAPS will need to be assessed to determine their suitability for this application.

As noted earlier, the photon detector will also require a calorimeter to be sensitive to longitudinal components of the electron polarization. Only modest energy resolution is needed; radiation hardness and time response are more important requirements for this detector - a tungsten powder/scintillating fiber calorimeter would meet these requirements.

Backgrounds are an important consideration for Compton polarimetry as well. The primary processes of interest are Bremsstrahlung and synchrotron radiation. Monte Carlo studies have shown that the contribution from Bremsstrahlung should be small for a beamline vacuum of 10^{-9} Torr. Synchrotron radiation, on the other hand, will be a significant concern. Careful design of the exit window for the backscattered photons will be required to mitigate backgrounds due to synchrotron. The electron detector is not in the direct synchrotron fan, but significant power can be deposited in the detector from one-bounce photons. This can be mitigated by incorporating tips or a special antechamber in the beampipe between the Compton IP and the detector [107]. The electron detector will also be subject to power deposited in the planned Roman Pot housing due to the beam Wakefield. Preliminary simulations indicate the Wakefield power should not be large enough to cause problems, but this will need to be considered in the detailed Roman Pot design.

In addition to measurements in the EIC electron ring, it is important to determine the electron beam polarization in or just after the Rapid Cycling Synchrotron (RCS) in order to facilitate machine setup and troubleshoot possible issues with the electron beam polarization. In the RCS, electron bunches of approximately 10 nC are accelerated from 400 MeV to the nominal beam energy (5, 10, or 18 GeV) in about 100 ms. These bunches are then injected into the EIC electron ring at 1 Hz. The short amount of time each bunch spends in the RCS, combined with the large changes in energy (and hence polarimeter analyzing power and/or acceptance) make non-invasive polarization measurements, in which the the RCS operates in a mode completely transparent to beam operations, essentially impossible. However, there are at least two options for making intermittent, invasive polarization measurements.

The first, and perhaps simplest from a polarimetry perspective, would be to operate the RCS in a so-called "flat-top" mode [108]. In this case, an electron bunch in the RCS is accelerated to its full or some intermediate energy, and then stored in the RCS at that energy while a polarization measurement is made. In this scenario, a Compton polarimeter similar to that described above could be installed in one of the straight sections of the RCS. The measurement times would be equivalent to those noted in Table 8.9 (since those are for a single stored bunch), i.e., on the order of a few minutes.

Another option would be to make polarization measurements in the transfer line from the RCS to the EIC electron ring. In this case, one could only make polarization measurements averaged over several bunches. In addition, the measurement would be much more time consuming due to the low average beam current ($\approx$ 10 nA) since the 10 nC bunches are extracted at 1 Hz.

The measurement time at 10 nA using a Compton polarimeter similar to the one planned for IP12 would take on the order many days. The IP12 Compton limits the number of interactions to an average of one per crossing to count and resolve the position of the backscattered photons. A position sensitive detector that could be operated in integrating mode, would allow more rapid measurements. However, the required position resolution (25-100 µm) would be very challenging for a detector operating in integrating mode.

An alternative to Compton polarimetry would be the use of Møller polarimetry. Møller polarimeters can be used to measure both longitudinal and transverse polarization and can make measurements quickly at relatively low currents. The longitudinal and transverse Møller analyzing powers are given by,

$$A_{ZZ} = -\frac{\sin^2\theta^*(7+\cos^2\theta^*)}{(3+\cos^2\theta^*)^2}, \tag{8.3}$$

$$A_{XX} = -\frac{\sin^4\theta^*}{(3+\cos^2\theta^*)^2}, \tag{8.4}$$

where A_{ZZ} is the analyzing power for longitudinally polarized beam and target electrons, A_{XX} for horizontally polarized beam and target electrons, and θ^* is the center-of-mass scattering angle. Note that $A_{YY} = -A_{XX}$. The magnitude of the analyzing power is maximized in both cases at $\theta^* = 90$ degrees, where $|A_{ZZ}| = 7/9$ and $|A_{XX}| = 1/9$.

Extrapolating from typical measurement times from the Møller polarimeters at TJNAF (which provide a statistical precision of 1% for the longitudinal polarization in about 15 minutes for a 1 µA beam on a 4 µm iron target), we estimate that a 10% measurement could be made in about 1.5 hours in the RCS to EIC transfer line. This could perhaps be shorter depending the maximum foil thickness that could be used as the polarimeter target.

A key drawback of Møller polarimetry is that the solid foil targets are destructive to the beam, so cannot be carried out at the same time as normal beam operations. An additional complication is the requirement for a magneto-optical system to steer the Møller electrons to a detector system. In the experimental Hall A at Jefferson Lab, the Møller spectrometer employs several quadrupoles of modest length and aperture, combined with a dipole to deflect the Møller electrons into the detector system. The whole system occupies about 7 m of space along the beamline, but the space used by the quadrupoles can also be used for beam transport during normal operations (i.e., when Møller measurements are not underway).

The preferred choice for polarimetry at the RCS is a Compton polarimeter in the RCS ring, with measurements taking place during "flat-top" mode operation. However, if this "flat-

top" mode is not practical, then a Møller polarimeter in the RCS transfer line could serve as a reasonable fallback, albeit with reduced precision and a larger impact on the beamline design.

8.6.2 Hadron Polarimetry

Hadron polarimetry has been successfully performed on RHIC polarized proton beams for nearly two decades. Through continual development a systematic uncertainty $< 1.5\%$ was achieved for the most recent RHIC polarized proton run. As the only hadron polarimeter system at a high energy collider it is the natural starting point for hadron polarimetry at the EIC.

Hadron polarization is typically measured via a transverse single spin left right asymmetry: $\epsilon = A_N P$. Unlike for polarized leptons, the proportionality constant is not precisely known from theory. The solution at RHIC employs an absolute polarimeter with a polarized atomic hydrogen jet target (Hjet), illustrated in Fig. 8.32. The hydrogen polarization vector is alternated between vertically up and down. The RHIC beam also has bunches with up and down polarization states. By averaging over the beam states the asymmetry with respect to the target polarization may be measured, and vice versa:

$$\epsilon_{\text{target}} = A_N P_{\text{target}} \quad \epsilon_{\text{beam}} = A_N P_{\text{beam}} \,. \tag{8.5}$$

The target polarization is precisely measured with a Breit-Rabi polarimeter. Combined with the measured asymmetries the beam polarization is determined:

$$P_{\text{beam}} = \frac{\epsilon_{\text{beam}}}{\epsilon_{\text{target}}} P_{\text{target}} \,. \tag{8.6}$$

The absolute polarization measurement is independent of the details of A_N.

The diffuse nature of the polarized jet target provides only a low rate of interactions, resulting in a measurement limited to a statistical precision of 5-8% per RHIC fill; it is not sensitive to the inevitable decay of beam polarization throughout a fill. Also, the jet target is wider than the beam and measures only the average polarization across the beam. The beam polarization is larger at the center than the edges transversely; the polarization of colliding beams differs from the average polarization due to this effect [109]. The polarimeters must measure this transverse polarization profile to provide correct polarizations for use by collider experiments.

At RHIC the required finer grained polarization details are provided by the proton-carbon (pC) relative polarimeter, illustrated in Fig. 8.33. A thin carbon ribbon target is passed across the beam and scattered carbon nuclei are measured in detectors arrayed around the beam. The dense target provides a high interaction rate, allowing an asymmetry measurement with a few per cent statistical precision in less than 30 seconds. Such measurements are made periodically throughout a RHIC fill, providing a measurement of the beam polarization decay. The ribbon target is narrower than the beam; thus it is able to measure

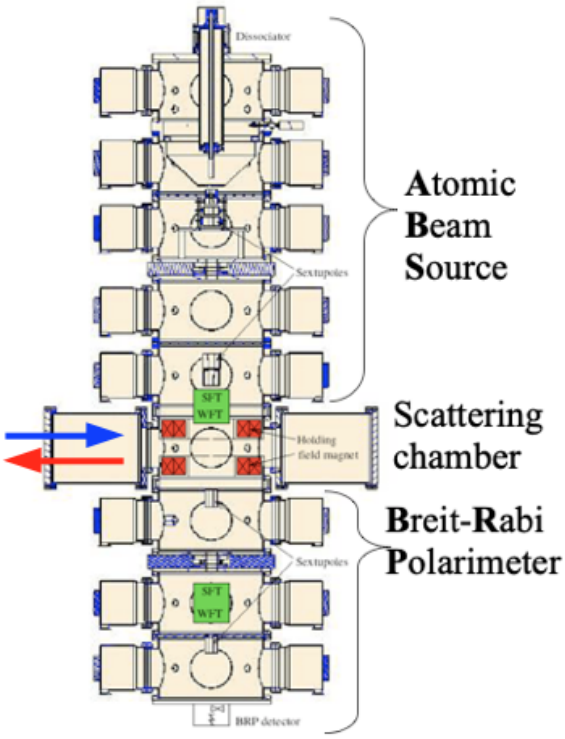

Figure 8.32: The RHIC polarized hydrogen jet polarimeter. The atomic beam source at the top passes polarized hydrogen across the beams (blue and read arrows) in the scattering chamber, with detectors left and right of the beams. The atomic hydrogen polarization is measured by the Breit-Rabi polarimeter at bottom.

asymmetry as a function of position across the beam and determine the transverse polarization profile. The absolute polarization scale of the pC polarimeter is set by normalizing an ensemble of pC measurements to the results from the Hjet polarimeter for the corresponding RHIC fills.

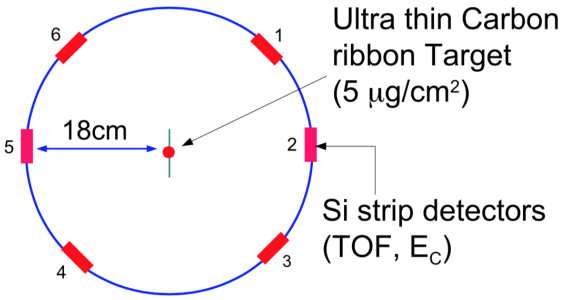

Figure 8.33: Cross section of the RHIC proton-carbon polarimeter. A thin carbon ribbon target is passed across the beam (into page) and scattered carbon nuclei are measured in the six detectors.

Both of the RHIC hadron polarimeters can in principle be used for proton polarimetry at

the EIC. At present two significant difficulties are foreseen. First, backgrounds in both polarimeters are observed and lie partially beneath the signal events. They are distinguished by timing distributions different from the signal allowing separation or estimation of a subtraction from the signal. At the EIC with higher bunch crossing frequency, the backgrounds will lie under the signal events from adjacent bunches and separation or subtraction based on timing will not be possible. Studies are under way to determine the nature of the background and possibly find a rejection method. Second, materials analysis of the carbon ribbon targets indicates that the higher proton beam currents and bunch crossing frequencies at the EIC will induce heating to temperatures causing the targets to break after only a few seconds in the beam. A search for alternative target materials has been initiated.

A possible alternative to the pC polarimeter has been proposed. It is based on the observation by the PHENIX collaboration of a large azimuthal asymmetry of forward neutrons in the proton direction in p+Au collisions [110]. This effect is well described by a process of the high Z Au nucleus emitting a photon, which produces neutrons off of the polarized proton [111]. A polarimeter based on this process would replace the Au beam with a high Z fixed target as a source of photons; a Xe gas jet may be a suitable target. Such a polarimeter could be tested at RHIC in the final years of operation.

For light ion polarimetry at the EIC, it may be possible to replace the hydrogen jet target with polarized light ions. Tagging of breakup of target or beam nuclei will be necessary to isolate the elastic scattering signal required for an absolute polarization measurement. The pC polarimeter, or an alternative, developed for protons at the EIC should also provide suitable relative polarimetry for light ions.

The main polarimeters may be situated anywhere in the EIC hadron ring. The Hjet and pC polarimeters each require 1-2 m space along and transverse to the beam. However, one relative polarimeter (pC or alternative) should be placed near the experimental interaction point between the hadron spin rotators. The hadron polarimeters are only sensitive to transverse spin polarization. During longitudinal spin runs asymmetry measurements near the interaction point are required to verify that the transverse component of the spin direction is zero.

8.7 Installation and Maintenance

8.7.1 Infrastructure

The baseline EIC configuration currently includes one fully instrumented Interaction Region (IR) and one general purpose physics detector. For the purposes of this document, it is assumed that the detector will be located in IP-6 (the STAR Hall), and that the available infrastructure will either be re-used or will serve as a reference for the future EIC installation. Complementary information about IP-8 (the PHENIX Hall) is given where appropriate.

Hall infrastructure

In addition to the beam line area (the Wide Angle Hall), RHIC complex 1006 has an Assembly Building with adequate floor space for detector maintenance work, as well as a control room, counting house, office space, electronic/mechanical workshops, gas shed, online computing room and other service areas, as shown in Fig. 8.34.

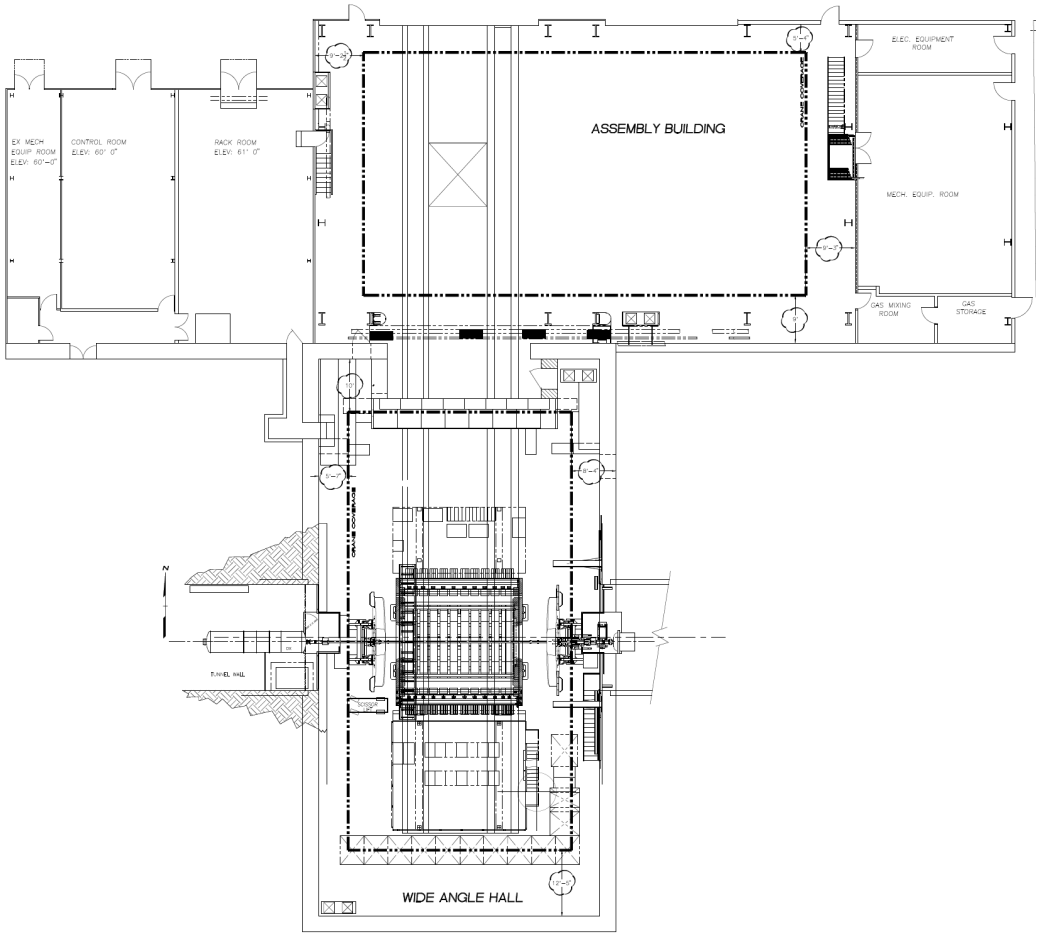

Figure 8.34: RHIC IP6 experimental area layout. STAR detector shown schematically in the beam position.

The general specifications for the IP6 and IP8 experimental halls are provided in Tab. 8.10.

The coordinate system of the EIC experiment is oriented as follows. The z-axis is along the beamline toward the outgoing hadron direction, the y-axis points upward, and the x-axis points toward the EIC-accelerator center.

Detector subsystem infrastructure requirements include cooling (HVAC, CW, LCW), power (clean, utility, generator-backed), cryogenics, cabling, service lines, and gas system specifications for gaseous detectors. These requirements cannot be specifically identified

Table 8.10: IP6 and IP8 experimental hall dimensions and related data. Hall width goes parallel to the beam line in this table, see also the Wide Angle Hall boundaries in Fig. 8.34.

	IP6	IP8
Hall length and width	3200 cm x 1615 cm	1737 cm x 1859 cm
Distance from floor to beam line	432 cm	523 cm
Door dimensions (W x H)	823 cm x 823 cm	927 cm x 1017 cm
Floor load capacity	5000 psi	4000 psi
Crane capacity	20 ton	12 ton

at this stage of planning, but will be developed by the Detector Working Groups for a subset of the EIC detector technologies on the time scale of the Yellow Report. The new requirements will be reported in the next revision of this document, along with a table containing the existing capacities available in the RHIC IP-6 Hall. The following is a list of items which needs to be considered during integration:

- *electronics racks and data cables* The bulk of the electronics cables and service lines for the sub-detectors will be routed through gaps which exist between the barrel and endcap regions. As a result, the installation design for these cables must accommodate the removal/repositioning of the endcaps.
- *Power distribution and grounding*
- *Cooling and gas installation*
- *Cryogenic capacity*
- *Pressure and temperature control of the experimental hall*
- *Shielding against the penetrating particles from the machine*

Safety and Environmental Protection

For the purpose of this document, it is assumed that the experimental hall's safety systems (sprinklers, ODH monitors, smoke alarm) are provided as part of the RHIC infrastructure. The design and operation of EIC sub-detector components will follow BNL safety regulation rules.

- *Radiation control*
- *Interlock system*
- *Hazardous materials and systems* (flammable gases, lasers, cryogenic fluids, electric shock hazard, magnetic forces, beam line vacuum, etc.)

8.7.2 Installation

At this time, the composition of the EIC central detector is not defined to a level of detail that is sufficient to provide a step-by-step installation procedure. However, the overall detector layout, as well as several boundary conditions, are sufficiently understood to make the following assertions:

- In order to maximize the luminosity, the beam line final focusing quads have to be brought as close to the IP as possible. Current Interaction Region design leaves only about 9 m of space for the main physics detector, with the accelerator beam line elements installed adjacent to this area. It is assumed that these elements (quads on the incoming hadron side and B0 magnet on the incoming electron side) are not supposed to be moved for the central detector installation and maintenance.
- The general purpose EIC detector with a 4π coverage in tracking, calorimetry and PID will almost certainly use all of the available space, up to the last centimeter.
- A fully assembled $\sim$9 m long detector will not pass through the 823 cm wide door, connecting the assembly and the installation areas. Unless the door is made wider as part of the civil construction work, it is therefore assumed that at least one of the calorimetry endcaps has to be rolled into the beam line area separately, on its own carriage.
- There is not enough space in the installation area for either assembly or maintenance during the long shutdown periods, see Figure 8.34. Consequently, as much of the pre-assembly work as possible should happen in the assembly hall.

Although the following considerations do not represent hard constraints, they will impact system design and operation:

- In order to maximize luminosity, the beam line final focusing quads must be positioned as close to the IP as possible. The current Interaction Region design provides approximately 9 meters of space for the main physics detector, with accelerator beam line elements installed in the adjacent areas. It is assumed that these elements (quads on the incoming hadron side and B0 magnet on the incoming electron side) WILL NOT be moved for installation or maintenance of the central detector.
- Having 4π coverage in tracking, calorimetry and PID, the general purpose EIC detector is likely to consume 100% of the available space.
- The door connecting the assembly area and the installation area is 823 cm wide. Accordingly, the fully assembled, $\sim$9 meter long detector cannot be moved intact between the two areas without making structural modifications. To accommodate this, it is assumed that one or more of the calorimetry endcaps will be placed on independent carriages that allow them to be separated from the main detector before moving.

- The space in the installation area is not sufficient to perform any significant assembly or maintenance on the central detector (see Fig.8.34). Consequently, the bulk of assembly and maintenance must be performed in the assembly hall.

- The solenoid cryostat chimney must be designed such that it does not need to be disconnected whenever the detector is relocated from the installation area to the assembly area, and vice versa. The current expectation is that the cryo-can will be mounted to the interior wall of the assembly area and will be connected to solenoid using a flexible cryogenic line. This line will be sufficiently long to remain connected to the solenoid when the central detector is in either room.

- In order to minimize the amount of silicon detector cabling in the electron endcap acceptance, the pre-assembled silicon tracker modules must be inserted into their nominal position from the hadron endcap side, with all cabling attached and routed through the "service gap" between the barrel and the hadron endcaps. This operation cannot be performed with the high-momentum gaseous RICH detector already installed in the hadron endcap, since it will block access to the central area. Additionally, due to space constraints along the beamline, the $\sim$1.5 meter long RICH modules cannot easily be installed into the central detector in the beam position. A possible solution is to pre-assemble the entire central part of the main detector (the barrel, the silicon forward / vertex / backward tracker, and all of the endcap acceptance equipment except for the calorimetry), together with the central piece of the beam pipe, in the assembly area.

This set of constraints and supporting considerations provides the foundation for the detector "building block" composition and the installation sequence, described below. A general purpose EIC detector, schematically shown in Figure 8.35, will be used as a reference. Figure 8.36 shows a perspective view of the EIC detector.

As illustrated in these figures, the detector can be naturally subdivided into three parts: the central barrel, which is built around the solenoid magnet yoke, and the two endcaps.

The endcap hadronic calorimeters are expected to be of an Fe/Sc sandwich type, with the magnetic structural steel used as an absorber. By design, they will be self-supporting, serve as a solenoid flux return, and will be able to provide mechanical support to other subsystems. To optimize construction, as well as the access strategy, it may be beneficial to locate not only the hadronic, but also the electromagnetic calorimetry in the endcap assemblies, as shown in Figure 8.39 for the hadronic calorimetry. This will certainly be true for the hadron endcap should a spaghetti W/SciFi e/m calorimeter technology be used in a configuration with the photo-sensor electronics installed on the upstream end of the towers. In that case, the hadronic and e/m calorimeter assemblies will likely be physically connected to one another face-to-face, with the barrel hadronic calorimeter to hadron endcap split then also needing to be aligned with the front of the e/m calorimeter. Once the endcap halves are rolled out, one will have access to both the e/m calorimetry front end electronics, and to the electronics and services of a substantial fraction of the central (barrel) part of the detector.

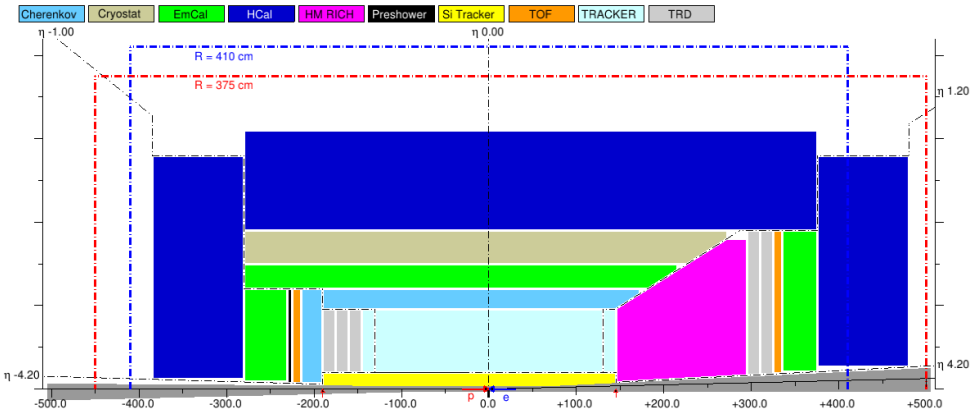

Figure 8.35: A 2D sketch of an EIC detector layout, horizontal cross cut. Only one half of the detector is shown, with the other half being mirror-symmetric in this view, up to the crossing angle. Beam pipe footprint (in dark gray) is to scale. Blue dashed line shows the doorway size between the assembly and the installation halls. Red dashed line shows the realistic central detector envelope with the available [-4.5 ... 5.0] m space along the beam line.

In order to meet space constraints, it is expected that the endcap assemblies can be moved laterally relative to the central part of the main detector. This should be achievable with a few cm of clearance, making it unnecessary to move them a substantial distance outward along the beam line. To accommodate this, it will be required that no part of the central detector is installed in the recess of either of the endcaps, and vice versa.

In this approach the support frame and the carriage system consist of five independent parts (one for the central piece and two more for each of the endcaps (see Figure 8.39), each on their own sets of the heavy duty Hilman rollers. Given the size of the endcap calorimeters, and the expected density of the absorber material, the total weight of each of the four of the endcap halves is estimated to be between 80-100 tons. The weight of the central part of the detector is estimated to be on the order of 500 tons, similar to the fully assembled sPHENIX detector without endcaps.

The beam pipe configuration (as shown in Figure 8.37), is expected to roughly follow the 1.5 m + 6.0 m + 1.5 m breakdown scheme, matching the main physics detector and consists of a $\sim$6.0 m long central part and two $\sim$1.5 m long endcaps. The central piece may be composed of more than one part. However, the installation procedure described here may be impacted if bulky, permanent flanges are used to interconnect the parts.

As shown in Figure 8.35, it is assumed that a clear $\sim$40 cm diameter "bore" is allocated for the forward / vertex / backward silicon detector assembly installation, and it is not obstructed by any other endcap equipment.

The pre-assembly sequence of the endcaps is straightforward, and does not require a detailed description at this stage.

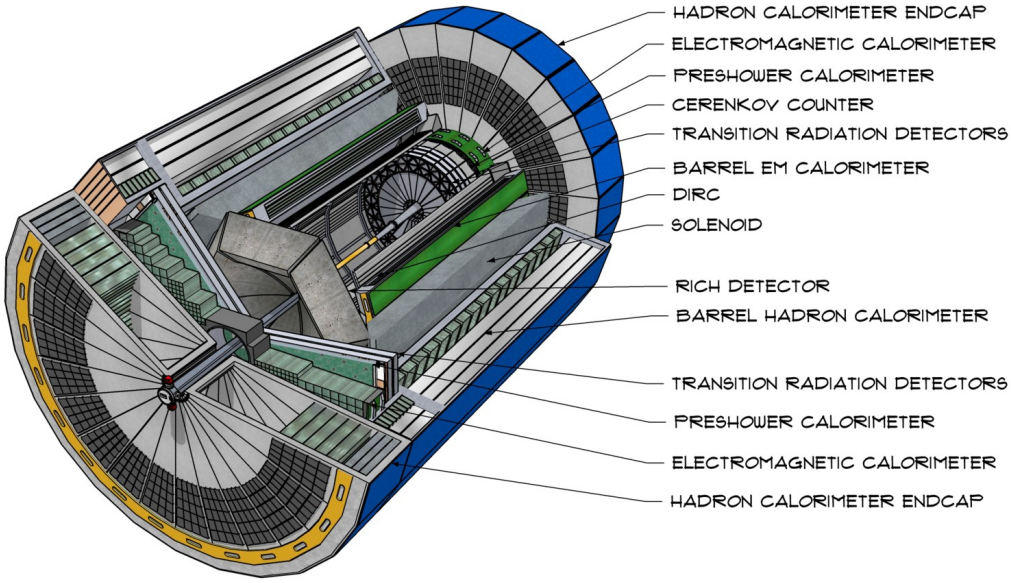

Figure 8.36: CAD model of the EIC detector, with the artistic rendering of the calorimetry subsystems.

Starting from the outer parts (the hadronic calorimeter, integrated into the solenoid flux return) the central part of the detector will be assembled on its own support structure. The inner barrel components (the solenoid cryostat, e/m calorimeter modules, PID detectors and the central volume tracker) will be added to the assembly one by one, in sequence, as is typically done for this type of detectors (e.g. BaBar and sPHENIX). Next the central piece of the beam pipe, as well as the two pre-assembled halves of the vertex silicon tracker are installed, with the latter ones connected to provide minimal clearance to the beam pipe. The endcap tracker and PID detector modules will be installed afterwards, starting from the inner modules.

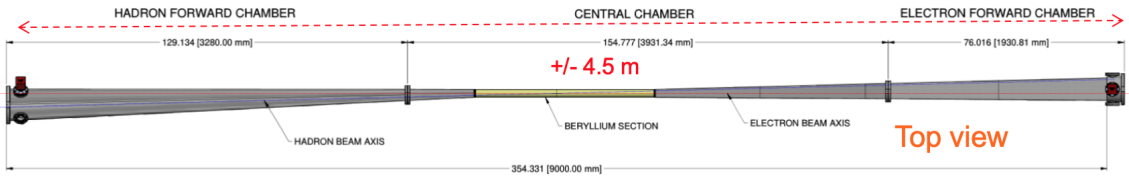

Figure 8.37: Interaction Region vacuum chamber layout.

The installation sequence of the B0 magnet equipment and the pre-assembled main detector blocks can look like this:

- The silicon tracker and the e/m calorimeter of the B0 magnet spectrometer are installed in its warm bore.
- The approximately 6 m long central part of the main detector, built around the solenoid magnet yoke, is rolled into the beam position, together with the electronics trailer and the pre-installed central piece of the beam pipe. Both endcaps are also rolled into the experimental hall, being split into halves, and moved away from the beam line, in order not to block access to the beam pipe installation.
- $\sim$1.5 m long pieces of the beam pipe are installed, together with the respective pump stands. This operation closes the accelerator UHV volume.
- The endcap halves are rolled towards the beam line and bolted together, as well as connected to the solenoid flux return yoke.

These actions are performed in the reverse sequence to move the detector from the experimental hall to the assembly area for maintenance.

Figure 8.38 shows the final installation of the EIC detector in the IP6 hall.

Detector Alignment

The internal alignment of the high-precision silicon tracker modules will be done on the bench, prior to installation in the experimental apparatus. It is assumed that the relative alignment of the detector components with respect to one other, to the solenoid magnet and to the beam line elements should be performed to accuracy on the order of $\sim$100 µm. This level of accuracy can be achieved using modern laser tracker survey apparatus, and by providing a redundant set of alignment marks on the detector frames, which are surveyed together with the network of the permanently mounted 3D points (survey mark nests) in the experimental hall. Maintaining visibility of the detector survey marks within the dense EIC installation environment will be a concern though, particularly for the inner tracker modules. Still, it should be noted that the ultimate alignment on the micron level of accuracy will be performed by software using the real particle tracks.

8.7.3 Access and Maintenance

Typically three different access and / or maintenance scenarios are expected. A short-term (controlled) access to the detector installation area where there will be no (dis)assembly of the equipment. This scenario would allow access to the electronics trailer, as well as the outer part of the sub-detector components, like FEE of the hadronic calorimeters.

A short shutdown (typically an emergency event, downtime of $<$ 48 hours) would allow the detector endcaps to be rolled out as indicated in Figure 8.39, providing an access to the endcap e/m calorimeters, outer part of the endcap trackers, beam pipe, as well as to a portion of the barrel part of the detector and the B0 silicon tracker for short maintenance.

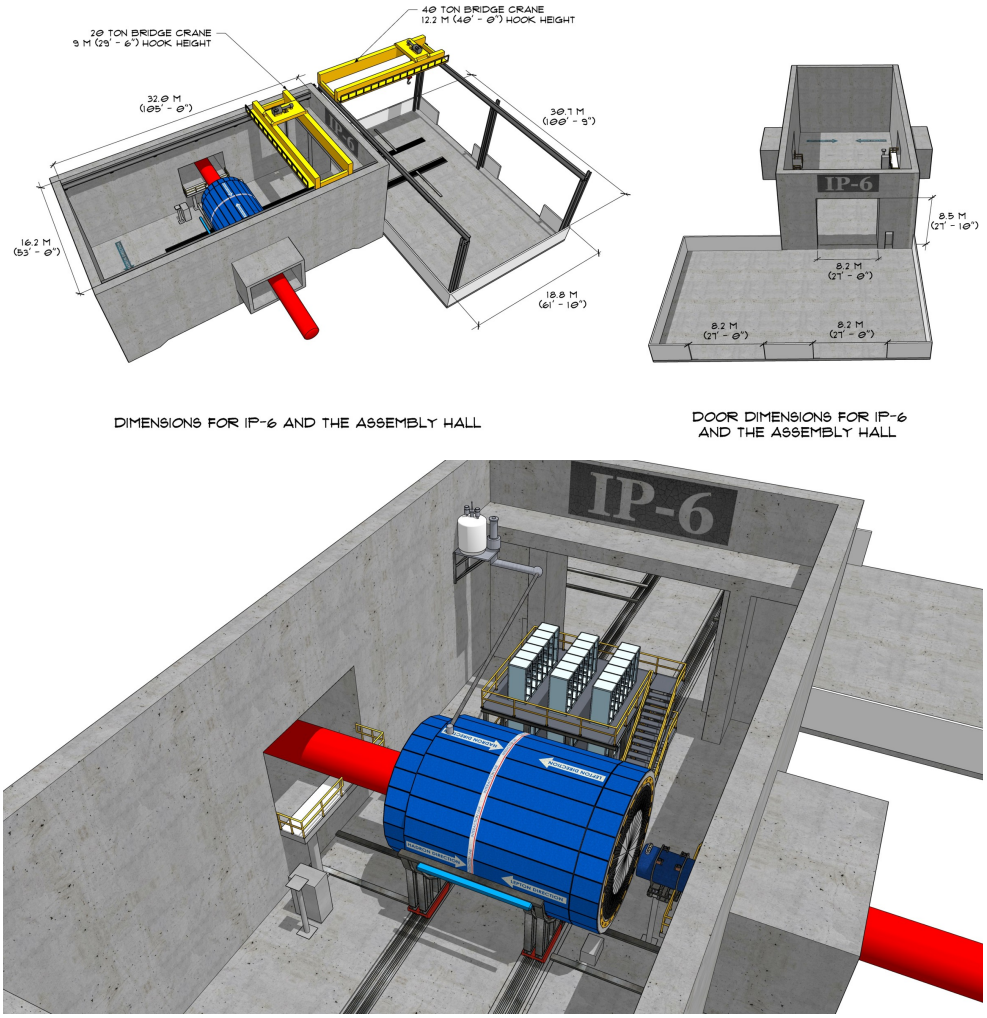

Figure 8.38: A model of the current detector system design in the experimental hall with magnets, cryocan, and rear carriage for the electronics.

This procedure will be easier in IP-6 (STAR Hall) than in IP-8 (PHENIX Hall) due to the tighter space constraints in IP-8, see Tab. 8.10, leaving less space to walk or move equipment (Fig 8.40).

During a long shutdown, the barrel part of the EIC detector could be moved out of the hall completely and sub-components could be disassembled safely. Fig. 8.41 shows how the barrel part of the detector together with the rear carriage could be rolled into the maintenance area outside of the hall. It is important to keep the readout electronics at the rear carriage next to the detector, to provide an easy way to test sub-components during the shutdown. Such a shutdown involves disassembly of the IP beam pipe section, as well as the beam pipes of RCS, dismantling of the shielding wall between the installation and assembly halls, and would require several weeks of downtime.

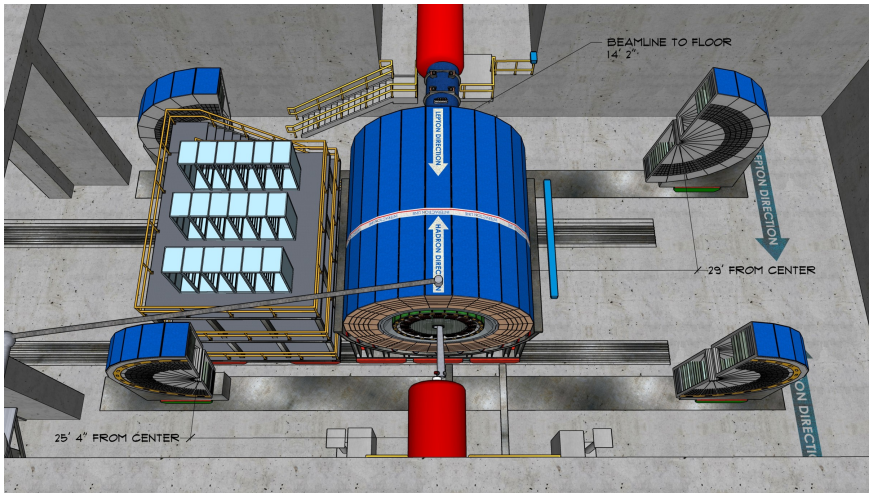

Figure 8.39: Barrel part of the main detector shown in the beam position. The endcaps shown rolled out to provide the space to access the inner parts of the barrel detectors.

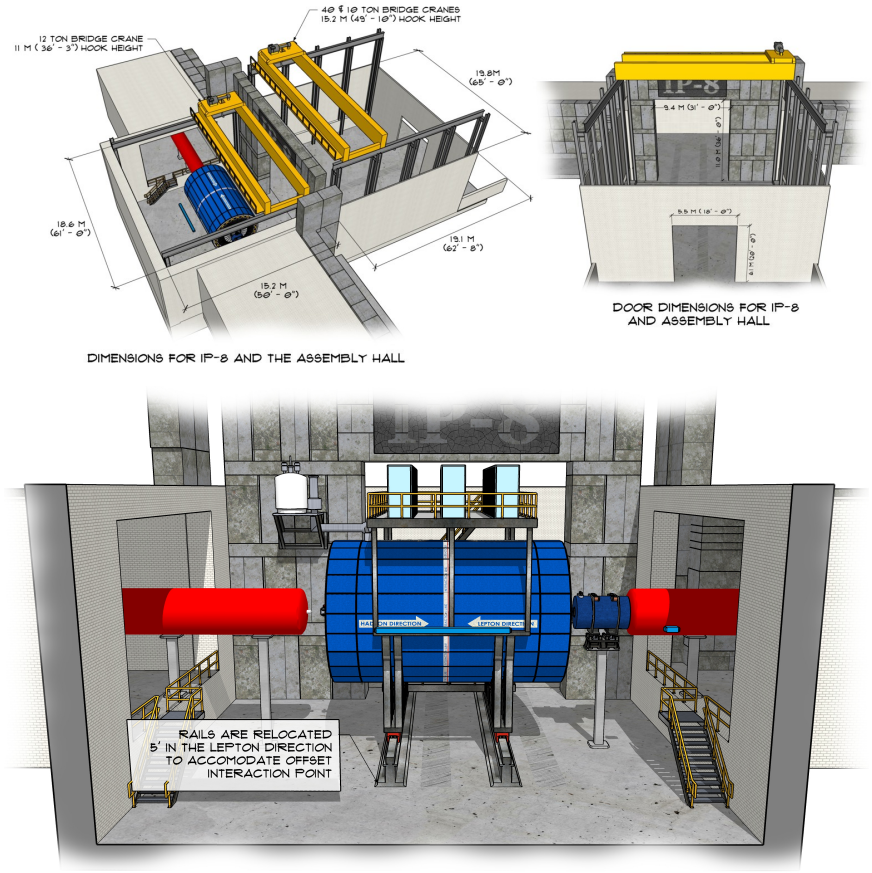

Figure 8.40: IP-8 (PHENIX Hall) installation

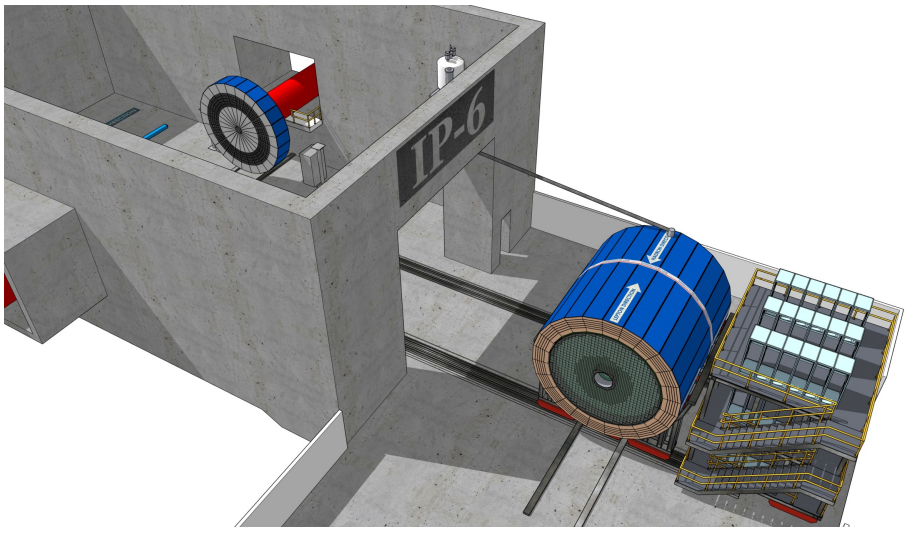

Figure 8.41: The barrel part of the detector and the rear carriage rolled into the maintenance area.

References

[1] National Academies of Sciences, Engineering, and Medicine, "An Assessment of U.S.-Based Electron-Ion Collider Science." The National Academies Press, Washington DC, 2018. https://doi.org/10.17226/25171.

[2] D. Boer *et al.*, "Gluons and the quark sea at high energies: Distributions, polarization, tomography," *arXiv preprint arXiv:1108.1713*, 2011.

[3] A. Accardi *et al.*, "Electron Ion Collider: The Next QCD Frontier," *Eur. Phys. J.*, vol. A52, no. 9, p. 268, 2016.

[4] A. Aprahamian *et al.*, "Reaching for the horizon: The 2015 long range plan for nuclear science." DOE/NSF Nuclear Science Advisory Panel (NSAC) Report, 2015.

[5] E. C. Aschenauer, S. Fazio, J. H. Lee, H. Mantysaari, B. S. Page, B. Schenke, T. Ullrich, R. Venugopalan, and P. Zurita, "The Electron-Ion Collider: Assessing the Energy Dependence of Key Measurements," *arXiv preprint arXiv:1708.01527*, 2017.

[6] "Generic Detector R&D for an Electron Ion Collider," 2011 - 2018. https://wiki.bnl.gov/conferences/index.php/EIC_R%25D.

[7] R. L. Jaffe and A. Manohar, "The G(1) Problem: Fact and Fantasy on the Spin of the Proton," *Nucl. Phys.*, vol. B337, pp. 509–546, 1990.

[8] E.-C. Aschenauer *et al.*, "The RHIC SPIN Program: Achievements and Future Opportunities," *arXive preprint arXive:1501.01220*, 2015.

[9] E. C. Aschenauer, R. Sassot, and M. Stratmann, "Unveiling the Proton Spin Decomposition at a Future Electron-Ion Collider," *Phys. Rev.*, vol. D92, no. 9, p. 094030, 2015.

[10] E. C. Aschenauer, I. Borsa, G. Lucero, A. S. Nunes, and R. Sassot, "Revisiting Helicity Parton Distributions at a Future Electron-Ion Collider," 7 2020.

[11] E. C. Aschenauer, R. Sassot, and M. Stratmann, "Helicity Parton Distributions at a Future Electron-Ion Collider: A Quantitative Appraisal," *Phys. Rev.*, vol. D86, p. 054020, 2012.

[12] D. Boer and P. J. Mulders, "Time reversal odd distribution functions in leptoproduction," *Phys. Rev.*, vol. D57, pp. 5780–5786, 1998.

[13] L. Zheng, E. C. Aschenauer, J. H. Lee, B.-W. Xiao, and Z.-B. Yin, "Accessing the Gluon Sivers Function at a future Electron-Ion Collider," *arXive preprint arXive:1805.05290*, 2018.

[14] D. W. Sivers, "Hard scattering scaling laws for single spin production asymmetries," *Phys. Rev.*, vol. D43, pp. 261–263, 1991.

[15] D. W. Sivers, "Single Spin Production Asymmetries from the Hard Scattering of Point-Like Constituents," *Phys. Rev.*, vol. D41, p. 83, 1990.

[16] J. Cammarota, L. Gamberg, Z.-B. Kang, J. A. Miller, D. Pitonyak, A. Prokudin, T. C. Rogers, and N. Sato, "Origin of single transverse-spin asymmetries in high-energy collisions," *Phys. Rev. D*, vol. 102, no. 5, p. 054002, 2020.

[17] D. Boer, C. Lorcé, C. Pisano, and J. Zhou, "The gluon Sivers distribution: status and future prospects," *Adv. High Energy Phys.*, vol. 2015, p. 371396, 2015.

[18] D. Müller, D. Robaschik, B. Geyer, F. M. Dittes, and J. Hořejši, "Wave functions, evolution equations and evolution kernels from light ray operators of QCD," *Fortsch. Phys.*, vol. 42, pp. 101–141, 1994.

[19] A. V. Radyushkin, "Scaling limit of deeply virtual Compton scattering," *Phys. Lett.*, vol. B380, pp. 417–425, 1996.

[20] X.-D. Ji, "Deeply virtual Compton scattering," *Phys. Rev.*, vol. D55, pp. 7114–7125, 1997.

[21] X.-D. Ji, "Gauge invariant decomposition of nucleon spin," *Phys. Rev. Lett.*, vol. 78, pp. 610–613, 1997.

[22] E.-C. Aschenauer, S. Fazio, K. Kumericki, and D. Mueller, "Deeply Virtual Compton Scattering at a Proposed High-Luminosity Electron-Ion Collider," *JHEP*, vol. 09, p. 093, 2013.

[23] P. Barry, N. Sato, W. Melnitchouk, and C.-R. Ji, "First Monte Carlo Global QCD Analysis of Pion Parton Distributions," *Phys. Rev. Lett.*, vol. 121, no. 15, p. 152001, 2018.

[24] J. Sullivan, "One pion exchange and deep inelastic electron - nucleon scattering," *Phys. Rev. D*, vol. 5, pp. 1732–1737, 1972.

[25] A. C. Aguilar *et al.*, "Pion and Kaon Structure at the Electron-Ion Collider," *Eur. Phys. J. A*, vol. 55, no. 10, p. 190, 2019.

[26] F. Gelis, E. Iancu, J. Jalilian-Marian, and R. Venugopalan, "The Color Glass Condensate," *Ann. Rev. Nucl. Part. Sci.*, vol. 60, pp. 463–489, 2010.

[27] L. Zheng, E. C. Aschenauer, J. H. Lee, and B.-W. Xiao, "Probing Gluon Saturation through Dihadron Correlations at an Electron-Ion Collider," *Phys. Rev.*, vol. D89, no. 7, p. 074037, 2014.

[28] K. J. Eskola, P. Paakkinen, H. Paukkunen, and C. A. Salgado, "EPPS16: Nuclear parton distributions with LHC data," *Eur. Phys. J.*, vol. C77, no. 3, p. 163, 2017.

[29] A. H. Mueller and J.-W. Qiu, "Gluon Recombination and Shadowing at Small Values of x," *Nucl. Phys.*, vol. B268, p. 427, 1986.

[30] E. C. Aschenauer, S. Fazio, M. A. C. Lamont, H. Paukkunen, and P. Zurita, "Nuclear Structure Functions at a Future Electron-Ion Collider," *Phys. Rev.*, vol. D96, no. 11, p. 114005, 2017.

[31] X. Chu, E.-C. Aschenauer, J.-H. Lee, and L. Zheng, "Photon structure studied at an Electron Ion Collider," *arXive preprint arXive:1705.08831*, 2017.

[32] B. Page, X. Chu, and E. Aschenauer, "Experimental Aspects of Jet Physics at a Future EIC," *Phys. Rev. D*, vol. 101, no. 7, p. 072003, 2020.

[33] M. Arratia, Y. Song, F. Ringer, and B. Jacak, "Jets as precision probes in electron-nucleus collisions at the Electron-Ion Collider," *Phys. Rev. C*, vol. 101, no. 6, p. 065204, 2020.

[34] X. Liu, F. Ringer, W. Vogelsang, and F. Yuan, "Lepton-jet Correlations in Deep Inelastic Scattering at the Electron-Ion Collider," *Phys. Rev. Lett.*, vol. 122, no. 19, p. 192003, 2019.

[35] I. Vitev, "Radiative processes and jet modification at the EIC," in *Probing Nucleons and Nuclei in High Energy Collisions: Dedicated to the Physics of the Electron Ion Collider*, pp. 244–247, 2020.

[36] J. Blumlein, "The Theory of Deeply Inelastic Scattering," *Prog. Part. Nucl. Phys.*, vol. 69, pp. 28–84, 2013.

[37] S. Chekanov *et al.*, "Leading proton production in deep inelastic scattering at HERA," *JHEP*, vol. 06, p. 074, 2009.

[38] S. Roesler, R. Engel, and J. Ranft, "The Monte Carlo event generator DPMJET-III," in *Advanced Monte Carlo for radiation physics, particle transport simulation and applications. Proceedings, Conference, MC2000, Lisbon, Portugal, October 23-26, 2000*, pp. 1033–1038, 2000.

[39] L. Zheng, E. C. Aschenauer, and J. H. Lee, "Determination of electron-nucleus collision geometry with forward neutrons," *Eur. Phys. J.*, vol. A50, no. 12, p. 189, 2014.

[40] G. R. Young *et al.*, "The 0-degree calorimeter for the relativistic heavy ion experiment WA80 at CERN," *Nucl. Instrum. Meth.*, vol. A279, pp. 503–517, 1989.

[41] Zero-degree High-Precision Hadronic Calorimetry, `https://wiki.bnl.gov/conferences/images/9/97/ZDC-2014-EIC-RD_2.pdf`.

[42] F. D. Aaron *et al.*, "Determination of the Integrated Luminosity at HERA using Elastic QED Compton Events," *Eur. Phys. J.*, vol. C72, p. 2163, 2012. [Erratum: Eur. Phys. J.C74,2733(2012)].

[43] H1 Luminosity Monitor, http://www-h1.desy.de/h1/www/h1det/lumi/.

[44] Zeus Luminosity Monitor, http://www-zeus.desy.de/zeus_det_papers/zeus_det_papers.html.

[45] http://www.desy.de/~pol2000/Welcome.html.

[46] https://wiki.bnl.gov/rhicspin/Polarimetry.

[47] Workshop on Opportunities for Polarized He-3 in RHIC and EIC, https://indico.bnl.gov/conferenceDisplay.py?ovw=True&confId=405.

[48] A. Adare *et al.*, "Concept for an Electron Ion Collider (EIC) detector built around the BaBar solenoid," 2 2014.

[49] "An EIC Detector Built Around The sPHENIX Solenoid - A Detector Design Study," 10 2018.

[50] R. Kersevan and M. Ady, "Recent developments of Monte-Carlo codes Molflow+ and Synrad+," in *10th International Particle Accelerator Conference*, p. TUPMP037, 2019.

[51] A. P. de Hass *et al.*, "The FoCal prototype—an extremely fine-grained electromagnetic calorimeter using CMOS pixel sensors," *Journal of Instrumentation*, 2018.

[52] U. Amaldi, ed., *Study of an ep Facility for Europe DESY, Hamburg, April 2-3, 1979.*, vol. 790402, (Hamburg, Germany), Deutsches Electron Synchrotron / European Committee for Future Accelerators, 1979.

[53] S. D. C. Soós *et al.*, "Versatile Link PLUS transceiver development," *Journal of Instrumentation*, 2017.

[54] CERN GBT Project: GBTX Manual, https://espace.cern.ch/GBT-Project/GBTX/Manuals/gbtxManual.pdf.

[55] K. Chen, H. Chen, J. Huang, F. Lanni, S. Tang, and W. Wu, "A Generic High Bandwidth Data Acquisition Card for Physics Experiments," *IEEE Trans. Instrum. Measur.*, vol. 69, no. 7, pp. 4569–4577, 2019.

[56] S. Campana and T. Wenaus, "An ATLAS distributed computing architecture for HL-LHC," *J. Phys. Conf. Ser.*, vol. 1085, no. 3, p. 032029, 2018.

[57] M. Frank, F. Gaede, C. Grefe, and P. Mato, "DD4hep: A Detector Description Toolkit for High Energy Physics Experiments," *J. Phys. Conf. Ser.*, vol. 513, p. 022010, 2014.

[58] R. Brun, A. Gheata, and M. Gheata, "The ROOT geometry package," *Nucl. Instrum. Meth. A*, vol. 502, pp. 676–680, 2003.

[59] S. Agostinelli *et al.*, "GEANT4: A Simulation toolkit," *Nucl. Instrum. Meth.*, vol. A506, pp. 250–303, 2003.

[60] G. Amadio *et al.*, "GeantV Alpha Release," *J. Phys. Conf. Ser.*, vol. 1085, no. 3, p. 032037, 2018.

[61] X. Ai, "Acts: A common tracking software," *arXiv: Instrumentation and Detectors*, 2019.

[62] J. Rauch and T. Schlüter, "GENFIT — a Generic Track-Fitting Toolkit," *J. Phys. Conf. Ser.*, vol. 608, no. 1, p. 012042, 2015.

[63] G. Barrand *et al.*, "GAUDI - A software architecture and framework for building HEP data processing applications," *Comput. Phys. Commun.*, vol. 140, pp. 45–55, 2001.

[64] M. Clemencic, H. Degaudenzi, P. Mato, S. Binet, W. Lavrijsen, C. Leggett, and I. Belyaev, "Recent developments in the LHCb software framework Gaudi," *J. Phys. Conf. Ser.*, vol. 219, p. 042006, 2010.

[65] D. Lawrence, A. Boehnlein, N. Brei, and D. Romanov, "JANA2: Multithreaded Event Reconstruction," *J. Phys. Conf. Ser.*, vol. 1525, no. 1, p. 012032, 2020.

[66] E. Tejedor, E. Bocchi, D. Castro, H. Gonzalez, M. Lamanna, P. Mato, J. Moscicki, and D. Piparo, "Facilitating collaborative analysis in SWAN," *EPJ Web Conf.*, vol. 214, p. 07022, 2019.

[67] S. Höche and S. Prestel, "The midpoint between dipole and parton showers," *Eur. Phys. J. C*, vol. 75, no. 9, p. 461, 2015.

[68] F. Dulat, S. Höche, and S. Prestel, "Leading-Color Fully Differential Two-Loop Soft Corrections to QCD Dipole Showers," *Phys. Rev. D*, vol. 98, no. 7, p. 074013, 2018.

[69] G. Schuler and H. Spiesberger, "DJANGO: The Interface for the event generators HERACLES and LEPTO," in *Workshop on Physics at HERA*, pp. 1419–1432, 1991.

[70] E. C. Aschenauer, T. Burton, T. Martini, H. Spiesberger, and M. Stratmann, "Prospects for Charged Current Deep-Inelastic Scattering off Polarized Nucleons at a Future Electron-Ion Collider," *Phys. Rev.*, vol. D88, p. 114025, 2013.

[71] P. Bedaque, A. Boehnlein, M. Cromaz, M. Diefenthaler, L. Elouadrhiri, T. Horn, M. Kuchera, D. Lawrence, D. Lee, S. Lidia, *et al.*, "Report from the AI For Nuclear Physics Workshop," *arXiv preprint arXiv:2006.05422*, 2020.

[72] P. Mehta, M. Bukov, C.-H. Wang, A. G. Day, C. Richardson, C. K. Fisher, and D. J. Schwab, "A high-bias, low-variance introduction to machine learning for physicists," *Physics reports*, vol. 810, pp. 1–124, 2019.

[73] C. Lynch, "Big data: How do your data grow?," *Nature*, vol. 455, no. 7209, p. 28, 2008.

[74] Alves Jr, A Augusto and Andrade Filho, LM and Barbosa, AF and Bediaga, I and Cernicchiaro, G and Guerrer, G and Lima Jr, HP and Machado, AA and Magnin, J and Marujo, F and others, "The LHCb detector at the LHC," *Journal of Instrumentation*, vol. 3, no. 08, p. S08005, 2008.

[75] "Streaming Readout Workshop," 2020. https://www.bnl.gov/srvii2020/.

[76] "Fast Machine Learning Workshop," 2020. https://indico.cern.ch/event/924283/.

[77] R. Chalapathy and S. Chawla, "Deep learning for anomaly detection: A survey," *arXiv preprint arXiv:1901.03407*, 2019.

[78] S. Farrell, P. Calafiura, M. Mudigonda, D. Anderson, J.-R. Vlimant, S. Zheng, J. Bendavid, M. Spiropulu, G. Cerati, L. Gray, *et al.*, "Novel deep learning methods for track reconstruction," *arXiv preprint arXiv:1810.06111*, 2018.

[79] D. Derkach, M. Hushchyn, T. Likhomanenko, A. Rogozhnikov, N. Kazeev, V. Chekalina, R. Neychev, S. Kirillov, F. Ratnikov, L. collaboration, *et al.*, "Machine-Learning-based global particle-identification algorithms at the LHCb experiment," in *Journal of Physics: Conference Series*, vol. 1085, p. 042038, IOP Publishing, 2018.

[80] C. Fanelli and J. Pomponi, "DeepRICH: learning deeply Cherenkov detectors," *Machine Learning: Science and Technology*, vol. 1, no. 1, p. 015010, 2020.

[81] H. Drucker and C. Cortes, "Boosting decision trees," in *Advances in neural information processing systems*, pp. 479–485, 1996.

[82] M. Dugger, B. Ritchie, I. Senderovich, E. Anassontzis, P. Ioannou, C. Kourkoumeli, G. Vasileiadis, G. Voulgaris, N. Jarvis, W. Levine, *et al.*, "A study of decays to strange final states with GlueX in Hall D using components of the BaBar DIRC," *arXiv preprint arXiv:1408.0215*, 2014.

[83] B. Page, X. Chu, and E. Aschenauer, "Experimental aspects of jet physics at a future EIC," *Physical Review D*, vol. 101, no. 7, p. 072003, 2020.

[84] G. Louppe, K. Cho, C. Becot, and K. Cranmer, "QCD-aware recursive neural networks for jet physics," *Journal of High Energy Physics*, vol. 2019, no. 1, p. 57, 2019.

[85] "Ml4jets workshop," 2020. https://iris-hep.org/projects/ml4jets.html.

[86] I. Goodfellow, J. Pouget-Abadie, M. Mirza, B. Xu, D. Warde-Farley, S. Ozair, A. Courville, and Y. Bengio, "Generative adversarial nets," in *Advances in neural information processing systems*, pp. 2672–2680, 2014.

[87] C. Doersch, "Tutorial on variational autoencoders," *arXiv preprint arXiv:1606.05908*, 2016.

[88] D. J. Rezende and S. Mohamed, "Variational inference with normalizing flows," *arXiv preprint arXiv:1505.05770*, 2015.

[89] M. Paganini, L. de Oliveira, and B. Nachman, "Accelerating science with generative adversarial networks: an application to 3D particle showers in multilayer calorimeters," *Physical review letters*, vol. 120, no. 4, p. 042003, 2018.

[90] R. Stevens, V. Taylor, J. Nichols, A. B. Maccabe, K. Yelick, and D. Brown, "AI for Science," tech. rep., Argonne National Lab.(ANL), Argonne, IL (United States), 2020.

[91] K. Li and J. Malik, "Learning to optimize," *arXiv preprint arXiv:1606.01885*, 2016.

[92] D. Whitley, "A genetic algorithm tutorial," *Statistics and computing*, vol. 4, no. 2, pp. 65–85, 1994.

[93] J. Snoek, H. Larochelle, and R. P. Adams, "Practical bayesian optimization of machine learning algorithms," in *Advances in neural information processing systems*, pp. 2951–2959, 2012.

[94] D. R. Jones, M. Schonlau, and W. J. Welch, "Efficient global optimization of expensive black-box functions," *Journal of Global optimization*, vol. 13, no. 4, pp. 455–492, 1998.

[95] E. Cisbani, A. Del Dotto, C. Fanelli, M. Williams, M. Alfred, F. Barbosa, L. Barion, V. Berdnikov, W. Brooks, T. Cao, *et al.*, "AI-optimized detector design for the future Electron-Ion Collider: the dual-radiator RICH case," *Journal of Instrumentation*, vol. 15, no. 05, p. P05009, 2020.

[96] "Town Hall on A.I. Projects in the Experimental Physics Program," 2020. https://wiki.jlab.org/epsciwiki/index.php/Aug˙28,_ENP_%2B_CST_AI/ML_Town_Hall.

[97] K. Deb, S. Agrawal, A. Pratap, and T. Meyarivan, "A fast elitist non-dominated sorting genetic algorithm for multi-objective optimization: NSGA-II," in *International conference on parallel problem solving from nature*, pp. 849–858, Springer, 2000.

[98] K. Deb, *Multi-objective optimization using evolutionary algorithms*, vol. 16. John Wiley & Sons, 2001.

[99] P. Feliot, J. Bect, and E. Vazquez, "A Bayesian approach to constrained single-and multi-objective optimization," *Journal of Global Optimization*, vol. 67, no. 1-2, pp. 97–133, 2017.

[100] Y. Jin and B. Sendhoff, "Pareto-based multiobjective machine learning: An overview and case studies," *IEEE Transactions on Systems, Man, and Cybernetics, Part C (Applications and Reviews)*, vol. 38, no. 3, pp. 397–415, 2008.

[101] "Joint Machine Learning Workshop, GlueX Panda EIC," 2020. https://indico.gsi.de/event/9244/.

[102] "AI4EIC-exp Workshop." Center for Frontiers in Nuclear Science, Stony Brook, 2021. https://indico.bnl.gov/category/218/.

[103] K. Aulenbacher, E. Chudakov, D. Gaskell, J. Grames, and K. D. Paschke, "Precision electron beam polarimetry for next generation nuclear physics experiments," *Int. J. Mod. Phys. E*, vol. 27, no. 07, p. 1830004, 2018.

[104] J. Hansknecht and M. Poelker, "Synchronous photoinjection using a frequency-doubled gain-switched fiber-coupled seed laser and ErYb-doped fiber amplifier," *Phys. Rev. ST Accel. Beams*, vol. 9, p. 063501, 2006.

[105] B. Sobloher, R. Fabbri, T. Behnke, J. Olsson, D. Pitzl, S. Schmitt, and J. Tomaszewska, "Polarisation at HERA - Reanalysis of the HERA II Polarimeter Data -," *HERA Internal Note*, 1 2012.

[106] A. Camsonne, J. Hoskins, *et al.*, "eRD15: R&D for a Compton Electron Detector," *EIC R&D Progress Report*, June 2017.

[107] A. Camsonne, J. Hoskins, *et al.*, "eRD15: R&D for a Compton Electron Detector," *EIC R&D Progress Report*, January 2016.

[108] F. Méot *et al.*, "eRHIC EIC: Plans for Rapid Acceleration of Polarized Electron Bunch at Cornell Synchrotron," in *9th International Particle Accelerator Conference*, p. MOPMF013, 2018.

[109] W. Fischer and A. Bazilevsky *Phys. Rev. ST Accel. Beams*, vol. 15, p. 041001, 2012.

[110] C. Aidala *et al. Phys. Rev. Lett.*, vol. 120, p. 022001, 2018.

[111] G. Mitsuka *Phys. Rev.*, vol. C95, p. 044908, 2017.